AIRBORNE WIRELESS COMMUNICATION MODELING AND ANALYSIS

THESIS

Matthew J. Vincie, Lieutenant, USAF

AFIT-ENG-14-M-80

DEPARTMENT OF THE AIR FORCE
AIR UNIVERSITY

AIR FORCE INSTITUTE OF TECHNOLOGY

Wright-Patterson Air Force Base, Ohio

AFIT-ENG-14-M-80

AIRBORNE WIRELESS COMMUNICATION MODELING AND ANALYSIS

THESIS

Presented to the Faculty

Department of Electrical and Computer Engineering

Graduate School of Engineering and Management

Air Force Institute of Technology

Air University

Air Education and Training Command

In Partial Fulfillment of the Requirements for the

Degree of Master of Science in Electrical Engineering

Matthew J. Vincie, BS

Lieutenant, USAF

March 2014

AFIT-ENG-14-M-80

AIRBORNE WIRELESS COMMUNICATION MODELING AND ANALYSIS

Matthew J. Vincie, BS

Lieutenant, USAF

Approved:

//signed//	13-03-14
Dr. Gilbert L. Peterson (Chairman)	Date
//signed//	13-03-14
Dr. John M. Colombi (Member)	Date
//signed//	13-03-14
Dr. David R. Jacques (Member)	Date

AFIT-ENG-14-M-80

Abstract

Over the past decade, there has been a dramatic increase in the use of unmanned aerial vehicles (UAV) for military, commercial, and private applications. Critical to maintaining control and a use for these systems is the development of wireless networking systems [1]. Computer simulation has increasingly become a key player in airborne networking developments though the accuracy and credibility of network simulations has become a topic of increasing scrutiny [2-5]. Much of the inaccuracies seen in simulation are due to inaccurate modeling of the physical layer of the communication system. This research develops a physical layer model that combines antenna modeling using computational electromagnetics and the two-ray propagation model to predict the received signal strength. The antenna is modeled with triangular patches and analyzed by extending the antenna modeling algorithm by Sergey Makarov, which employs Rao-Wilton-Glisson basis functions. The two-ray model consists of a line-of-sight ray and a reflected ray that is modeled as a lossless ground reflection. Comparison with a UAV data collection shows that the developed physical layer model improves over a simpler model that was only dependent on distance. The resulting two-ray model provides a more accurate networking model framework for future wireless network simulations.

I would like to thank my family and friends for their support in this endeavor. I would also like to extend a special thanks to my fiancée for her thoughtfulness and encouragement. Your love and support are very much appreciated.

Acknowledgments

I would like to express my sincere appreciation to my advisor, Dr. Gilbert Peterson, for his guidance and support throughout the course of my research. I would also like to thank Dr. David Jacques and Dr. John Colombi for their invaluable training in unmanned aerial systems and their involvement in flight-testing. I would like to thank Rick Patton and Captain Charles Neal for their technical guidance and assistance with flight tests. I would also like to thank the staff at Radical RC in Dayton, Ohio for their advice and demonstration of wiring procedures. I would like to extend appreciation to Co-Operative Engineering Services, Inc. (CESI) for facilitating the flight tests.

Matthew J. Vincie

Table of Contents

Page

List of Figures

Page

I Introduction

1.1. Motivation

It is of interest to the US military and several public institutions to develop a high fidelity simulation of airborne communication networks [5]. By making simulations perform closer to reality, communications protocols can be designed to handle the high variability of the wireless environment. In addition, a high fidelity simulation will provide a means to explore the optimization of flight paths and antennas to achieve the best network performance. Ultimately, there is a desire for a high fidelity simulation that can replace costly flight tests.

Several projects at AFIT have involved wireless communications among small unmanned aerial vehicles (SUAVs) [6-11]. These projects looked at extending the range of the wireless communication system [6,7], cooperative control [8,9], mesh networking [10], and network simulation [11]. In these projects, RF propagation was assumed to be isotropic in an environment free of obstacles. In reality, the wireless communication link is more complex and unreliable than these projects anticipated. A model for RF propagation will aid AFIT in both the development and deployment of future unmanned aerial systems (UASs).

Outside AFIT, ongoing airborne wireless communication research focuses mainly on the development of wireless systems rather than modelling the environment in which they operate. This research usually involves topics such as: autonomous node placement [12-14], flight path optimization [15,16], antenna diversity and tracking [17-21], protocol development [22], data ferrying [23,24], field experimentation [25-27], test bed development [28-30], range extension [31,32], unmanned aerial vehicle (UAV) development [33], and cooperative control [34]. These topics are subject to the wireless environment. As a result, they can all benefit from a simulator that characterizes the wireless environment.

1.2. Goals

This research has three goals. The first goal is to develop a method and algorithm for modeling wireless communication in a simplified, rural, outdoor environment. This model uses the position and attitude of each aircraft to predict the received signal strength (RSS). This model takes into account polarization and multipath interference due to ground reflection. The second goal is to devise a system to acquire flight telemetry and RSS measurements (Appendices A-D). The final goal is to validate the model by comparison with measured flight data.

1.3. Methodology

This research develops a physical layer model that combines antenna modeling using computational electromagnetics in the frequency-domain and the two-ray propagation model to predict the RSS. The antenna is modeled with triangular patches and analyzed by extending the antenna modeling algorithm by Sergey Makarov, which employs Rao-Wilton-Glisson basis functions. The two-ray model consists of a line-of-sight ray and a reflected ray that is modeled as a lossless ground reflection. This model is validated with real-world UAV data.

1.4. Contribution

This research provides future researchers with a foundation for airborne network simulation using MATLAB® and develops a model of the physical layer of an airborne communication system. MATLAB simulations are compared to real-world flight data to determine the accuracy of the model. This model is more accurate than models dependent only on distance and allows the user the flexibility to design new antenna models and test them in a simulated environment. A large portion of this research was spent in the development of a system for flight data acquisition using commercial-off-the-shelf products. For future researchers, this system is discussed in detail in the appendices.

1.5. Results

For validation, this model was compared to real-world UAV data from three scenarios. The first scenario compared the model to data collected in an Air-to-Air configuration where both aircraft were in flight; the second scenario compared the model to data collected in a Ground-to-Air configuration where the aircraft containing the access point was place on the ground and the aircraft containing the client was flown; and the third scenario compared the model to data collected in an Air-to-Ground configuration where the aircraft containing the client was placed on the ground and the aircraft containing the access point was flown. Data from all flight tests were combined and compared to the model, and the model developed in this research showed improvement in accuracy over a model that is only dependent on distance. Nonetheless, the model lacked higher precision due to inaccuracies in the antenna model and measurement errors contained in the flight data**.**

1.6. Layout

This chapter discussed the motivation for this research and the goals, methodology, contribution, and results. Chapter 2 presents the background material related to modeling the physical layer of an airborne RF wireless communication system. Chapter 3 presents the development of a model for simulating the airborne wireless environment. Chapter 4 compares the one-ray, two-ray, and Friis model results against data collected from several flight tests. Chapter 5 concludes the documentation of the research and presents recommendations for future research.

II Literature Review

2.1. Chapter Overview

This chapter presents the background material related to modeling the airborne RF wireless communication system. Section 2.2 discusses the growing demand from efficient and flexible communication systems within the DoD, and Section 2.3 discusses the Federal Communication Commission's investigation of airborne networking for disaster relief. Section 2.4 discusses previous AFIT work related closely to this research. Section 2.5 discusses the application and operation of network simulators. For this research, modeling of the physical layer is divided into two parts: propagation modeling and antenna modeling. Section 2.6 provides a brief description of propagation modeling using ray tracing. Section 2.7 discusses statistical propagation models and focuses on the two-ray model adopted in this research. Section 2.8 discusses the antenna modeling technique used in this research. Section 2.9 defines the scalar, vector, and matrix notations used in this thesis. Section 2.10 provides a summary of this chapter.

2.2 Reduction on DoD Electromagnetic Spectrum

On February 20, 2014, the DoD announced that they would be turning over part of the DoD allocated electromagnetic spectrum to the civilian sector [35]. This reduces the amount of spectrum available to the DoD to perform its mission which is becoming increasingly dependent on communications. Mission performance calls for the development of efficient and flexible communication systems. The operation of these systems will also require more stringent planning to avoid interference. Critical to the development of new communication systems and planning are realistic computer simulations which could reduce the overall cost of upgrades to DoD legacy communication systems.

2.3 Emergency Communications

The Federal Communications Commission is investigating the use of a deployable aerial communication architecture (DACA) to provide reliable communication to first responders after disasters [1]. A DACA provides a means to avoid road blockages which often impede ground repair crews and mobile ground based communications. In addition, DACA technology provides unique propagation advantages and increased coverage area. However, the problem of interference remains a large issue in the development of this system. The development and operation of a DACA is costly. This cost can be mitigated by implementing computer simulation in operational planning and system development.

2.4. Previous Research at AFIT using OPNET

In 2009, Major Clifton Durham evaluated the performance of the OPNET® network simulator in emulating a wireless airborne network [11]. In addition, he investigated the use of network simulators in the development of a mobile ad-hoc network (MANET). Durham compared recorded flight data to the simulated results in order to determine the accuracy of OPNET. Durham used three custom pairs of antenna radiation patterns in his analysis, and he found that the antenna model with the greatest level of detail yielded results closest to the real-world data in two of the three flight tests. The third flight test was said to be significantly different from the other tests and could not be successfully simulated. Durham found that an appropriate amount of detail must be put into the design of the network physical layer in order to produce results closer to reality. According to Durham, the model used to determine the path loss was the free-space model that has an inverse distance squared dependency. He suggested that solving the accuracy problem required complicated antenna engineering, which was beyond the scope of his research.

2.5. Network Simulators

Network simulation provides a means to test communication protocols and network configurations. A network simulator typically analyzes several layers of communication. These layers are defined in the Open System Interconnection (OSI) model [11]. Figure 1 shows the relationship between these layers.

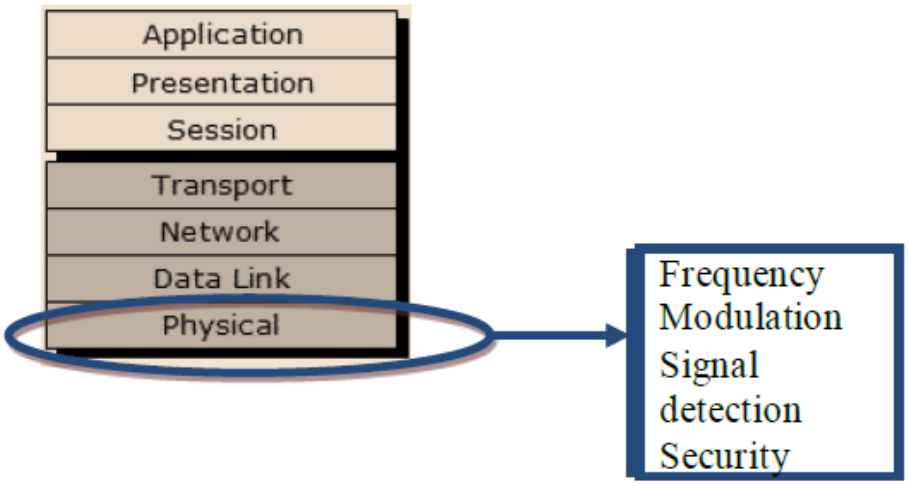

Figure 1: Seven Layer OSI Model [11].

The physical layer is the bottom layer of the model and defines how information is transmitted from one physical device to another. The physical layer can be wired, wireless, or even mechanical. The physical layer includes parameters such as voltages, currents, impedance, modulation, frequency, antenna gain, propagation, etc. Moving up from the physical layer, operations are performed on bits using both software and hardware.

This research focuses on the physical layer, which for a wireless environment is difficult to model. Inaccurate modeling of the physical layer can greatly reduce the accuracy of the network simulation. Major Durham gives an example of the physical layer model used by OPNET in his discussion of the transceiver pipeline [11, pp. 18]. This pipeline is depicted in

Figure 2. Stages 3, 4, and 7 are the focus of this research. These stages are critical in determining the signal-to-noise ratio (SNR) which is used to estimate the bit error rate (BER).

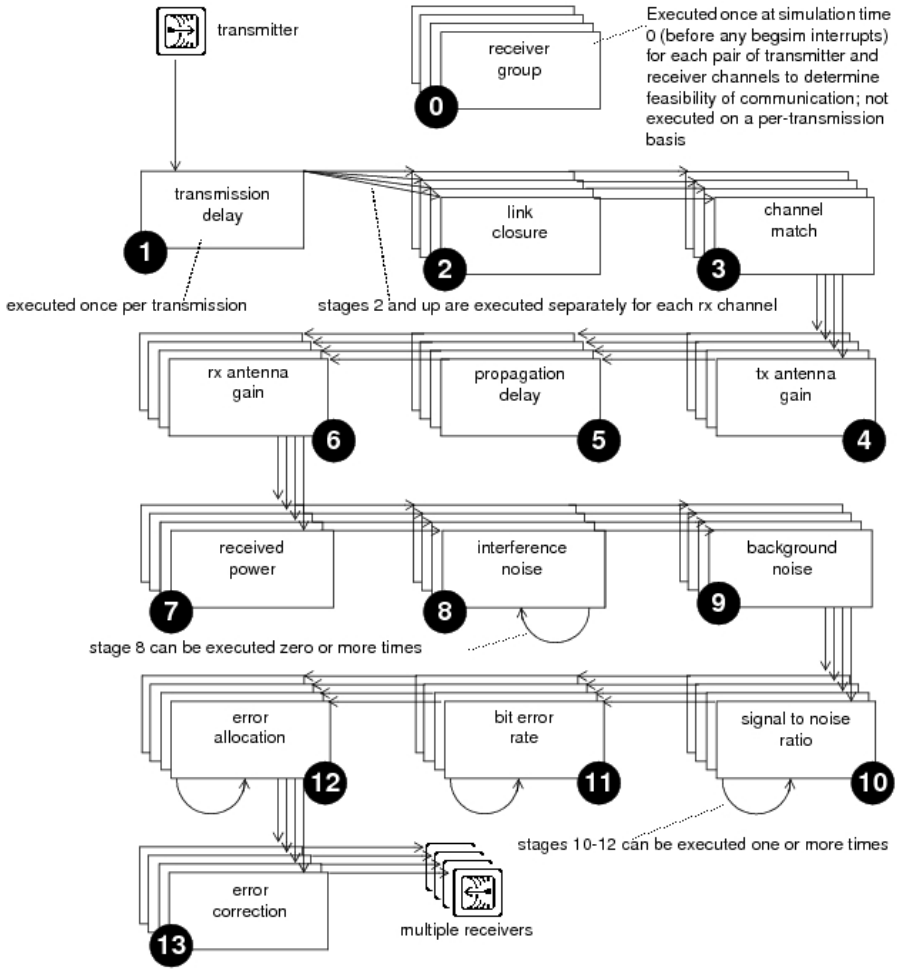

Figure 2: OPNET Radio Transceiver Pipeline [36].

2.6. Propagation Modeling: Ray Tracing

Ray tracing is a technique that is used to model RF propagation and provides the potential for the greatest accuracy in complex environments [37]. Ray tracing is done by repeatedly advancing narrow beams (rays) a discrete amount. As the ray advances, various materials cause the ray to bend, reflect, or be absorbed. Using a computer, a large number of rays can be propagated and summed to determine signal strength, polarization, and delay at a point of

interest. For example, SAIC® Urbana™ wireless toolkit uses 3-D ray tracing to simulate propagation and takes into account antenna radiation patterns, multipath, angle of arrival, delay, etc. [38]. The two drawbacks to this technique are the large computational expense and the requirement for an accurate 3-D representation of the region of interest. Furthermore, the electromagnetic characteristics of the materials in the region must be specified.

2.7. Propagation Modeling: Statistical Models

Statistical models of RF propagation are based on both experimental and theoretical data. They give a rough estimate of what the signal strength will be at a point of interest and are less computationally expensive than the ray trace method. They are employed in network simulators such as NS-2 and OPNET [11]; however, a majority of these models are not designed for airborne wireless networks [39-41]. According to a study performed by Nadeel Ahmed *et al*.,the two major contributors to link degradation in airborne networks are antenna orientation and multipath due to ground reflections [42].

A practical model found in [41] yielded RSS values that were close to reality when multipath due to ground reflection was present. To calculate the gain due to antenna orientation, they modelled antenna radiation patterns using real-world data. They then used the common two-ray model to determine RSS. This model is deterministic in nature. However, based on empirical data, they added a Gaussian error to the output of the model to compensate for imperfections in the hardware and the incomplete description of the wireless environment. This Gaussian error had a standard deviation that was dependent on the mean RSS. They found that as the mean RSS increased the standard deviation of the RSS decreased. By adding this error to their model, they were able to estimate the precision of their simulation. Though their model was accurate for a specific scenario, it does not accurately model airborne operations for two reasons. First, they

designed their model for strictly horizontal or vertical polarization, which for the airborne environment is seldom reality. Second, their antenna model cannot accurately define complex radiation patterns. To apply the two-ray model to airborne environment, the model must be reformulated to handle all polarizations, and the antenna must be modeled to accurately account for polarization and gain.

2.8. Antenna Modeling

Over the past 60 years, advancements in computational electromagnetics (CEM) have increased the fidelity of antenna models; and, in the last decade, advancements in computer technology have provided the computational power necessary to analyze these high fidelity models. It is beyond the scope of this thesis to discuss all the advancements in CEM. Instead, the model implemented in this research is discussed.

Like many engineering problems, antenna modeling can be framed in the frequency domain. Solving Maxwell's integral equations in the frequency-domain is the most popular and widely used method for antenna design and analysis [43]. Two frequently used methods to solve these equations in the frequency-domain are the finite element (FE) method and the Method of Moments (MoM). The MoM is more efficient than the FE method when the antenna is comprised solely of conducting material. Since the antenna used in the research was comprised of only conducting material, the MoM was selected for this research. This method has improved in capability and fidelity since the 1960s. Two common antenna problems simulated using the MoM are wire and surface antennas. The latter is used in this research because it provides future researchers the capability of analyzing more complex antenna structures.

In the simulation of a surface antenna, a surface integral equation is solved. Solving the surface integral equation requires breaking the surface into smaller surface patches. Modeling the

antenna with surface patches was one of the more challenging aspects of modeling antennas because expansion functions of the time did correctly model current continuity from patch-to-patch [43]. In 1982, Rao, Wilton, and Glisson (RWG) developed the vector basis functions which substantially improved the fidelity of the surface antenna simulation. Sergey N. Makarov, whose code was adopted in this research, employed these vector basis functions and the MoM [44]. For brevity and because many other resource are available for this type of antenna modeling, further details of this model are not discussed in this thesis. Makarov's codes can be downloaded from [45].

2.9. Scalar, Vector, and Matrix Notations

Throughout the methodology and results section of this thesis, the following notations are adhered to. Scalars are italicized. Vectors appear with an arrow on top (for example—$\vec{z}_A$) and are in column form. Matrices are bold and italicized.

2.10. Summary

This chapter discussed the background materials related to modeling an airborne RF wireless communication system. Sections 2.2 and 2.3 discussed the growing demand for better airborne communication systems. Section 2.4 discussed Major Durham's work at AFIT using OPNET to simulate an airborne wireless network, where he found that greater model fidelity was needed to accurately model the physical layer. Section 2.5 briefly discussed network simulators and the physical layer of the communication system. Sections 2.6 and 2.7 looked at how wireless propagation could be modeled using ray tracing or statistical models. Ray tracing has the potential for greater fidelity but is more computationally expensive and complex than statistical model. Section 2.8 provided a background of the antenna modeling technique used in this research. Section 2.9 defined the notation for scalars, vectors, and matrices in this thesis.

III Methodology

3.1. Chapter Overview

This chapter presents the development of a model for simulating the airborne wireless environment. The model incorporates multipath due to ground reflects into the calculation of the received signal strength (RSS). The more accurate this calculation is, the more realistic results from flight path optimization and communication protocol development will be.

The method used in this research to characterize the wireless environment is the two-ray model. This model takes into account the multipath due to ground reflection. Figure 3 shows the two rays leaving the transmitting antenna and ending at the receiving antenna. In this model, the effects of the airframe on the electromagnetic (EM) field are ignored.

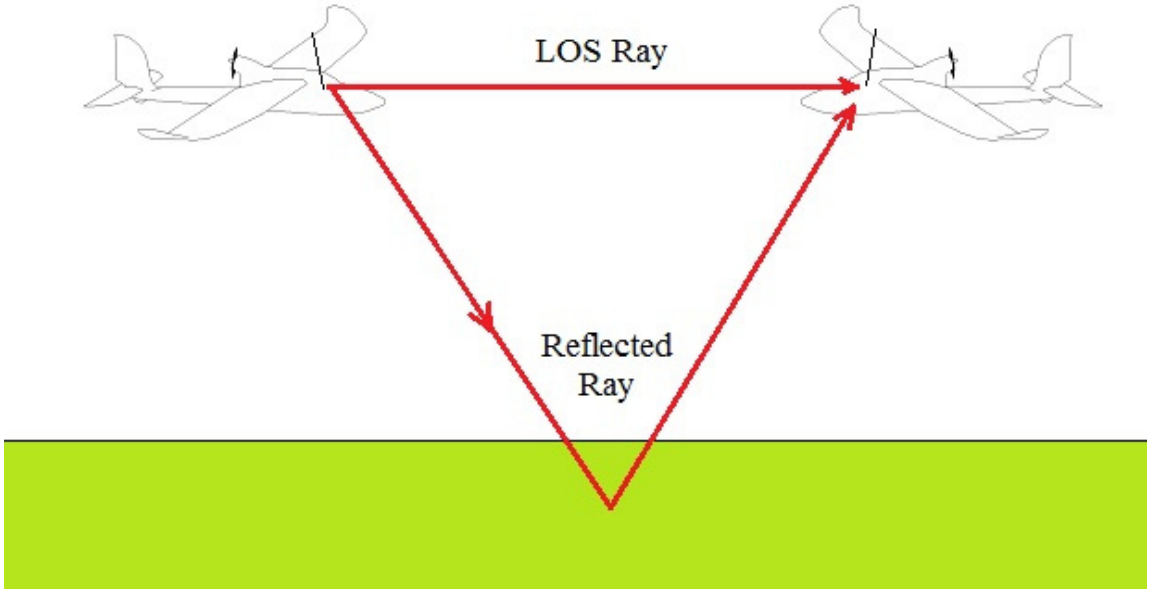

Figure 3: Airborne Two-Ray Model.

The MATLAB® algorithm designed to implement the two-ray model splits the data flow into two threads (Figure 4 and Figure 5). These two threads show the steps necessary to calculate the EM field of the reflected and line-of-sight (LOS) rays. Each process block includes a

reference to the section that discusses the computation within that block. The outputs of these two threads are combined for the calculation of the RSS at the receiving antenna.

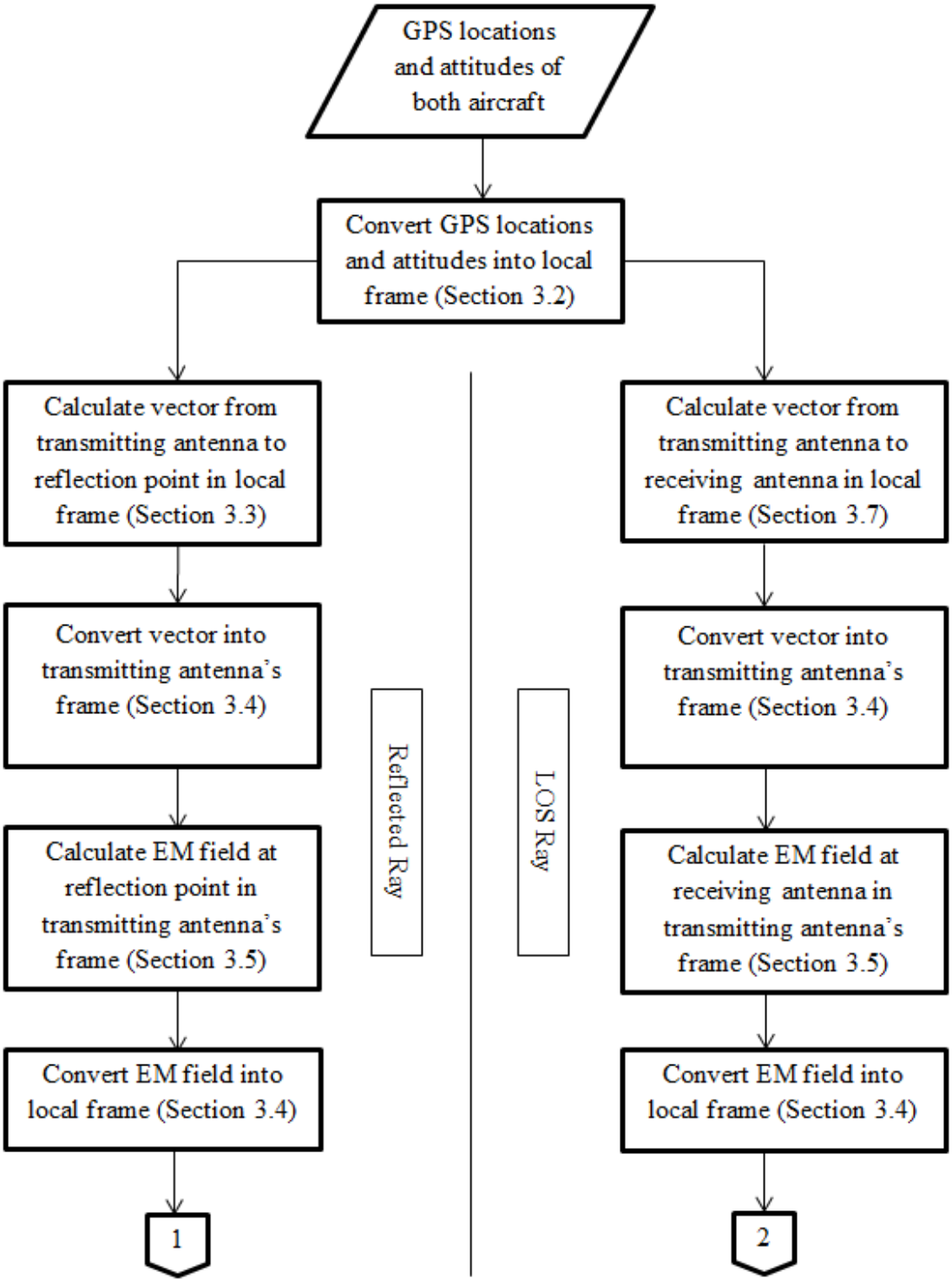

Figure 4: Two-Ray Algorithm Flow Chart (Part 1 of 2).

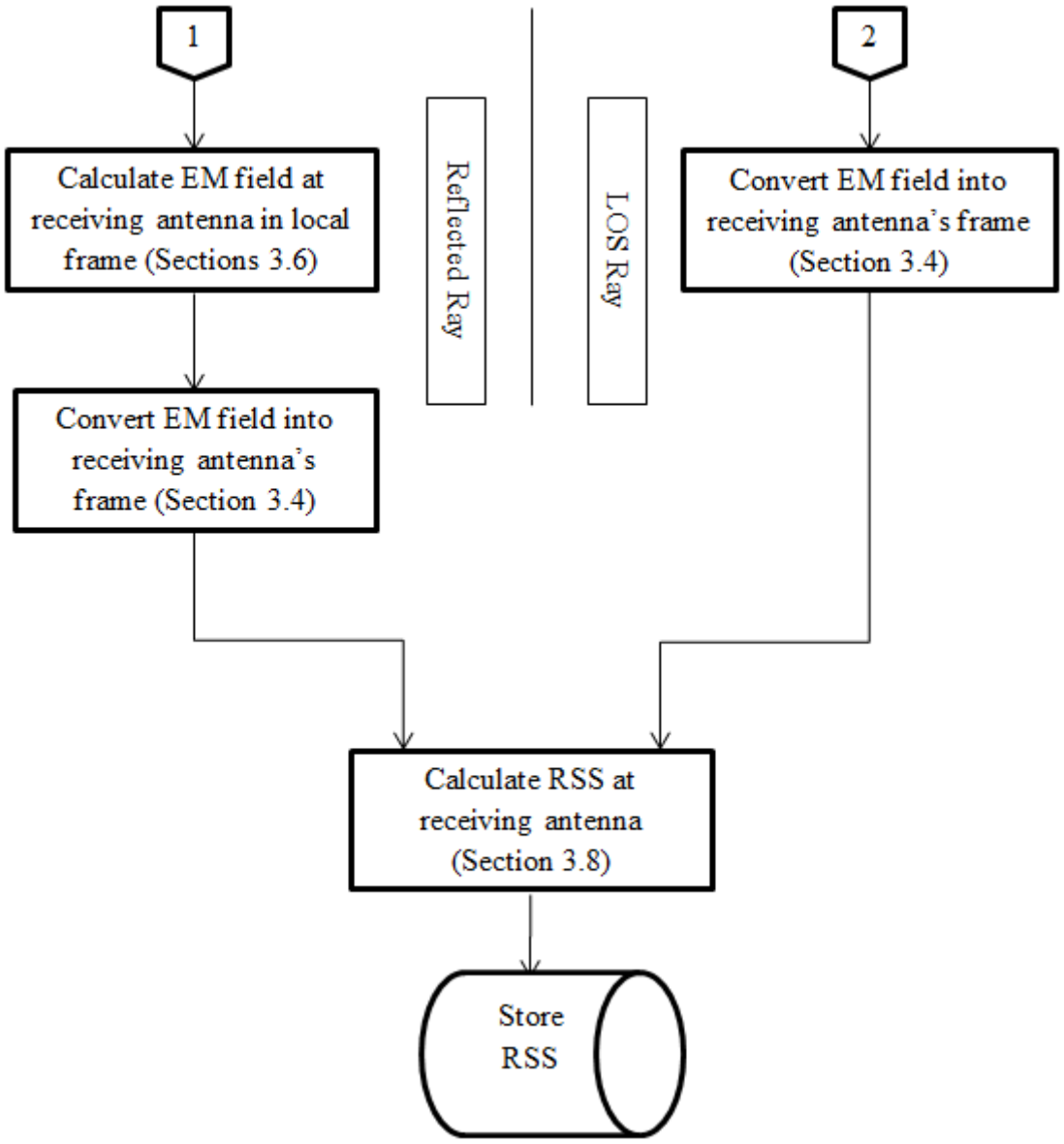

Figure 5: Two-Ray Algorithm Flow Chart (Part 2 of 2).

The two threads do not run simultaneously during the computation of one RSS calculation. The reflected ray's thread runs first followed by the LOS ray's thread. However, parallel computing is implemented which allows four RSS calculations to run simultaneously on a four core processor.

Section 3.2 discusses the method used to convert GPS longitude and latitude in the local coordinated frame. Section 3.3 derives the equations for determining the location of the

reflection point. Section 3.4 presents the transformation between local and antenna frames. Section 3.5 discusses the method used to develop the antenna model and compares the simulated radiation characteristics to the datasheet of the research antenna. Section 3.6 derives the equations used to determine the strength and polarization of the reflected ray. Section 3.7 briefly describes the method used to calculate the LOS ray at the receiving antenna. Section 3.8 discusses the method used to combine the two rays at the receiving antenna and the method used to estimate the RSS. Section 3.9 describes the testing of the model in six validation scenarios. Section 3.10 discusses the method used for performance evaluation of the model, and Section 3.11 summarizes the model developed in this chapter.

3.2. Conversion of Aircraft GPS Location into the Local Cartesian Frame

In the local frame, the ground is considered to be an infinite, flat plane with the origin centered at longitude = -86.009389° and latitude = 39.34300°. This places the origin at the center of the small UAV airstrip at Camp Atterbury, Johnson, Indiana (Figure 6). The flat plane model is accurate for a small change in latitude and longitude. For this reason, the origin was placed at the center of the runway. For the selected origin, a one-degree change in longitude results in an 86,206.576 m change in the $+x_L$-axis direction, and a one-degree change in the latitude results in an 111,022.01 m change in the $+y_L$-axis direction [46]. The altitude stored by the autopilot is equal to the displacement in the $+z_L$-axis direction.

Figure 6: Map of Small UAV Airstrip Superimposed with Local Frame.

3.3. Reflection Point Localization

Before the characteristics of the reflected wave can be determined, it is necessary to calculate the location of the ground reflection point. Figure 7 portrays the geometry of the reflected ray's path. In the local frame, the coordinate with subscripts L1 defines the location of the transmitter, the coordinate with subscripts L2 define the location of the ground reflection point, and the coordinate with subscripts L3 define the location of the receiver.

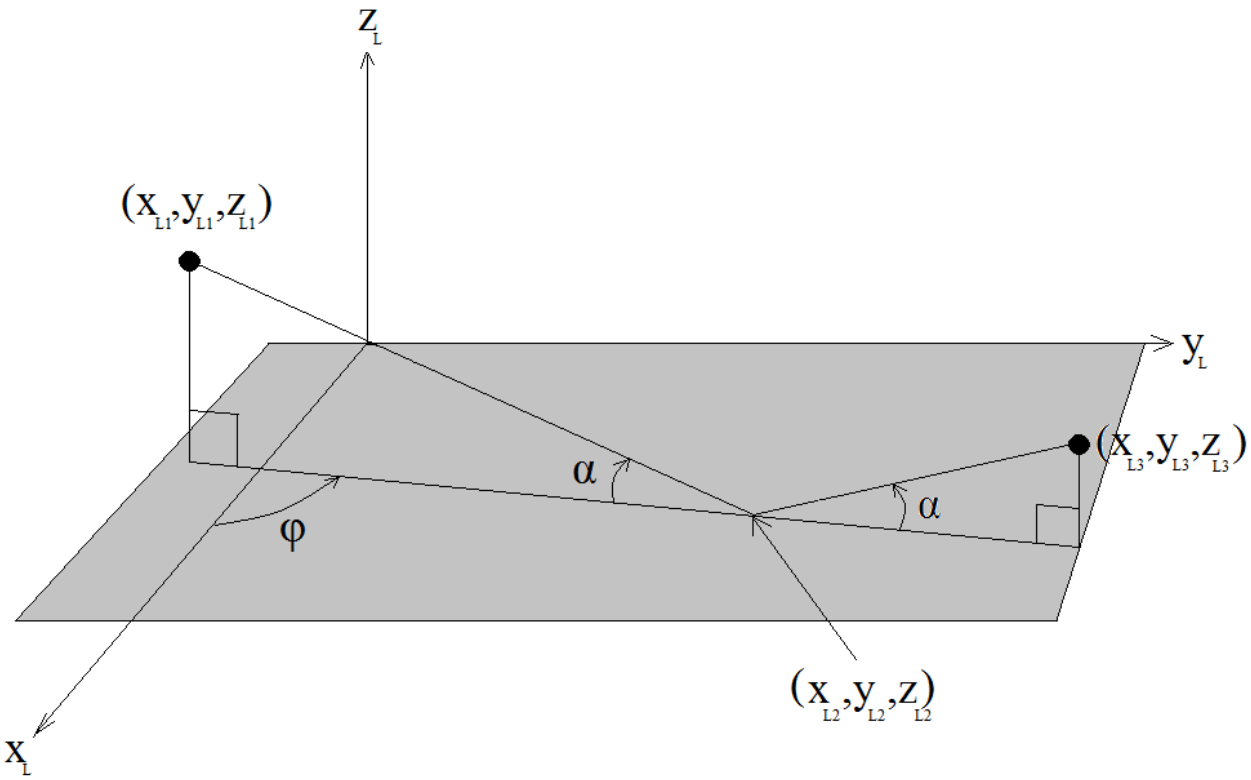

Figure 7: Reflection Geometry in Local Frame.

According to the law of reflection, the angle of incidence is equal to the angle of reflection. This relationship is seen in Figure 7 with the angle α. The angle φ is calculated using Equation 1:

$$\cos\varphi = \frac{x_{L3} - x_{L1}}{\sqrt{(x_{L3} - x_{L1})^2 + (y_{L3} - y_{L1})^2}} \tag{1}$$

The geometry is then viewed in two dimensions as shown in Figure 8, where d_3 is the ground distance between the transmitter and the receiver and is calculated using Equation 2:

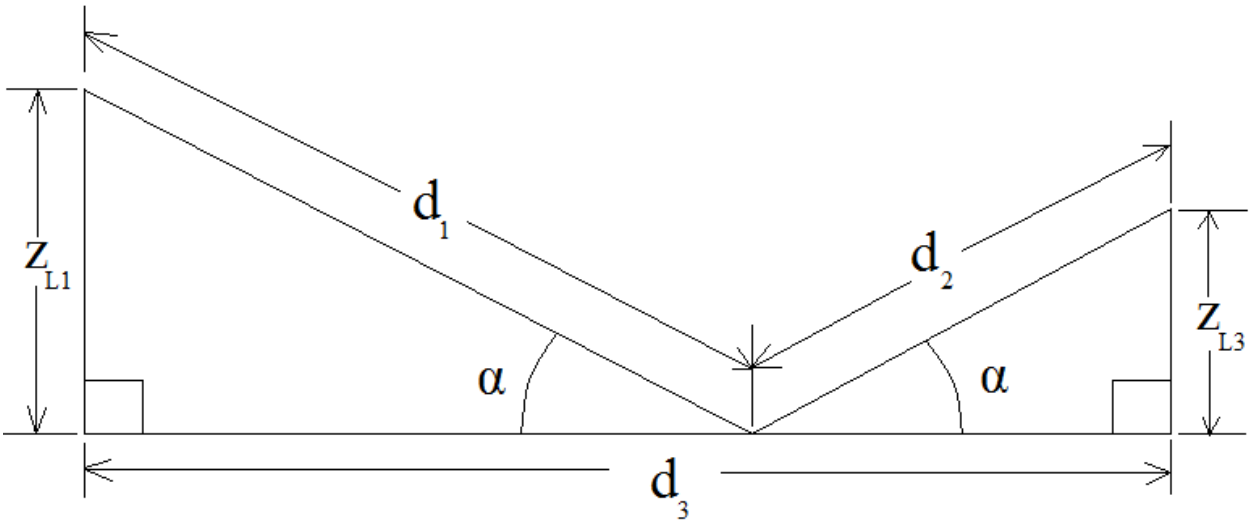

Figure 8: Plane of Incidence Geometry.

$$d_3 = \sqrt{(x_3 - x_1)^2 + (y_3 - y_1)^2} \tag{2}$$

For the geometry of Figure 8,

$$d_1 = \frac{z_{L1}}{\sin\alpha} \tag{3}$$

$$d_2 = \frac{z_{L3}}{\sin\alpha} \tag{4}$$

$$\alpha = \tan^{-1}\left(\frac{z_{L1} + z_{L3}}{\sqrt{(x_{L3} - x_{L1})^2 + (y_{L3} - y_{L1})^2}}\right) \tag{5}$$

The location of ground incidence is then

$$(x_{L2}, y_{L2}, z_{L2}) = (x_{L1} + d_1 \cos\alpha \cos\varphi, y_{L1} + d_1 \cos\alpha \sin\varphi, 0) \tag{6}$$

One can calculate the vector from the transmitting antenna to the receiving antenna using

$$\vec{v}_{L1\to L2} = \begin{bmatrix} x_{L2} \\ y_{L2} \\ z_{L2} \end{bmatrix} - \begin{bmatrix} x_{L1} \\ y_{L1} \\ z_{L1} \end{bmatrix} \tag{7}$$

3.4. Transformations between Orthogonal Coordinate Frames

For this research, calculations for the EM field radiated by or incident on an antenna are done in the antenna's frame. However, while the EM wave is in transit between antennas,

calculations are done in the local frame or reflection frame. Therefore, a transformation between orthogonal coordinate frames is necessary.

To transform the coordinates of a vector in the local frame into the antenna's frame, four direction cosine matrices (DCMs) which correspond to rotations in yaw, pitch, roll, and antenna angle are developed. The rotations will align the $\vec{z}_A$-axis with the antenna and the $\vec{y}_A$-axis with the left wing of the aircraft (Figure 9). Because the autopilot and GPS unit are located close to the antenna, the origin of the reference frame used by the autopilot is assumed to be located at the origin of the antenna's frame.

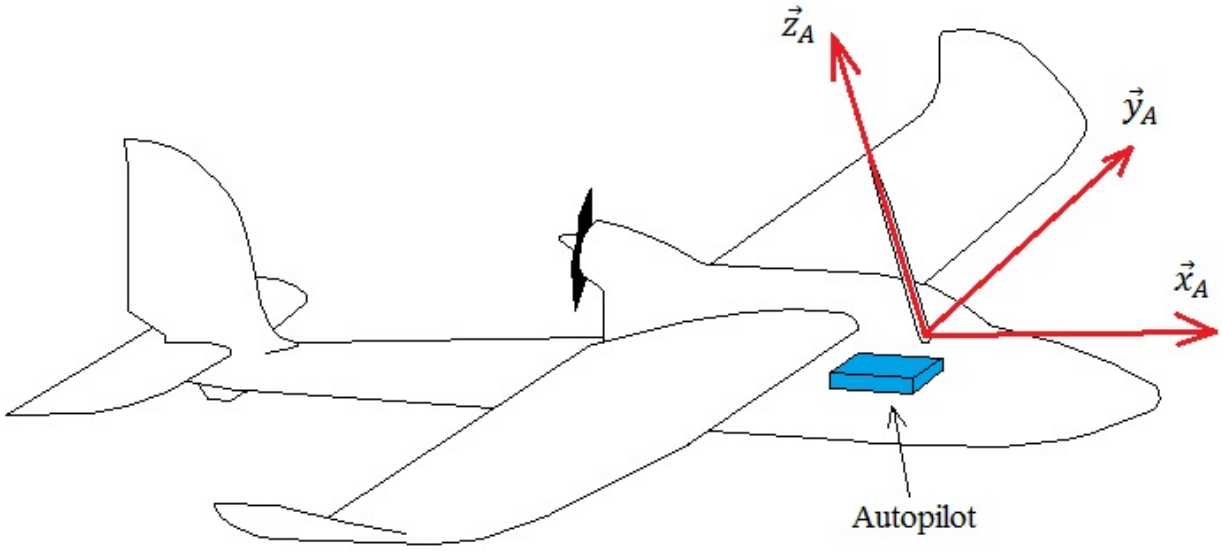

Figure 9: Antenna's Coordinate Frame.

The first DCM, Equation 8, corresponds to a rotation about the about the yaw axis:

$$\boldsymbol{R_z} = \begin{bmatrix} \cos(\gamma) & \sin(\gamma) & 0 \\ -\sin(\gamma) & \cos(\gamma) & 0 \\ 0 & 0 & 1 \end{bmatrix} \tag{8}$$

Where γ is the yaw angle. A rotation is then performed about the pitch axis:

$$\boldsymbol{R_{y1}} = \begin{bmatrix} \cos(-\beta) & 0 & -\sin(-\beta) \\ 0 & 1 & 0 \\ \sin(-\beta) & 0 & \cos(-\beta) \end{bmatrix} \tag{9}$$

Where β is the pitch angle. The third rotation is performed about the roll axis:

$$\boldsymbol{R_x} = \begin{bmatrix} 1 & 0 & 0) \\ 0 & \cos(\delta) & \sin(\delta) \\ 0 & -\sin(\delta) & \cos(\delta) \end{bmatrix} \tag{10}$$

Where δ is the roll angle. The final rotation is due to the position of the antenna with respect to the aircraft (Appendix A). This rotation is about the y-axis by -5°:

$$\boldsymbol{R_{y2}} = \begin{bmatrix} \cos(-5°) & 0 & -\sin(-5°) \\ 0 & 1 & 0 \\ \sin(-5°) & 0 & \cos(-5°) \end{bmatrix} \tag{11}$$

A vector is transformed from the local frame to the antenna frame by Equation 12:

$$\vec{V}_A = \boldsymbol{R_{y2}R_xR_{y1}R_z}\vec{V}_L \tag{12}$$

Note that the matrix multiplication is not commutative and that the matrix multiplication must be performed in the order prescribed by Equation 12.

To transform a vector from the antenna's frame to the local frame, matrix algebra is used to solve for $\vec{V}_L$ in Equation 12. This yields

$$\vec{V}_L = \left(\boldsymbol{R_{y2}R_xR_{y1}R_z}\right)^{-1}\vec{V}_A \tag{13}$$

Since each of the frames is orthogonal, Equation 13 can be written as

$$\vec{V}_L = \left(\boldsymbol{R_{y2}R_xR_{y1}R_z}\right)^{T}\vec{V}_A \tag{14}$$

Where $\left(\boldsymbol{R_{y2}R_xR_{y1}R_z}\right)^{T}$ is the transpose of $\boldsymbol{R_{y2}R_xR_{y1}R_z}$.

3.5. Transmitting Antenna Model

In order to model the transmitting antenna, MATLAB codes written by Sergey N. Makarov [44] were adopted. This code requires a 3-D model of the antenna created using triangular patches. The antenna used for flight data collection was cut open to reveal the internal geometry of the antenna (Figure 10).

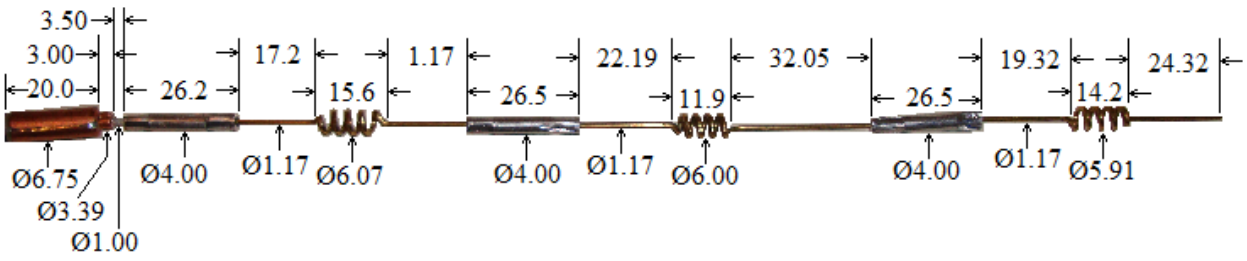

Figure 10: Internal Geometry of Research Antenna.

Using the dimensions of the antenna, code was written that divided the antenna up into 15 sections, and these sections were populated with triangular patches (Figure 11). Each coil has 4 turns; and the feeding-edge, which is the location where the shielded cable connects to the antenna, is located between the sections that have a 3.39-mm diameter and a 1.00-mm diameter. Correspondingly, the feeding-edge is located at coordinate (0, 0, 0) in the MATLAB model. Each section is modelled by a 2-D strip with a width equal to four times the radius of the wire for that section [44, pp. 60].

Makarov's code uses the 3-D model to calculate an impedance matrix. This matrix is used in the determination of the electric current flowing on the antenna surface [44, pp. 3]. Once the electric current flow is determined, the radiated field can be determined at any point in space. Figure 12 shows a quantitative representation of the power passing through each triangular subsection of a sphere with a radius of 100 m. The axes shown in Figure 12 correspond to the axes of the antenna's frame. The dark blue triangles represent the regions of lowest transmitted power, and the dark red triangles represent the regions of highest transmitted power. A majority of this antenna's power is confined to low elevation angles, while the power remains approximately constant for every azimuthal angle. This pattern is common for omni-directional antennas, and the antenna used in this research is omni-directional [47].

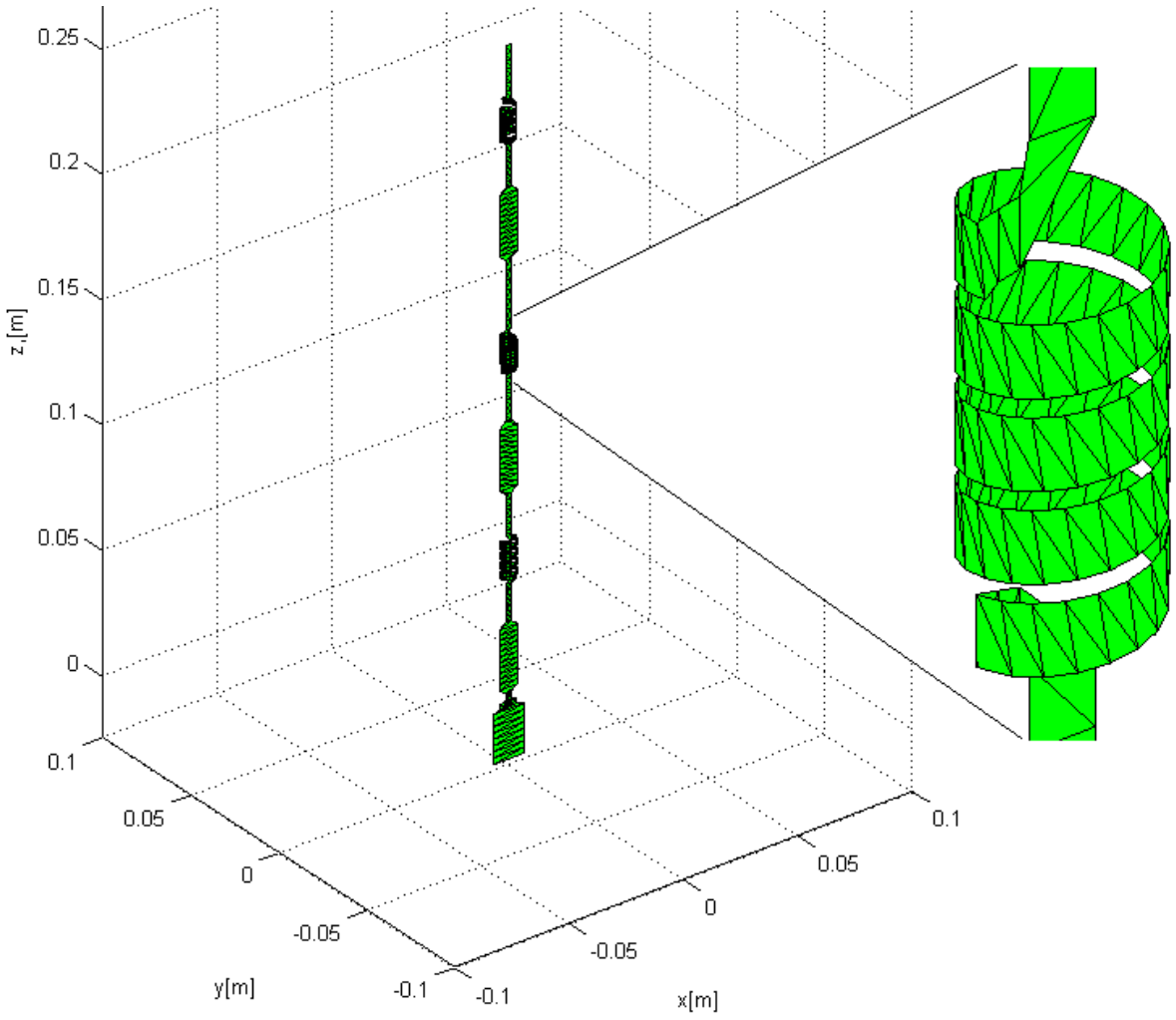

Figure 11: 3-D Antenna Model made from 2-D Patches.

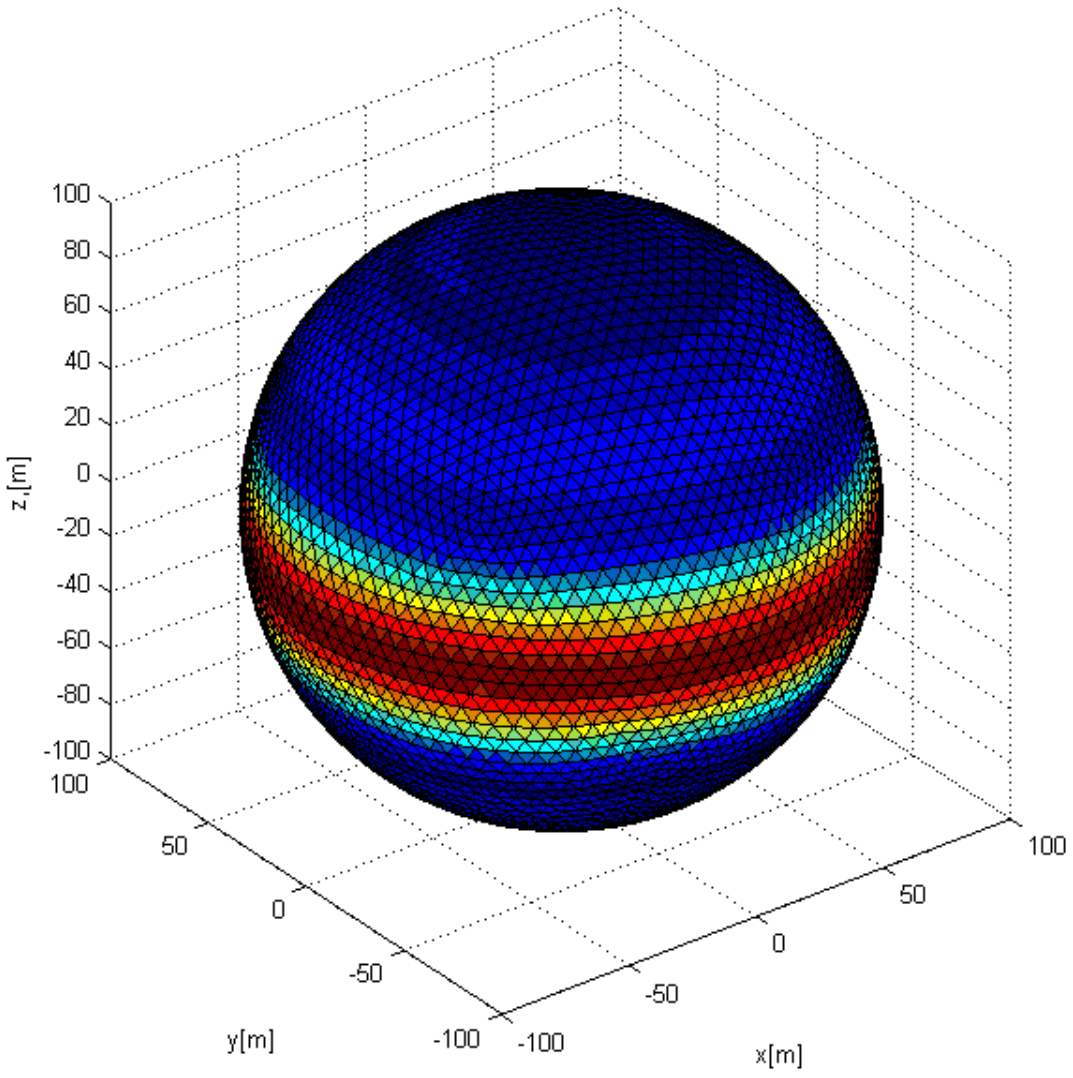

Figure 12: Qualitative Representation of Power Distribution.

In order to validate the accuracy of this model, the radiation patterns must be compared to the antenna's datasheet. Figure 13 shows the datasheet's vertical plane co-polarization pattern in orange. The vertical plane co-polarization E-field pattern generated by the simulation is superimposed in blue.

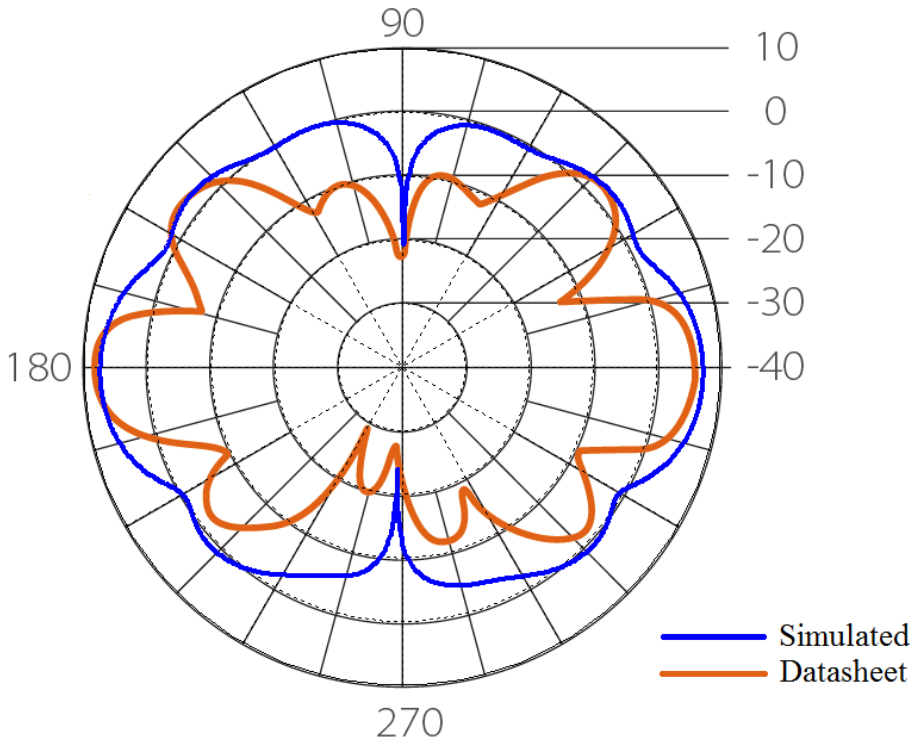

Figure 13: Vertical Plane Co-polarization E-field Pattern (Radial Unit is dB).

Figure 12 shows the comparison of the datasheet's vertical plane co-polarization pattern to the pattern representing the simulated transmitted power at a given elevation. This figure looks more like the pattern seen in the datasheet than Figure 13. The datasheet's vertical plane co-polarization pattern is asymmetric. This asymmetry may be a result of the test configuration or, if simulation was employed, the model used to simulate the antenna's radiation. The simulated pattern in blue has negligible asymmetry. Figure 15 shows the horizontal plane H-field co-polarization pattern. This pattern is the same as the horizontal plane co-polarization pattern in the datasheet.

The simulated antenna model produced similar propagation patterns to those found in the datasheet; consequently, this model was used in all simulations. Furthermore, the 3-D patch model was used to compute both the radiated field of the transmitting antenna and the current in the receiving antenna.

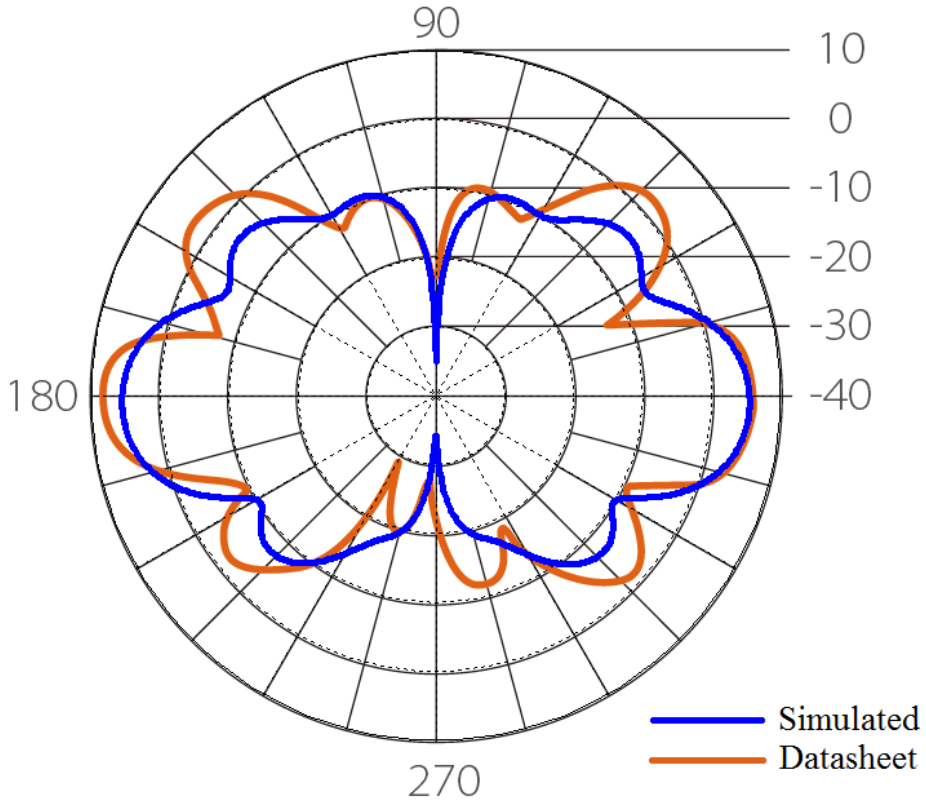

Figure 14: Vertical Plane Power Pattern (Radial Unit is dB).

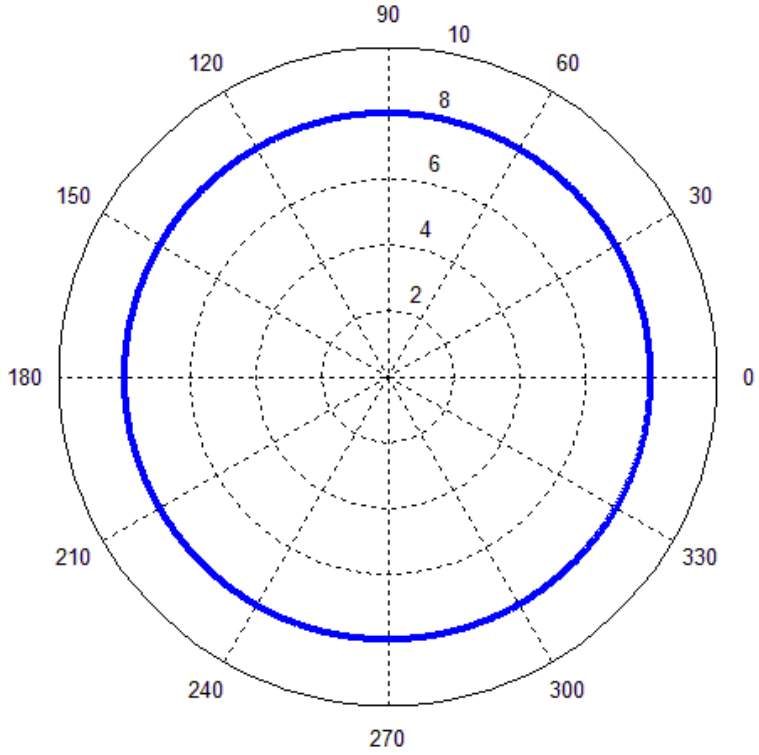

Figure 15: Horizontal Plane H-field Co-polarization Pattern (Radial Unit is dB).

3.6. Reflection Modelling

Reflections are normally modeled in the plane of incidence, which is the plane containing the incident, reflected, and transmitted rays (Figure 8). Many electromagnetics and wireless communications textbooks characterize the interaction taking place on the reflecting surface for both parallel and perpendicular polarizations [39, 48-51]. For this model, the rays are assumed to be travelling through free space and reflecting from the soil. It is also assumed that the receiving antenna and reflection point are in the far-field. In the far-field, $\vec{E}$ and $\vec{H}$ are related by

$$\vec{E}(\vec{r}) = \eta\vec{\mathrm{H}}(\vec{r}) \times \frac{\vec{r}}{r} \tag{15}$$

$$\vec{H}(\vec{r}) = \frac{1}{\eta}\frac{\vec{r}}{r} \times \vec{\mathrm{E}}(\vec{r}) \tag{16}$$

where η is the intrinsic impedance, $\vec{E}$ is the electric field (E-field) vector, $\vec{H}$ is the magnetic field (H-field) vector, $\vec{r}$ is the vector from the transmitting antenna to the point of interest, and r is the magnitude of $\vec{r}$. Equations 15 and 16 are good approximations when

$$r > \frac{2L^2}{\lambda} \tag{17}$$

where L is the maximum dimension of the antenna and λ is the wavelength of the electromagnetic wave in free space [44, pp. 44]. At 2.4 GHz and with an antenna length of 28.5 cm, $(2L^2/\lambda)$ = 1.30 m. For all of the flight tests, r > 1.30 m, which justifies the use of the far-field approximation in this research.

Because the E-field and H-field are related, only the E-field is considered in the reflection equations. At the point of reflection, the incident E-field in the antenna's frame, $\vec{E}_{IA}$, can be calculated using the antenna model. The E-field components in the antenna frame are then converted to the local frame using DCMs. However, the local frame may not align with the parallel and perpendicular polarization vectors, $\vec{z}_R$ and $\vec{x}_R$ respectively. Because the equations

defining this interaction are based strictly on parallel and perpendicular polarizations, the E-field must be broken into its parallel and perpendicular components. This is performed using two DCMs. Figure 16 defines the geometry of the reflection.

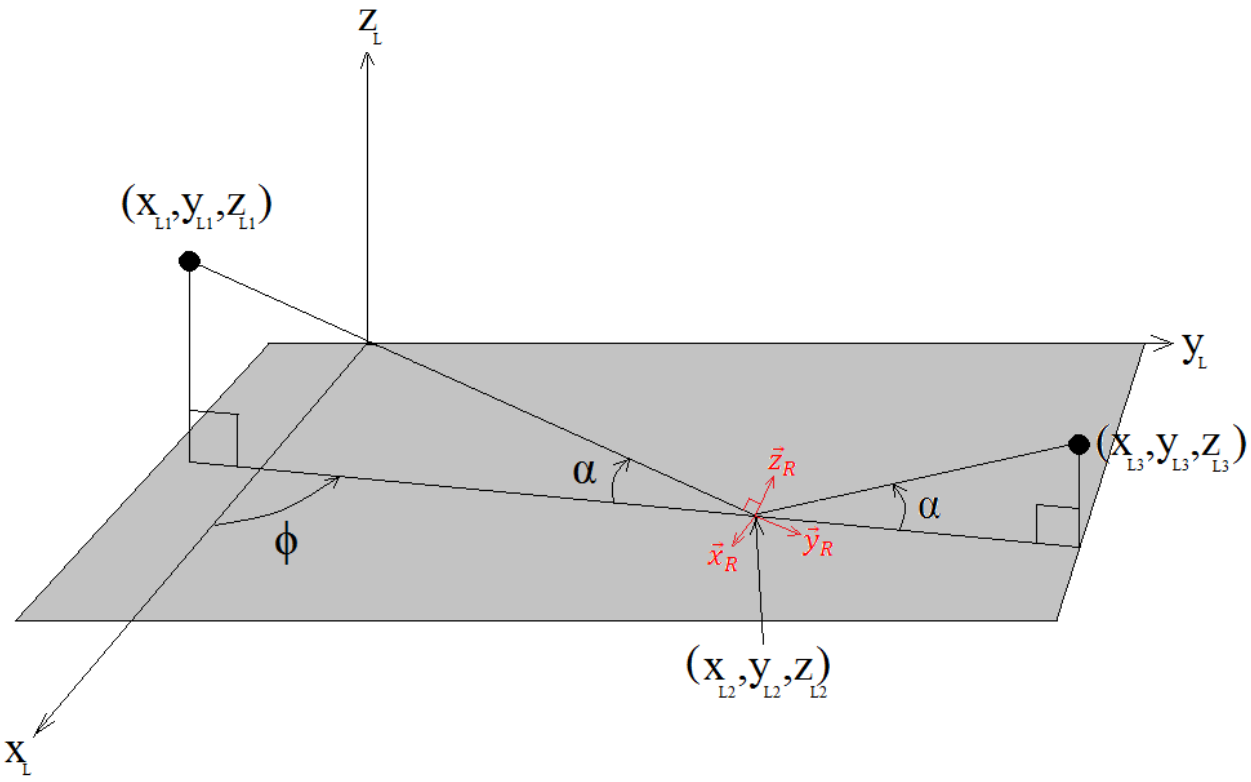

Figure 16: Reflection Coordinate Frame Shown in Local Frame.

To develop the DCMs, two rotations are necessary to align the local frame with the reflection frame $(\vec{x}_R, \vec{y}_R, \vec{z}_R)$. Figure 17 portrays the first rotation about the $\vec{z}_L$-axis.

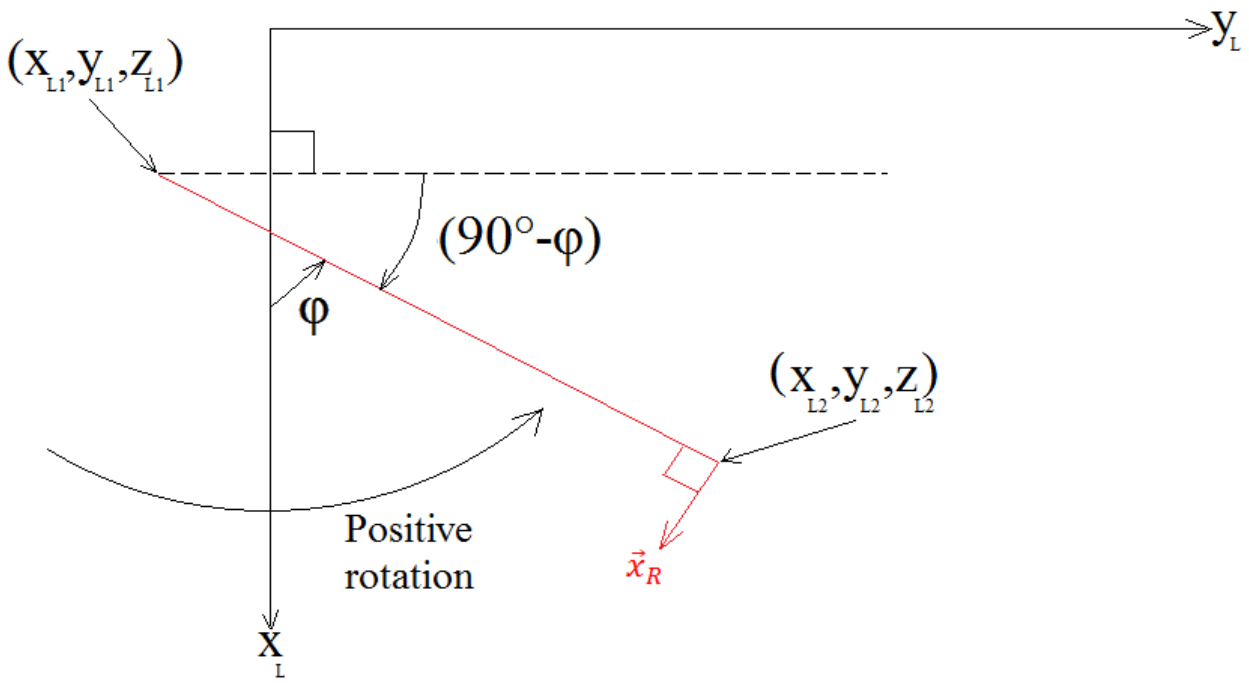

Figure 17: View from above *xy*-plane.

Using the φ calculated in Section 3.3, the amount of rotation about the $\vec{z}_L$-axis required to align $\vec{x}_L$ with $\vec{x}_R$ is -(90°- φ). The DCM used for this rotation is

$$\boldsymbol{R_z} = \begin{bmatrix} \cos(\varphi - 90°) & \sin(\varphi - 90°) & 0 \\ -\sin(\varphi - 90°) & \cos(\varphi - 90°) & 0 \\ 0 & 0 & 1 \end{bmatrix} \tag{18}$$

The second rotation is shown in Figure 18. This rotation is about the $\vec{x}_R$ axis by –α. The corresponding DCM is

$$\boldsymbol{R_{x1}} = \begin{bmatrix} 1 & 0 & 0) \\ 0 & \cos(-\alpha) & \sin(-\alpha) \\ 0 & -\sin(-\alpha) & \cos(-\alpha) \end{bmatrix} \tag{19}$$

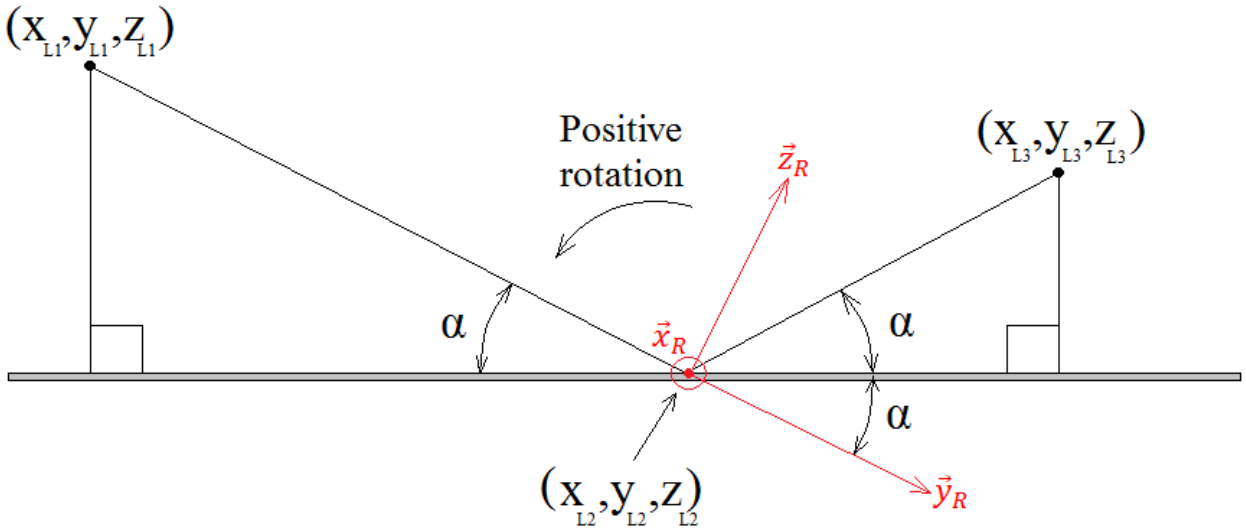

Figure 18: Plane of Incidence View.

The multiplication of these DCMs with the incidence E-field, $\vec{E}_{IL}$, yields

$$\vec{E}_{IR} = \boldsymbol{R_{x1}R_z}\vec{E}_{IL} \tag{20}$$

Where $\vec{E}_{IR}$ is the incidence E-field in the reflection frame. Once the incidence E-field is in the reflection frame, the depolarization matrix is used to calculate the strength and polarization of the reflected E-field in the reflection frame [39, pp. 117]. This matrix is given by

$$\boldsymbol{D} = \begin{bmatrix} \Gamma_{\perp} & 0 & 0 \\ 0 & 0 & 0 \\ 0 & 0 & \Gamma_{\parallel} \end{bmatrix} \tag{21}$$

Where $\Gamma_{\parallel}$ and $\Gamma_{\perp}$ are the parallel and perpendicular reflection coefficients respectively, and

$$\Gamma_{\parallel} = \frac{E_{RRx}}{E_{IRx}} = \frac{\eta_2 \sin\theta_t - \eta_1 \sin\alpha}{\eta_2 \sin\theta_t + \eta_1 \sin\alpha} \tag{22}$$

$$\Gamma_{\perp} = \frac{E_{RRz}}{E_{IRz}} = \frac{\eta_2 \sin\alpha - \eta_1 \sin\theta_t}{\eta_2 \sin\alpha + \eta_1 \sin\theta_t} \tag{23}$$

Where $\eta_{1,2}$ is the intrinsic impedance and is given by

$$\eta_{1,2} = \sqrt{\mu_{1,2}/\varepsilon_{1,2}} \tag{24}$$

where μ_1 is the permeability of free space which equals $4\pi \times 10^{-7}$ H/m; ε_1 is the permittivity of free space which equals 8.854×10^{-12} F/m; μ_2 is the permeability of the soil and is normally equal to the permeability of free space [52]; and ε_2 is the permittivity of the soil and for simplicity equal to $3.4 \times \varepsilon_1$ [51, pp. 35]. This simplification is made because ground samples at the flight area were not analyzed and the added complexity of having a complex ε_2 (real and imaginary parts) may not add substantial accuracy to the solution. This simplified case is known as lossless reflection. Before equations 22 and 23 can be used, the transmission angle, θ_t, must be solved using Snell's Law:

$$\theta_t = 90° - \sin^{-1}\left(\sqrt{\frac{\mu_1 \varepsilon_1}{\mu_2 \varepsilon_2}}\right)\sin(90° - \alpha) \tag{25}$$

The reflected field in the reflection frame, $\vec{E}_{RL}$,is given by

$$\vec{E}_{RR} = \boldsymbol{D}\vec{E}_{IR} \tag{26}$$

The next step is to compute the reflected field in the local frame. Parallel component of the reflected field does not coincide with the reflection frame's $\vec{z}_R$. To align the local frame with the perpendicular and parallel components of the reflected field, the first rotation is the same, but the second rotation is about the $\vec{x}_R$ axis by +α. This results in the following DCM:

$$\boldsymbol{R_{x2}} = \begin{bmatrix} 1 & 0 & 0) \\ 0 & \cos(\alpha) & \sin(\alpha) \\ 0 & -\sin(\alpha) & \cos(\alpha) \end{bmatrix} \tag{27}$$

The equation to compute the reflected E-field in the local frame from the incidence E-field in the local frame is given by

$$\vec{E}_{RL} = (\boldsymbol{R_{x2}R_z})^T \boldsymbol{D R_{x1} R_z} \vec{E}_{IL} \tag{28}$$

The reflected ray undergoes further attenuation after reflecting from the soil. Based on the concepts covered in [39, pp. 120-122], the E-field of the reflected ray in the local frame at the intersection with the origin of the antenna's frame is given by

$$\vec{E}_{2L} = \frac{d_1}{d_1 + d_2} \vec{E}_{RL} e^{-jk_0 d_2} \tag{29}$$

where d_1 and d_2 are defined in Section 3.3. $\vec{E}_{RL}$ was defined in Section 3.6. Note that $\vec{E}_{RL}$ has complex components and that multiplication by $e^{-jk_0 d_2}$ results in a phase shift of these components. k_0 is the wavenumber of free space which is given by

$$k_0 = \frac{\omega}{c} rad/m = \frac{2\pi f}{c} rad/m \tag{30}$$

where c is the speed of light in free space, and f is frequency of the radiated field (2.4 GHz for this research).

3.7. LOS Ray

To calculate the E-field for the LOS ray at the receiving antenna, the transmitting antenna model and DCMs, which were previously developed, are used. First, the vector pointing from the transmitting antenna to the receiving antenna is calculated in the local frame using

$$\vec{V}_{L1 \to L3} = \begin{bmatrix} x_{L3} \\ y_{L3} \\ z_{L3} \end{bmatrix} - \begin{bmatrix} x_{L1} \\ y_{L1} \\ z_{L1} \end{bmatrix} \tag{31}$$

Then the DCMs developed in Section 3.4 are used to convert the vector, $\vec{V}_{L1 \to L3}$, into the transmitting antenna's frame. Given this vector, the E-field is then determined in the transmitting antenna's frame. The E-field is converted into the local frame using four DCMs corresponding to the transmitting antenna, and finally into the receiving antenna's frame using four DCMs corresponding to the receiving antenna.

3.8. Receiving Antenna Model

To compute the received power, the 3-D patch model developed in Section 3.5 is again used. In the case of receiving antenna, the radiated field incidence on the antenna's surface will induce current flow in the antenna. Code was developed by Makarov in [44] to handle the incidence of a single plane wave on the surface of an antenna; however, the two-ray model requires the superposition of two plane waves on the antenna surface. The far-field approximation is again used.

The E-field of the LOS ray and reflected ray in the local frame at the intersection with the origin of the antenna's frame are $\vec{E}_{1L}$and $\vec{E}_{2L}$respectively. These E-fields are transformed into the receiving antenna's frame using the DCMs developed in Section 3.4. In the antenna frame, the two rays intersect at the origin of the frame and consequently at the feeding point of the antenna. In the far-field, these rays are approximated using uniform plane waves. Figure 19 shows the incidence of a single plane wave on an antenna. This plane wave changes in both phase and amplitude along the antenna. Since the dimensions of the antenna are small, the changes in amplitude are negligible; however, the change in phase is not negligible and is computed using the distance, *d*, the wave front moves in the direction of $\vec{k}$. The wave vector, $\vec{k}$, is pointed in the same direction as the ray and has a magnitude of k_0 for Section 3.6. The distance, *d*, is the projection of $\vec{r}$ onto $\hat{k}$ which is the unit vector in the direction of $\vec{k}$. Multiplying k_0 by *d* gives the amount of phase shift in radians. Using complex numbers, the E-field at each point along the antenna produced by a single ray is

$$\vec{E}(\vec{r}) = \vec{E}_0 e^{-j\vec{k}\cdot\vec{r}} \tag{32}$$

Where $\vec{E}_0$ is the E-field at the origin, and $(\cdot)$ denotes the dot product. This approach was used by Makarov and is described in [53].

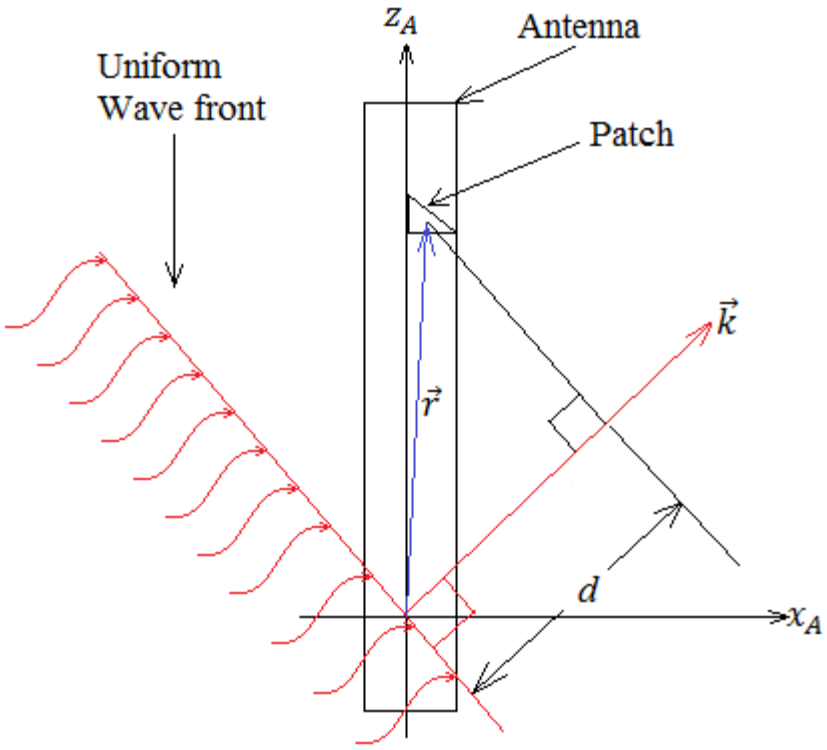

Figure 19: Incidence Model Geometry.

Since two waves are arriving at the antenna, the E-field created by each wave front is first computed and then added together at each patch along the antenna. The current in the antenna is then calculated using Makarov's code, and the received power is estimated using the current through the feed-point and the real part of the antenna's impedance. The received power is given by

$$RSS = \frac{1}{2} Real(Z) I^2 \tag{33}$$

Where Z is the complex impedance of the antenna (which is 227.73+j9.6215 Ω from simulation), and I is the amplitude of the steady-state alternating current. Note that the real part of the impedance which was calculated using the 3-D patch model is higher than the datasheet specified (50 Ω) [47]. This is due to imperfections in the modeling of the antenna.

3.9. Validation Testing

In order to ensure that the algorithm was working properly, several tests were performed in simulation. The first, three tests were done at high altitude (10 km) to ensure both the transmitting and receiving antenna models were working correctly. In the first test, the transmitting and receiving aircraft were positioned at local coordinate positions (0, 0, 10000) m and (0, 100, 10000) m respectively. Both aircraft were pointed in the *x*-axis direction. The transmitting plane performed a rotation about the roll axis (Figure 20). Figure 21 is RSS pattern generated as the transmitting aircraft rotates. This is identical to Figure 14 and proves that the transmitting antenna model is working properly. The plot is offset by 80.6774 dB to prohibit negative dB values, which causes trouble when using the MATLAB polar function.

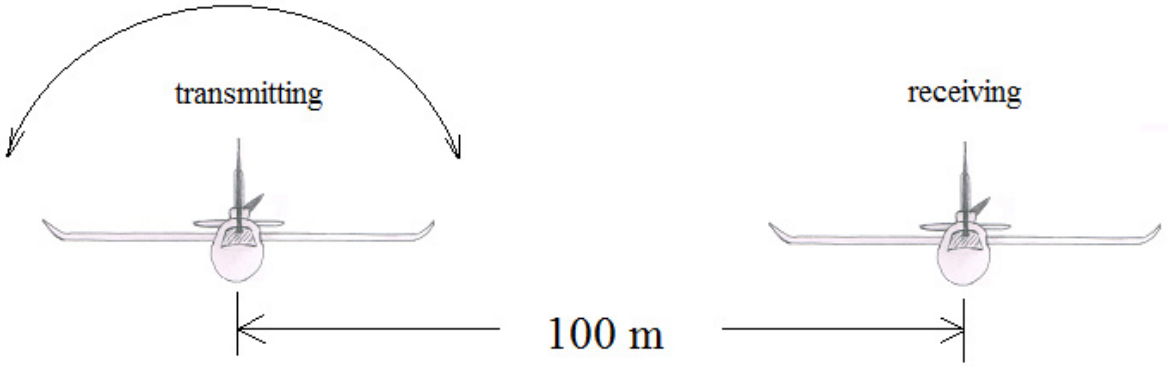

Figure 20: Test Setup 1 for Vertical Plane Power Pattern Analysis.

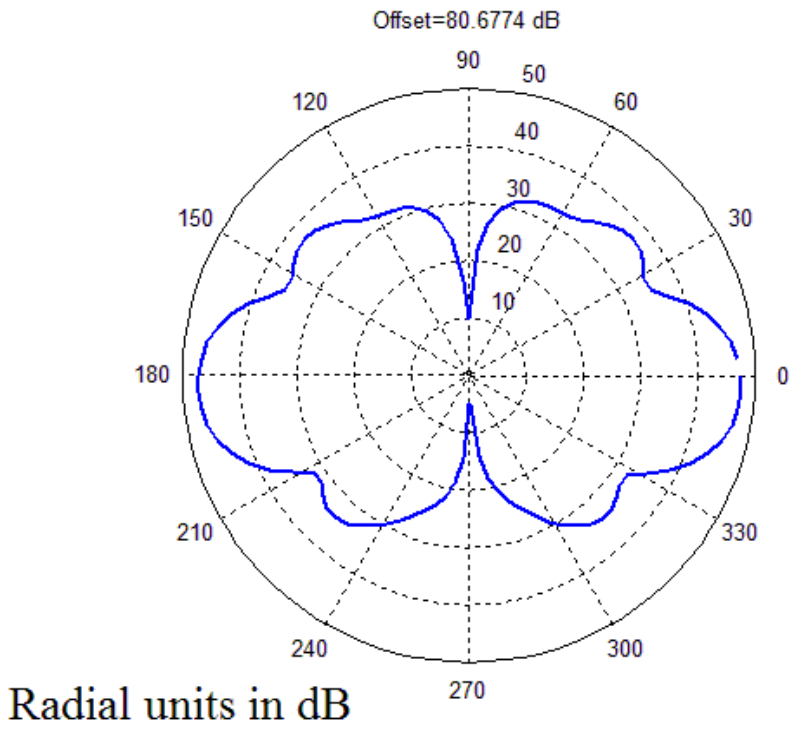

Figure 21: Validation Vertical Plane Power Pattern.

Similarly the receiving aircraft was rotated (Figure 22), and the pattern seen in Figure 21 was again repeated. This repetition follows in accordance with the reciprocity theorem [54, pp. 147-150] and proves that the receiving antenna model was functioning properly.

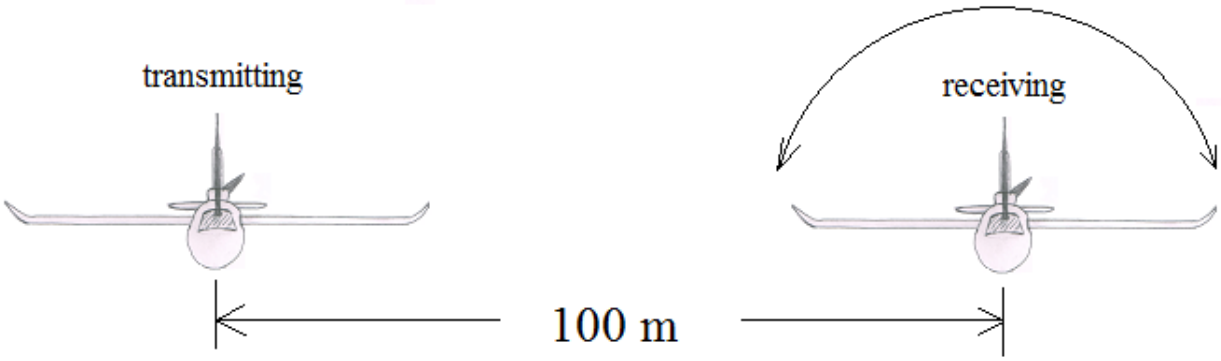

Figure 22: Test Setup 2 for Vertical Plane Power Pattern Analysis.

The third test looked at polarization mismatch. The transmitting and receiving aircraft were positioned at local coordinate positions (0, 0, 10000) m and (100, 0, 10000) m respectively.

Both aircraft were pointed in the *x*-axis direction. The receiving plane was rotated about the roll axis to create a polarization mismatch (Figure 23).

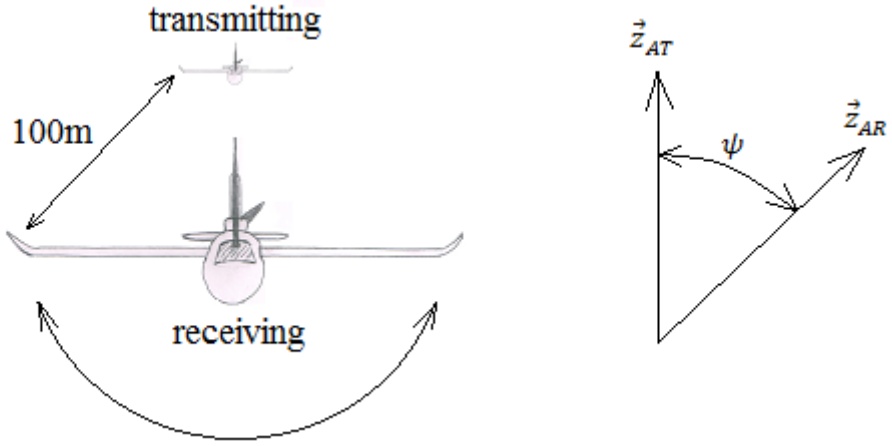

Figure 23: Test Setup for Polarization Mismatch Analysis.

According to [54, pp. 76], the polarization loss factor for linear polarization is given by

$$PLF = |\cos(\psi)|^2 \tag{34}$$

where the angle ψ is defined in Figure 23 above. For comparison of the simulated RSS to the theoretical RSS, the theoretical RSS is given by

$$RSS_{PLF} = 10\log(|\cos(\psi)|^2) + \max(RSS_{dB} + Offset) \tag{35}$$

where RSS_{dB} is the received signal strength in dB that is computed from the simulation, and $Offset$ is the value added to the RSS value to avoid plotting of negative radii in the polar plot. In addition, RSS_{PLF} values which fall below zero, which takes place when ψ goes to 90° or -90°, are reset to zero. This prevents RSS_{PLF} from going towards negative infinity. In Figure 24, the simulated RSS is shown in blue, and the RSS computed from Equation 35 is shown in red. The red and blue curves show significant overlap proving that the simulation model is functioning properly. The curves do not overlap at every angle because the antenna is not perfectly linearly polarized.

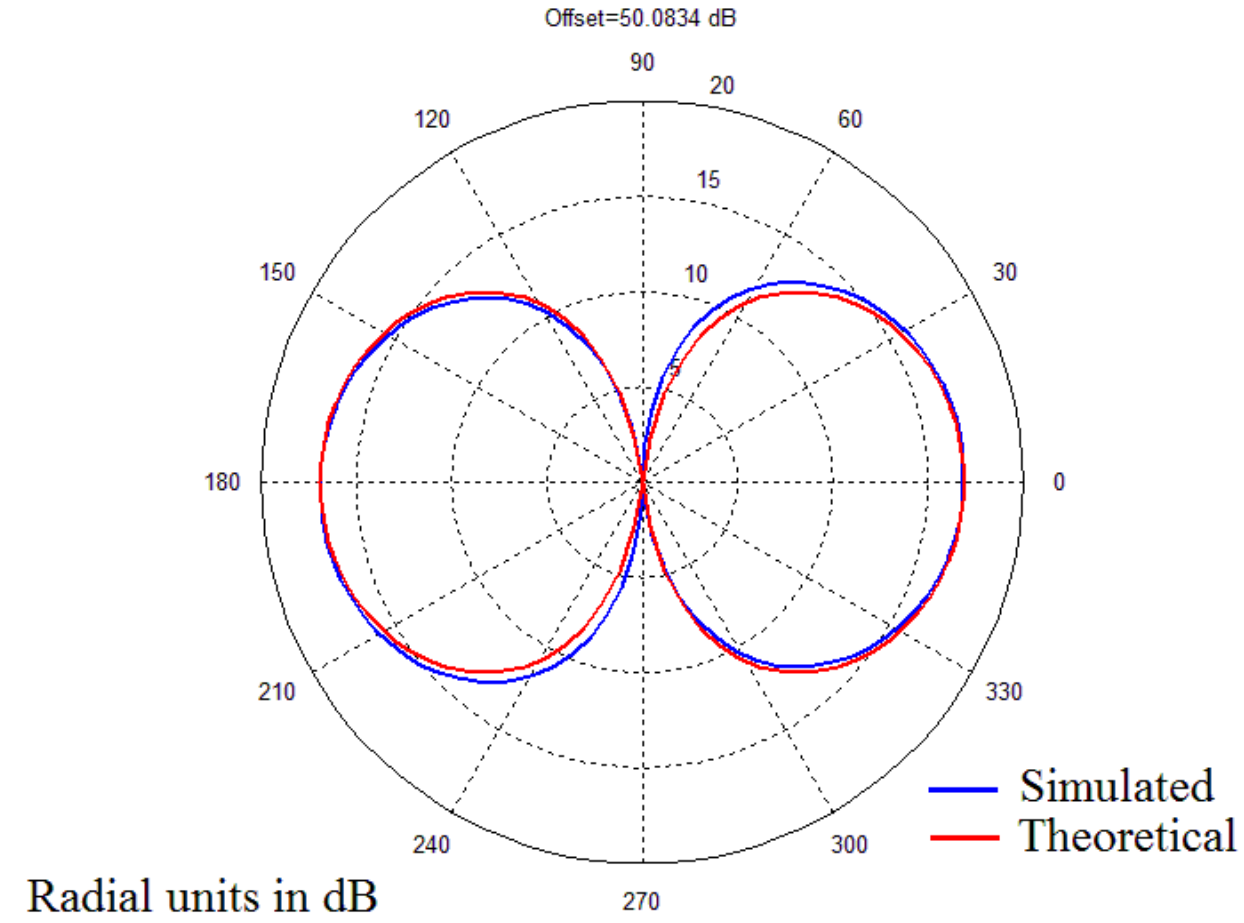

Figure 24: Simulated and Theoretical RSS vs. Polarization Mismatch Angle.

The final three tests are performed at 1.50-m altitude with the transmitting aircraft at the coordinate (0, 0, 1.50) m. This ensures that the effects of ground reflection will be observable in the RSS solution. For the first test, both antennas are perpendicular to the ground plane, and the receiving aircraft is moved along the y-axis direction from (0, 0, 1.50) m to (0, 70, 1.50) m. Figure 25 shows the simulated RSS value in blue, and the RSS value predicted by the Friis equation [44, pp. 81] is shown in green. The Friis equation is given by

$$RSS = P_T \frac{G_T G_R}{(4\pi r)^2} \lambda^2 \tag{36}$$

where P_T is the transmitted power in watts; G_T is the linear gain of the transmitting antenna; G_R is the linear gain of the receiving antenna; λ is the wavelength of the electromagnetic wave; and r is the distance between the antennas.

Equation 36 in dB is given by

$$RSS_{dB} = 10\log_{10}(P_T G_T G_R \lambda^2) - 20\log_{10}(4\pi) - 20\log_{10}(r) \quad (37)$$

Only the last term on the right side of Equation 37 varies with distance. The rest of the terms remain constant. Therefore, Equation 37 can be written as

$$RSS_{dB} = C - 20\log_{10}(r) \quad (38)$$

Where C is a constant. At a distance of one meter, the last term of Equation 38 cancels out, and the constant C can be solved for. In Figure 25, the simulated RSS is above and below the Friis value due to constructive and destructive interference created by the ground reflection. This proves that the algorithm is combining both the LOS and reflected rays for vertically oriented antennas.

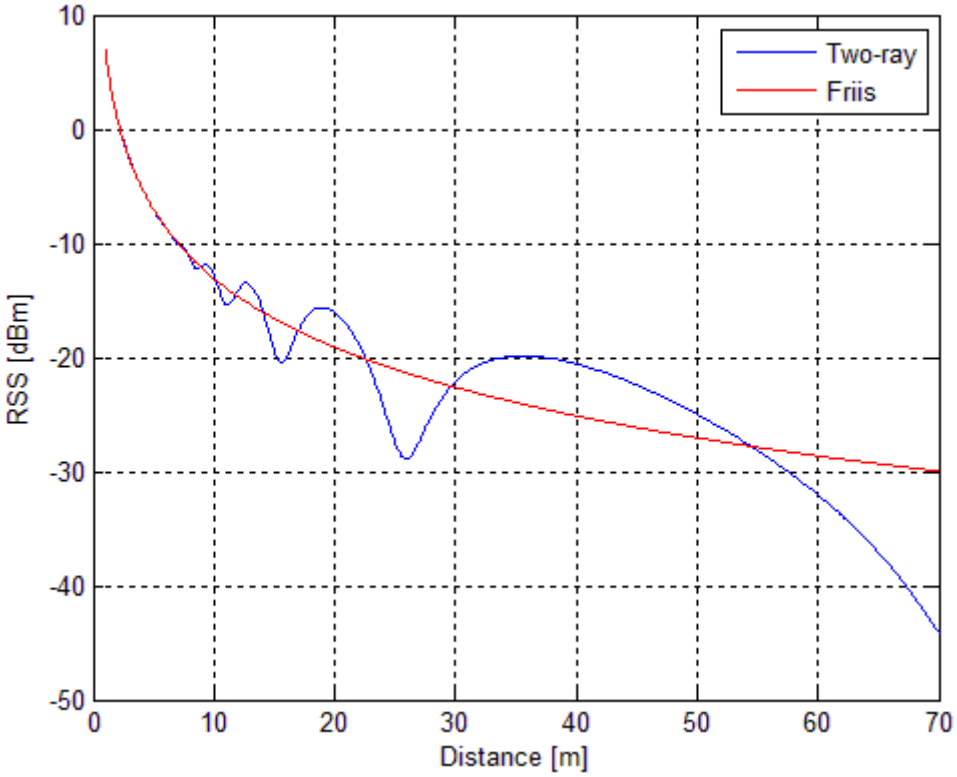

Figure 25: RSS vs. Distance (Height = 1.50 m and Vertical Polarization).

The second test was similar to the previous test. However, this time the antennas were oriented parallel to the ground plane and one another with the direction of highest gain pointed towards each other. Figure 26 again shows the effects of constructive and destructive interference and resembles [41, Fig. 6(c)] which was computed for the same antenna height and orientation using a different method. This proves that the algorithm is properly combining both the LOS and reflected rays for antennas oriented parallel to the ground plane.

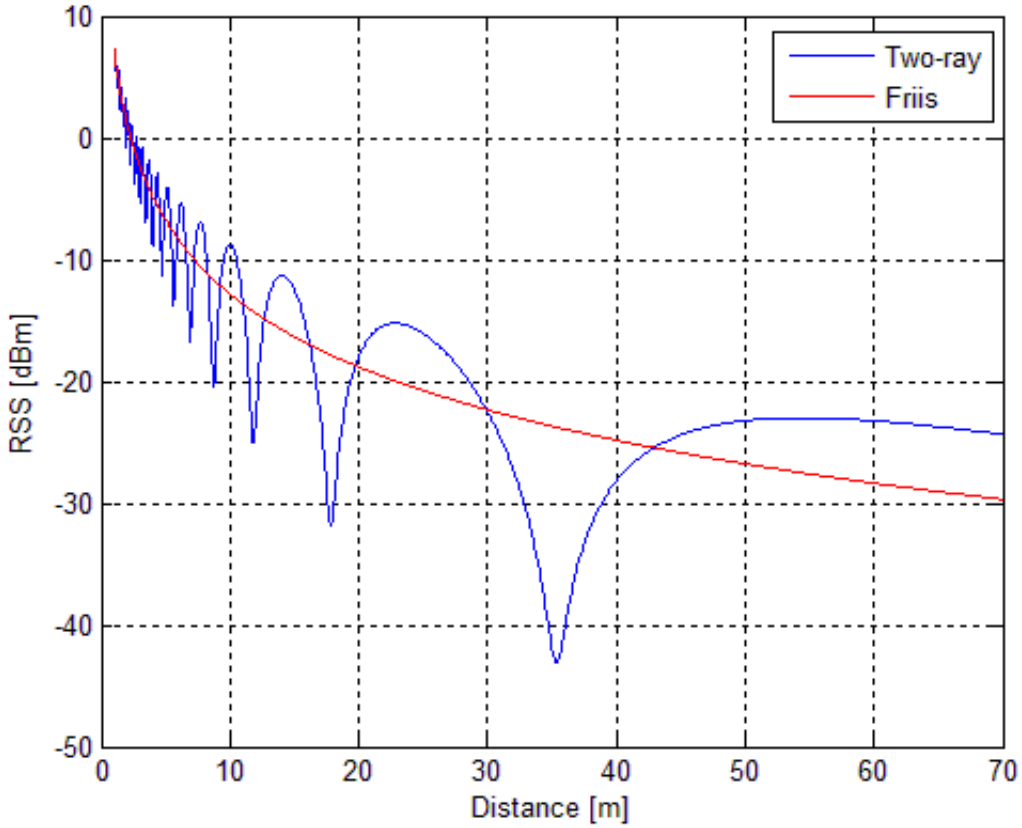

Figure 26: RSS vs. Distance (Height = 1.50 m and Horizontal Polarization).

In the final test, both antennas were placed vertically with respect to the ground plane, and the transmitting antenna was again placed at (0, 0, 1.5) m. The receiving antenna was moved to 40,000 positions in *x*- and *y*-axes directions while maintaining a height of 1.5 m above ground level. This produced the interference pattern seen in Figure 27 and proved that the algorithm is combining the two rays in the same manner in all directions.

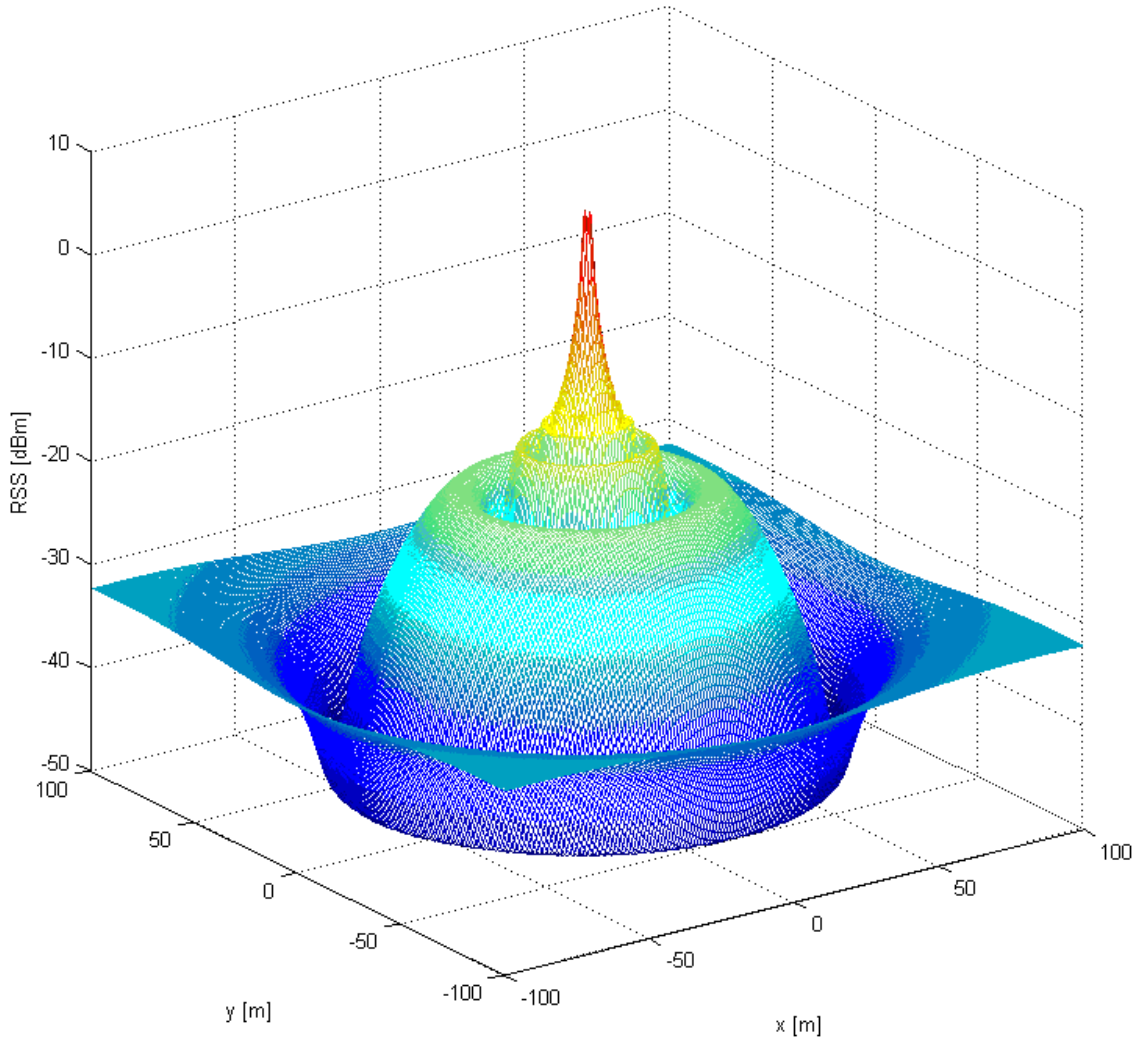

Figure 27: RSS Pattern Produced by Interference (Height = 1.50 m and V-Pol.).

3.10. Performance Evaluation

To evaluate the performance of the model, the results section compares the two-ray model to the data attained from flight-testing. In addition, this section evaluates a one-ray model using only the LOS ray. This model is a simplification of the two-ray model where the reflected ray is removed from the calculation of E-field at the receiving antenna. Furthermore, this section also evaluates the Friis model (Equation 38) and compares it to the other models. To rate the performance of the models, the results section displays the error between the simulated RSS and

measured RSS and shows the bias and standard deviation of the error with respect to the distance between antennas. A bias of zero means that the model is accurate and on average will produce the right result. A lower standard deviation means the model has greater precision. Note the precision and accuracy of the flight data affects the precision with which the simulated results can match the measured results. If errors are present in the measurement of location and attitude, the output of model will also have errors.

Before evaluation, all the models require calibration. The algorithm sets the input to the one-ray and two-ray models to a 10 V amplitude sinusoid. By varying the voltage amplitude the model can be calibrated; however, adding a constant value to the simulated RSS is much faster and produces the same result. The calibrated RSS equation is given by

$$RSS_{dB} = E + 20\log_{10}(P_R) \tag{39}$$

Where P_R is the simulated RSS in watts, and E is a constant that is chosen to reduce the bias of the error between simulated RSS and measured RSS. Similarly, C in Equation 38 is also chosen to reduce the bias of the error for the Friis model.

3.11. Summary

This chapter presented the two-ray model that simulates the airborne wireless environment. To determine the radiation characteristics of the transmitting antenna, MATLAB codes developed by Sergey N. Makarov were used to analyze a 3-D model of the research antenna made from 2-D triangular patches. DCMs were developed to transform vectors between coordinate frames, and a lossless reflection model was developed to determine the strength and polarity of the reflected ray. To determine the power generated at the receiving antenna, codes written by Makarov and the 3-D model developed in this chapter were again utilized. This model was tested and performed as anticipated showing the effects of polarization, directional gain, and

interference. Lastly, statistical evaluation of the error between the simulated RSS and measured RSS was proposed as the method for evaluating the performance of the one-ray, two-ray, and Friis models.

IV Analysis and Results

4.1. Chapter Overview

This chapter compares the one-ray, two-ray, and Friis model results against data collected from several flight test. In all sections, the data is analyzed when the required aircraft is/are in flight. Section 4.2 discusses the yaw angle correction applied to the flight data. Section 4.3 evaluates the performances of the models in the air-to-air (AtoA) scenario and provides the calibrated equations for the models. Sections 4.4 and 4.5 analyze the ground-to-air (GtoA) and air-to-ground (AtoG) scenarios and identify key features of the results. Section 4.6 combines the data from all scenarios and provides a more in depth statistical analysis. Section 4.7 summarizes the results found in this chapter.

4.2. Yaw Angle Correction

In Sections 4.2-4.4, the flight data is analyzed using both the yaw angle provided by the autopilot and the yaw calculated from the direction of the vector between consecutive GPS locations. Early in the analysis, it was found that the yaw angle provided by the autopilot was unreliable before the aircraft was in flight. The yaw angle drifted while the aircraft was stationary on the ground (Figure 83 in Appendix E). Even during flight, the yaw angle sometimes points in a direction off the flight path. This is observed in Figure 28, where the arrows shown are in the directions of the axes of the antenna's frame as defined in Section 3.4. The deviation of $\vec{x}_A$ from the flight path could be due to the high winds experienced the day of flight-testing. However, the locations at which these deviations occur and direction of $\vec{x}_A$ at these locations led to the conclusion that the heading solution of the autopilot was inaccurate. This could be due to the ArduPlane program or the inaccuracies associated with the magnetometer. Figure 29 shows the flight path overlaid with the antenna's frame and using GPS positions to

determine the yaw angle. In this case, $\vec{x}_A$ deviates less from the flight path than that seen in Figure 28.

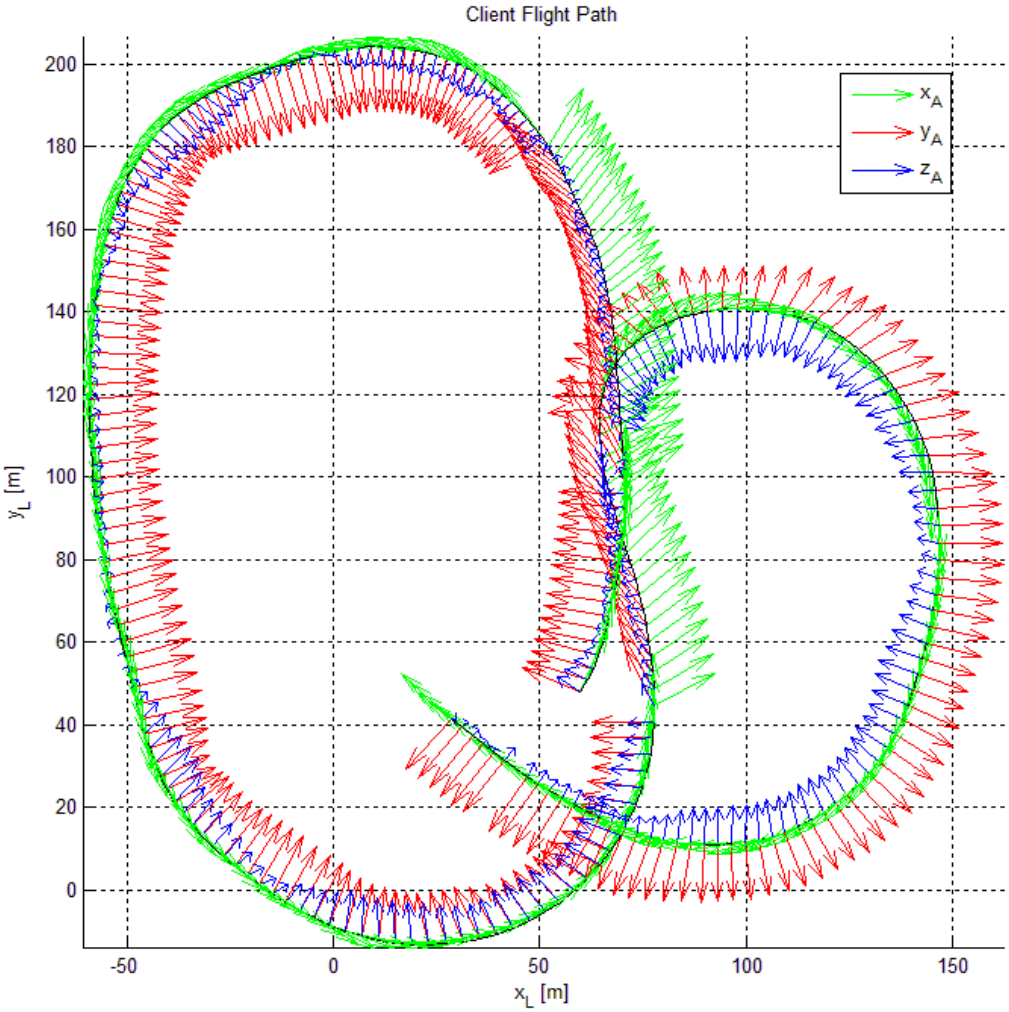

Figure 28: Flight Path Overlaid with Antenna's Frame using Autopilot Yaw.

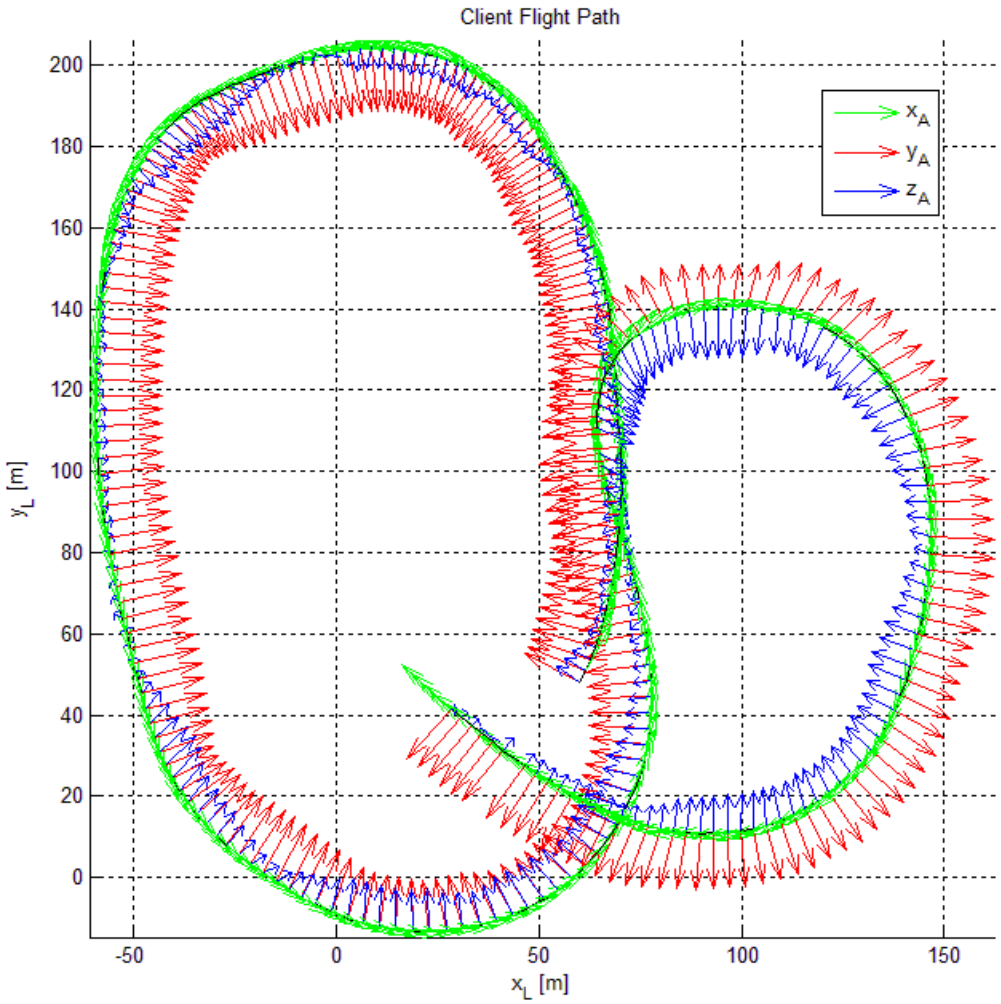

Figure 29: Flight Path Overlaid with Antenna's Frame using GPS Based Yaw.

4.3. Results of Air-to-Air Scenario

In the AtoA Scenario, both aircraft are in flight for the portion of the data analyzed (Figure 61 in Appendix E). The case for which autopilot yaw (sometimes referred to as raw heading in this thesis) is examined first. It is important to describe here how the following graphs were produced. The line of sight distance between each aircraft was first computed for each data entry. A scatter plot was then used to gain an understanding of the error between the simulated and measured RSS (Figure 60 in Appendix E). Anomalies were found in the data where the RSS value was either lower than the detectable limits of the WLAN module or much higher than

anticipated. For this reason, threshold lines were drawn using Equations 40 and 41, and data points outside the threshold lines were ignored.

$$error_{max} = -\frac{distance}{20} + 35 \tag{40}$$

$$error_{min} = \frac{distance}{20} - 35 \tag{41}$$

Where *distance* is the LOS distance between the antennas. Figure 30 shows the results of the statistical analysis on the data found in the scatter plot (Figure 60 in Appendix E). In Figure 30, 30, 31, and 32, the error is examined for every 20-m section of distance (0-20 m, 20-40 m, and so on), the bias and standard deviation are graphed at the midpoint of each section. The histogram shows the number of data points recorded within each 20-m section. These figures show the relationship between error and distance.

The Friis equation was calibrated to drive the bias at 250 m to zero and is given by

$$RSS_{dB} = -36.638 - 20\log_{10}(r) \tag{42}$$

Where r is the distance between the antennas. The one-ray and two-ray models were also calibrated at 250 m to reduce the error bias to zero, and Equation 43 is used by both:

$$RSS_{dB} = -33.5 + 20\log_{10}(P_R) \tag{43}$$

Where P_R is the simulated RSS in watts. These equations are used in the remaining analysis. Since the wireless module will only report RSS for the last received packet, values that fall below -92 dBm (the lowest value the wireless module can measure) are set equal to -92 dBm. Figure 30 shows a tendency of the Friis equation to estimate above the measured RSS value at distances under 150 m. This tendency is due in part to the Friis equation not taking into account the variations in antenna gain due to polarization and propagation direction.

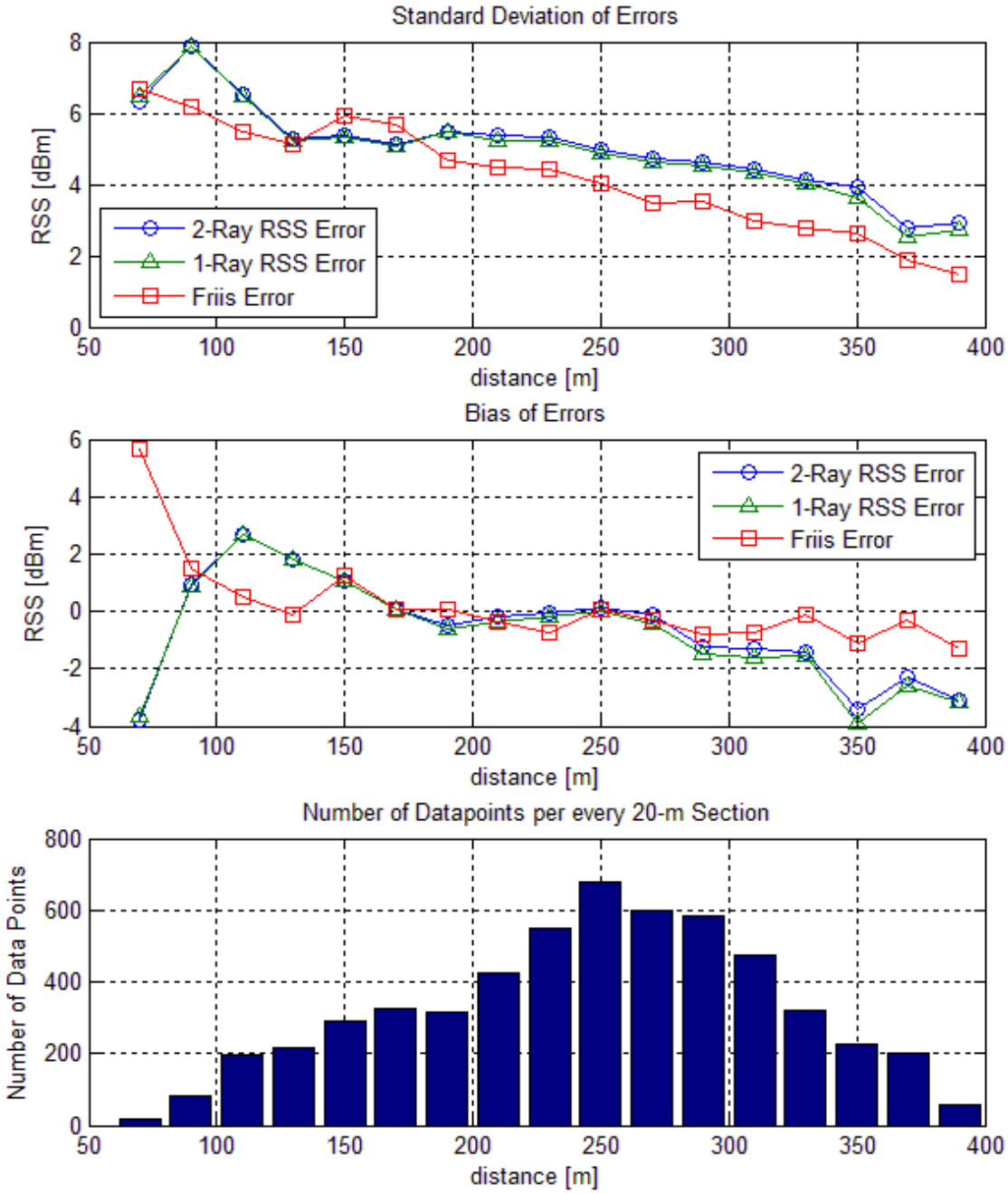

Figure 30: Statistical Analysis of AtoA Scenario with Raw Heading.

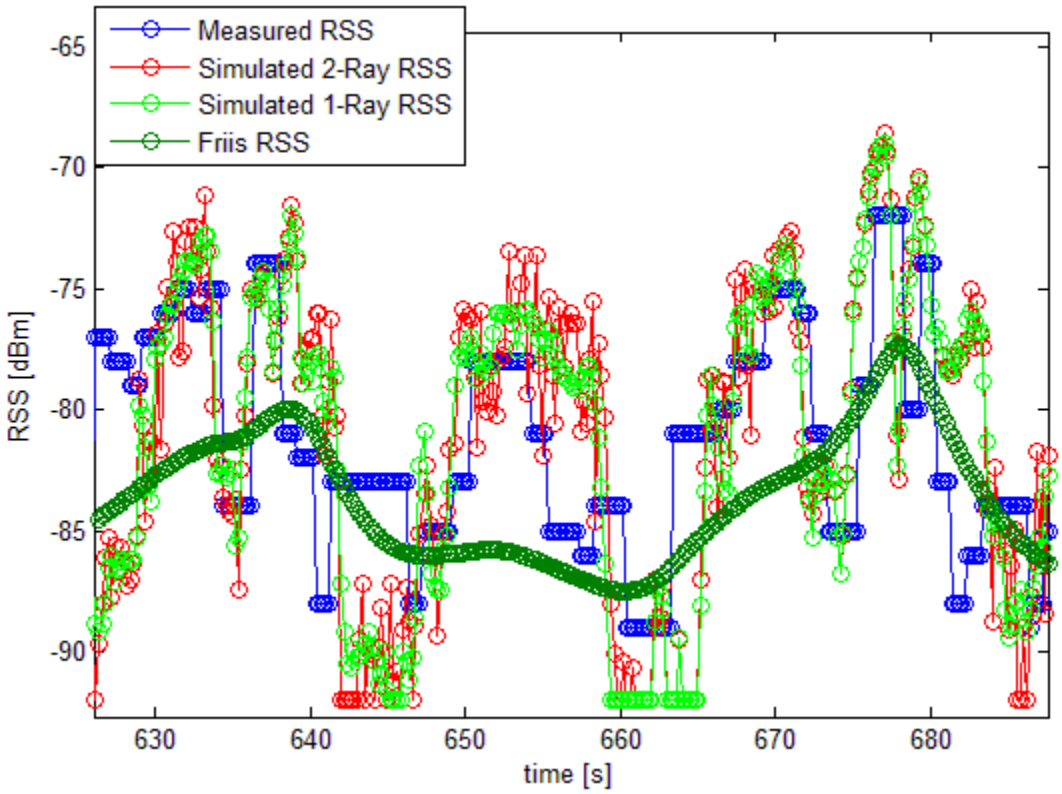

Figure 31: Snapshot of RSS vs. Time for AtoA Scenario using Raw Heading.

For all distances, the Friis equation produced less error bias than the one-ray or two-ray models, and its standard deviation was less for most distances. However, as shown in Figure 29, the one-ray and two-ray models are able to track variations in the RSS that the Friis equation cannot. The ability to track the variations makes these models more susceptible to the errors in attitude and distance measurements. The heading or yaw angle often experiences the largest errors of all the attitude measurements. These errors are most likely what leads to the higher standard deviation in comparison to the Friis model.

These errors are not associated with aircraft vibration; the sensor inputs are run through digital low pass filters in the ArduPlane program. This removes the high frequency portion of the signal coming from the sensors and is necessary to remove the effects that neighboring electronics and motors cause on the magnetometer. Nevertheless, the flight data was passed

through a first-order low-pass 1 Hz filter, but this method showed no improvement over using the raw data from the autopilot.

The AtoA flight was again analyzed with the autopilot yaw angle replace with a GPS based heading. For this case, the standard deviation of the error for the one-ray and two-ray models was reduced for a majority of the distances; the bias however was better at some distance and worse at others (Figure 65 in Appendix E).

4.4. Results of Ground-to-Air Scenario

For the GtoA Scenario, the aircraft containing the access point remained stationary on the ground while the aircraft containing the client was flown. Figure 32 shows that for a majority of the data entries the distance between the antennas was less than 200 m. For a majority of the distances, the one-ray and two-ray models have less error bias than the Friis model. For distances that have more than fifty data entries, the standard deviation of error for the one-ray and two-models varies by approximately one dBm above and below that of the Friis model. The use of a GPS based heading does not appear to perform any better (Figure 78 in Appendix E).

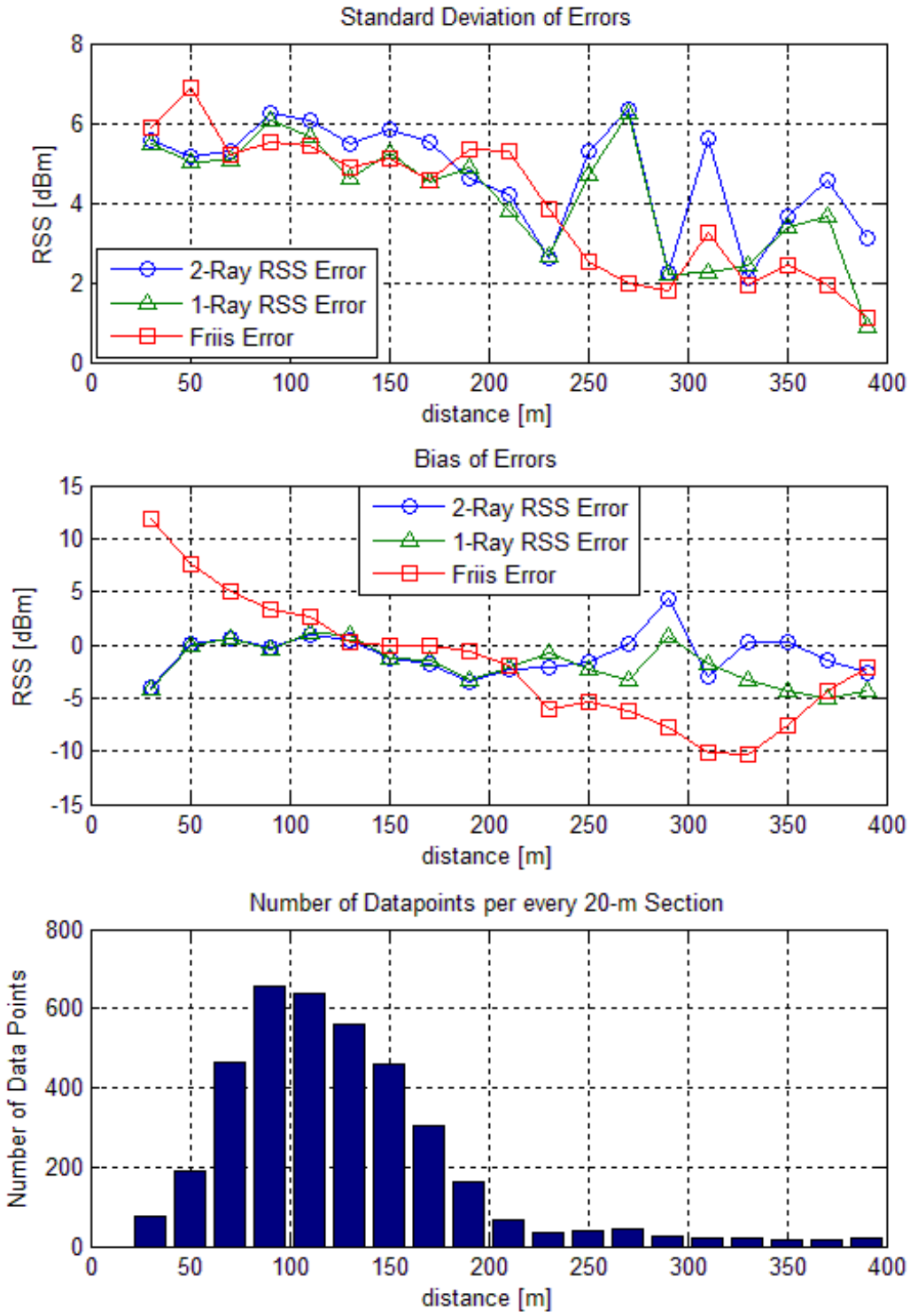

Figure 32: Statistical Analysis of GtoA Scenario with Raw Heading.

4.5. Results of Air-to-Ground Scenario

For the AtoG Scenario, the aircraft containing the client remained stationary on the ground while the aircraft containing the access point was flown. Figure 33 shows a majority of the data entries are around a 170-m separation distance between antennas. In this case, the error bias for the Friis model is again higher in magnitude than the one-ray or two-ray models for distances less than 270 m. For a majority of the distances, the standard deviation for the Friis model error is less than that for the one-ray or two-ray. The use of a GPS based heading does not appear to perform any better (Figure 91 in Appendix E).

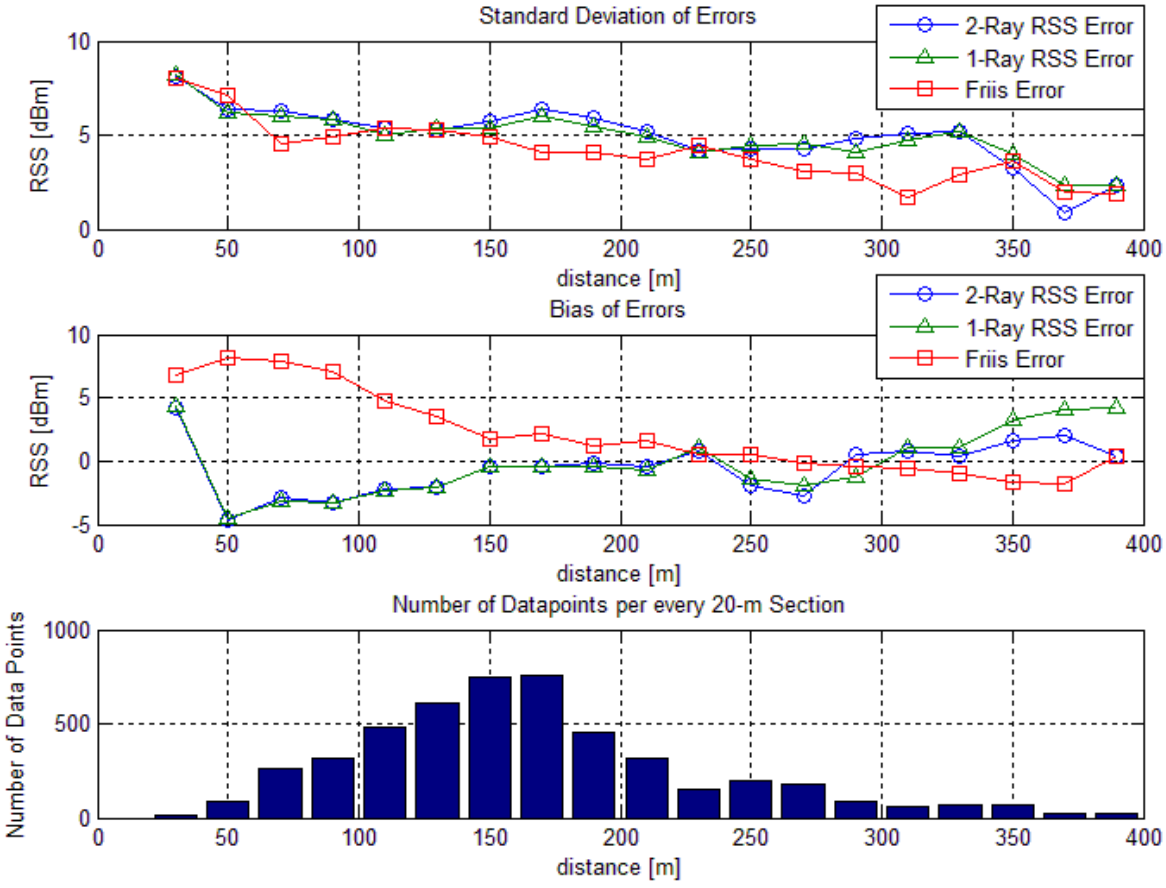

Figure 33: Statistical Analysis of AtoG Scenario with Raw Heading.

4.6. Combined Result of All Scenarios

Due to the limited data set available for each scenario, the flight data from all 3 scenarios were combined, and the results are shown in Figure 34.

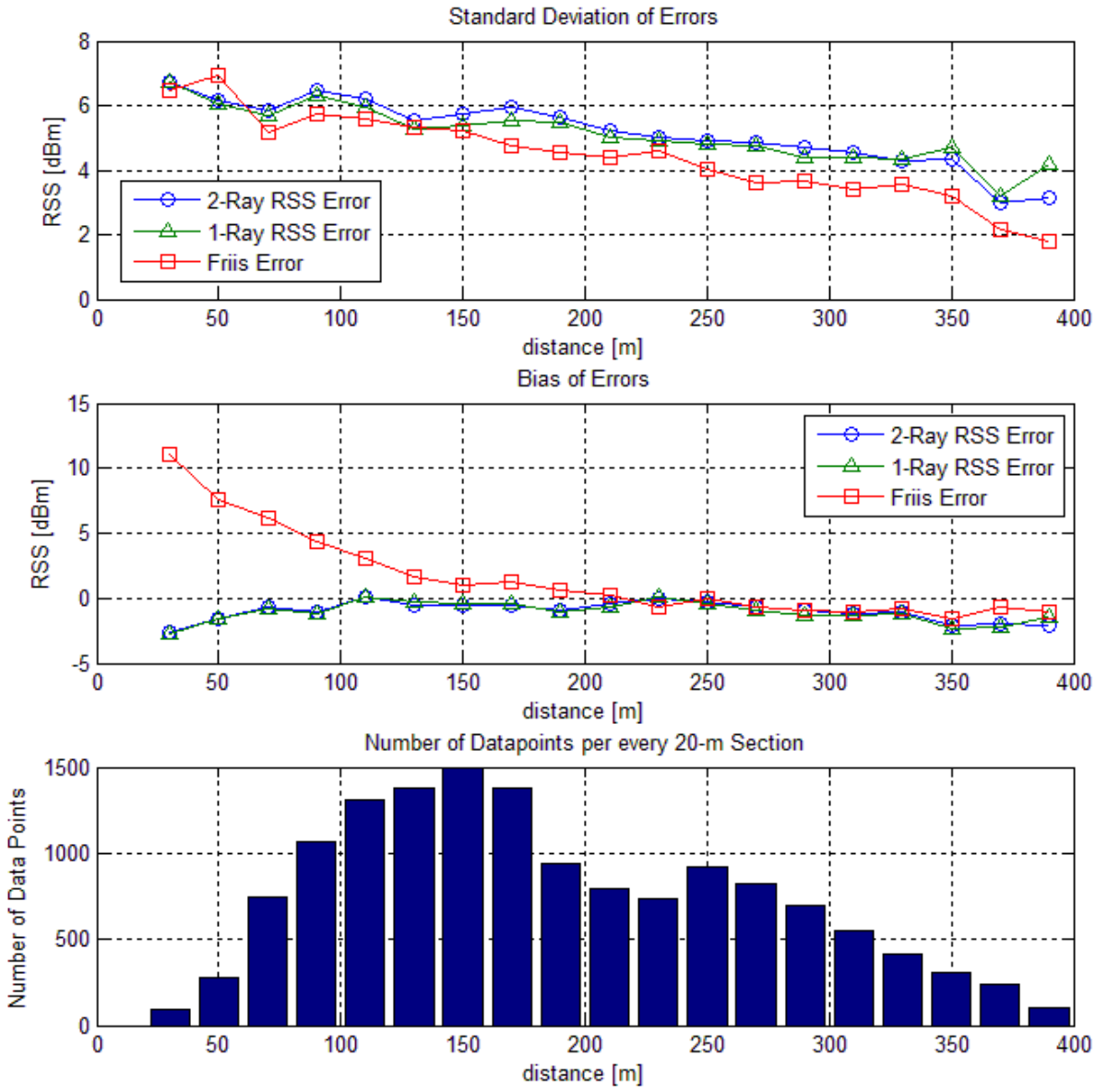

Figure 34: Statistical Analysis of All Scenarios with Raw Heading.

For a majority of the distances, the error bias of one-ray and two-ray is less than the error bias of the Friis model. The exception is at distances greater than 330 m where the number of data

entries is less than 400 per 20-m section. The standard deviation of the error for the one-ray and two-ray models is greater for a majority of the distances than the Friis model.

As stated earlier, the tendency of the Friis equation to estimate above the measured RSS value is due in part to the Friis equation not taking into account the variations in antenna gain due to polarization and propagation direction. To prove that this is indeed true, the elevation angle is first defined, and then the error is evaluated with respect to the elevation angle between the aircraft.

Figure 35 show the geometry of the elevation angle. The ground distance is given by

$$\text{Ground Distance} = \sqrt{(x_{L3} - x_{L1})^2 + (y_{L3} - y_{L1})^2} \tag{44}$$

Where x_{L1}, x_{L3}, y_{L1}, and y_{L3} are defined in Section 3.3.

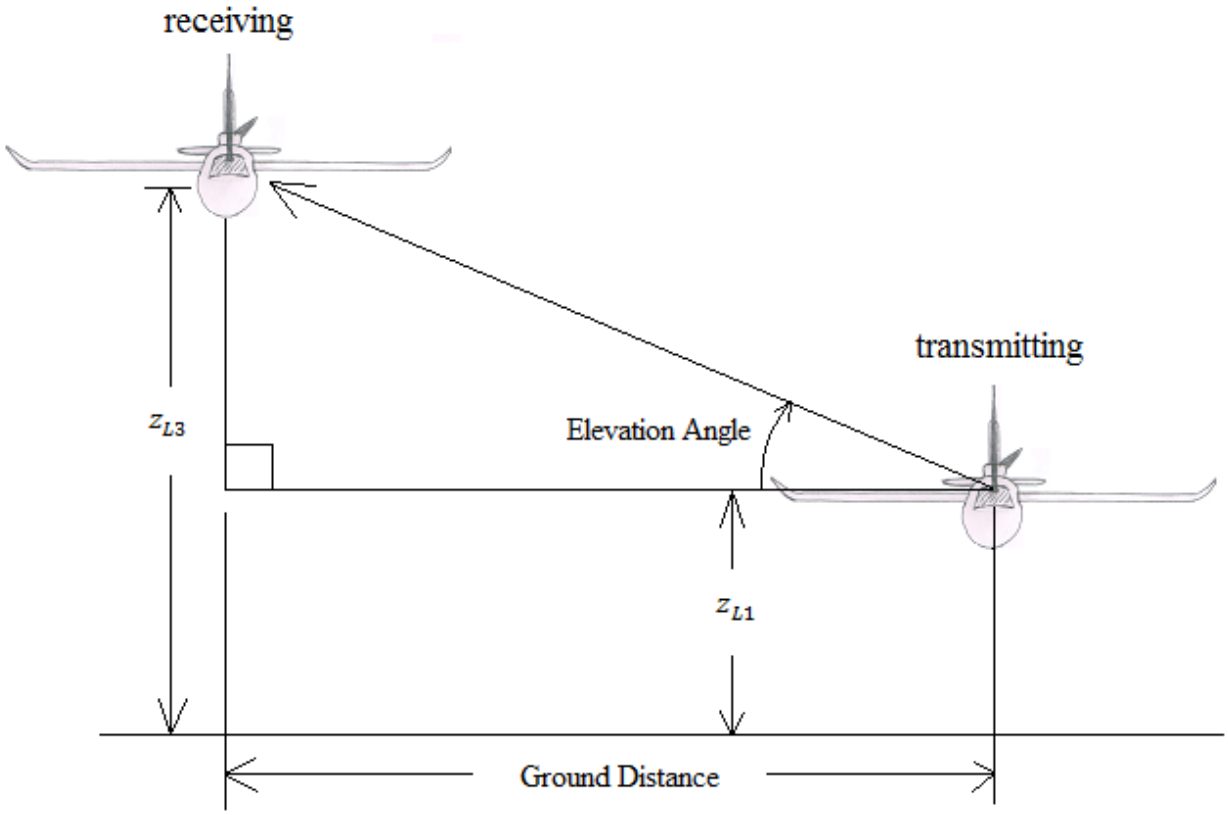

Figure 35: Elevation Angle Geometry.

The elevation angle is given by

$$\text{Elevation Angle } = \tan^{-1}\frac{z_{L3} - z_{L1}}{Ground\ distance} \tag{44}$$

Where z_{L1} and z_{L3} are defined in Section 3.3. Using the definition of the elevation angle, the bias and standard deviation of the error between the simulated and measured results were plotted in Figure 36. This plot shows that as the elevation angle moves from zero the Friis error begins to have a positive bias. Furthermore, it shows that the one-ray and two-ray experience a negative bias as the elevation angle moves from zero. This bias is due to inaccuracies in the antenna model. Figure 14 of Section 3.5 reveals that the lobes above and below the main horizontal lobes are smaller than the datasheet specifies, and this causes the negative bias seen in Figure 36.

Figure 36 shows how the error is related to the elevation angle, but it does not prove why the error bias of the Friis model increased as the distance between the antennas decreased. To prove this the elevation angle with respect to the distance between the antennas must be plotted. The elevation angle however has both positive and negative values. This leads to cancellation and predicts a mean elevation angle closer to zero. For sake of evaluation, if it is assumed that Figure 36 is symmetric across the vertical axis (which is not far from reality), then we need only look at the absolute value of the elevation angle. Figure 37 reveals that the mean of the absolute value of the elevation angle is increasing as distance decreases. This increase in elevation angle causes increasing, positive bias in the error of the Friis model and decreasing, negative bias in error for the one-ray and two-ray models. These results prove why the error bias of the Friis model increased as the distance between the antennas decreased and why the bias of the one-ray and two-ray models became more negative as the distance between the antennas decreased.

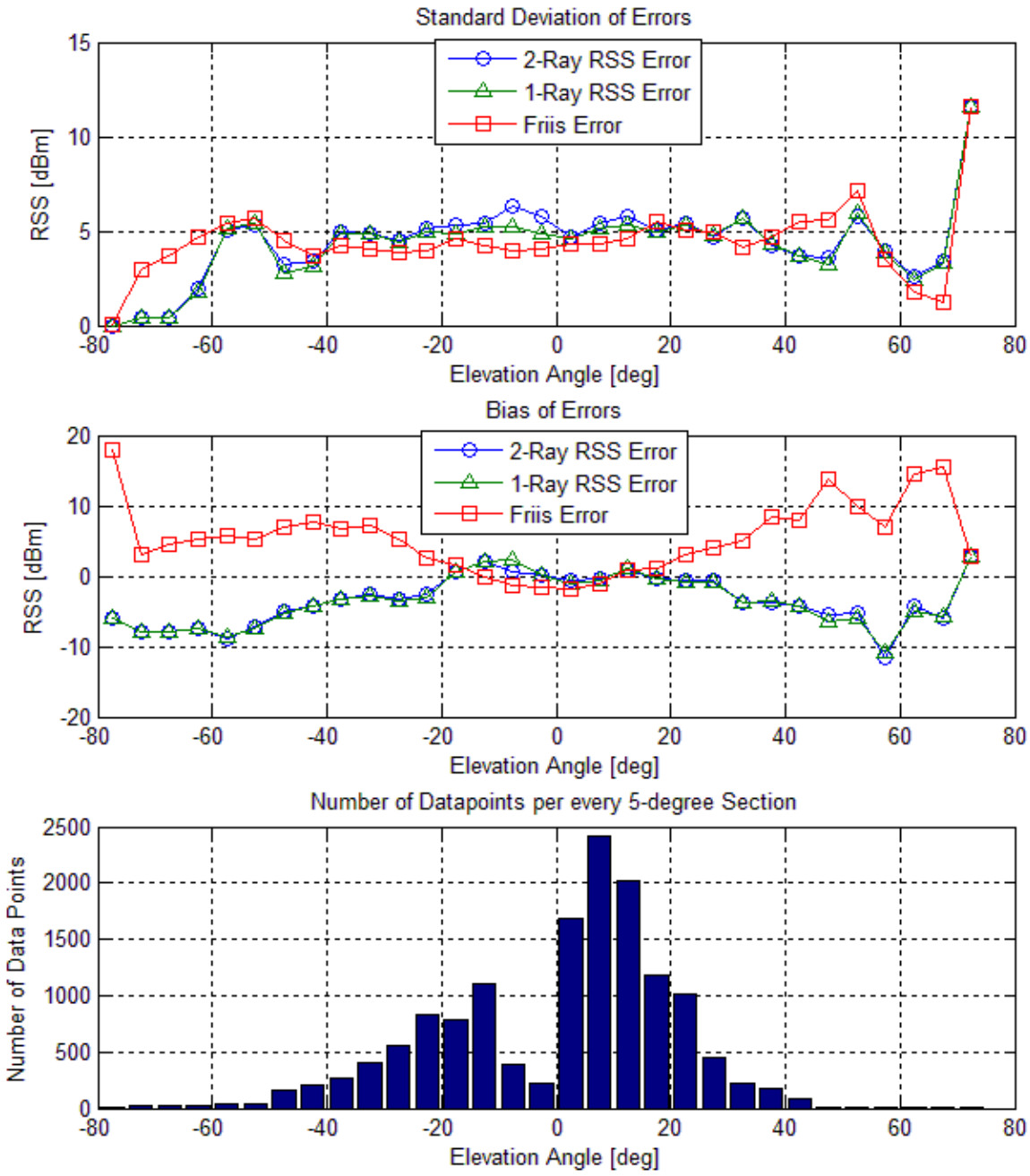

Figure 36: Error Statistics of All Scenarios with respect to Elevation Angle.

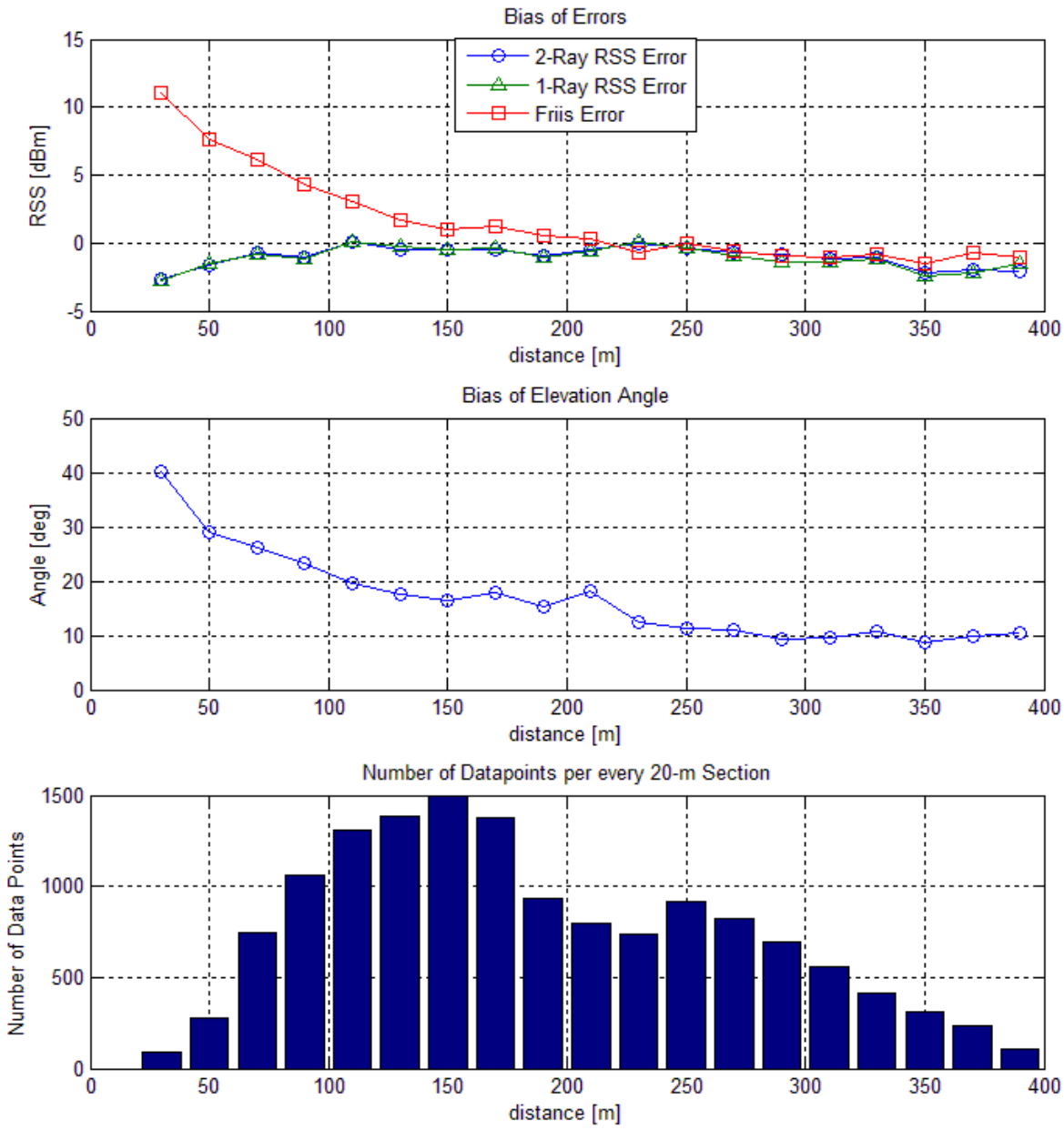

Figure 37: Bias of Errors and Mean Absolute Value of Elevation Angle vs. Distance

4.7. Summary

For the combination of all scenarios, the one-ray and two-ray models had a lower error bias than the Friis model for a majority of the antenna separation distances. This means that on average the one-ray and two-ray models produced the correct RSS value. On the other hand, the Friis model at short distances on average produced RSS values that were higher than the

measured values, which was linked to the Friis equation not taking into account the variations in antenna gain due to polarization and propagation direction. In addition, the negative error bias of the one-ray and two-ray models at short distances was linked to inaccuracies in the modelling of the antenna. The standard deviations of the errors for the one-ray and two-ray models were larger than that of the Friis model because of inaccuracies in the antenna model and the measurements of location and attitude. Lastly, the two-ray model performed almost identical to the one-ray model and showed no signs of improved accuracy or precision.

V Conclusions and Recommendations

5.1. Chapter Overview

This chapter concludes the research and presents recommendations for future research. Section 5.2 discusses the justification for this research. Section 5.3 discusses the goals of this research. Section 5.4 describes the contribution of this research to flight path planning, antenna selection, and protocol simulation. Section 5.5 provides a summary of the research findings. Section 5.6 describes the significance of this research, and Section 5.7 provides recommendations for future research.

5.2. Justification for Research

The reason for doing this research was to increase the fidelity of airborne wireless networking simulations. By doing so, the aircraft flight paths can be better optimized, and routing protocols can be tested in a simulation environment closer to reality. Static wireless network planning will also benefit from higher fidelity.

5.3. Research Goals

This research had three goals. The first goal was to develop a method and algorithm for modeling wireless communication in a simplified, rural, outdoor environment. This model used the position and attitude of each aircraft to predict the RSS. This model took into account polarization and multipath interference due to ground reflection. The second goal was to devise a system to acquire flight telemetry and RSS measurements. The system is discussed in detail in the appendices. The final goal was to validate the model by comparison with measured flight data.

5.4. Research Contribution

This research developed a model of the physical layer of an airborne communication system. This model was tested with real-world flight data collected using a system developed in this research. This model can be used in the optimization of flight paths to maintain the greatest signal strength. It can also be used in the selection and development of antennas for use in a specific airborne scenario. With modifications, it can simulate radio direction finding via phase shift analysis. Lastly, it provides a foundation for network simulation. This model can be extended to encompass the higher layers of the Open System Interconnection (OSI) model [11]. Employing this model in the physical layer provides for higher fidelity than that seen in many network simulators which do not incorporate computational electromagnetics (CEM) for antenna modeling.

5.5. Conclusions of Research

The two-ray model, on average, produced the correct result at all distances and was more accurate than the Friis model for the combination of all flight test scenarios. It was not however more accurate than the one-ray model. Inaccuracy in the antenna model caused the simulated results from the one-ray and two-ray models to be lower than the measured RSS at elevation angles above 20° and below -20°. Contrarily the results from the Friis model were higher than the measured RSS at elevation angles above 20° and below -20°. The standard deviation of the one-ray and two-ray models was also higher due to both inaccuracies in the model and errors in the measurement of the location and attitude. Figure 25 of Section 3.9 shows that small errors in the measurement of location can result in large variations of the predicted signal strength. Because the one-ray model is simpler and had the same accuracy as the two-ray model, it is the best model to use for the data collected in this research.

This research assumed the far-field approximation in the calculation of the electric field. For the far-field approximation, the electric and magnetic fields should not have components in the direction of propagation. However, Figure 38 shows that the electric field produced by the transmitting antenna has components in the direction of propagation at distances greater than the 1.30 m (Section 3.6). When the aircraft are/is in flight, the distance between the antennas is normally greater than 10 m for safety purposes, so this approximation works well for the line-of-sight ray. However, the reflection point can be close to the transmitting antenna during normal flight operations. When the reflection point is within the region where electric field has components in the direction of propagation, errors in the two-ray model are present because the reflection model does not take into account an electric field in the direction of propagation. These errors may be negligible; however, they are mentioned here for completeness.

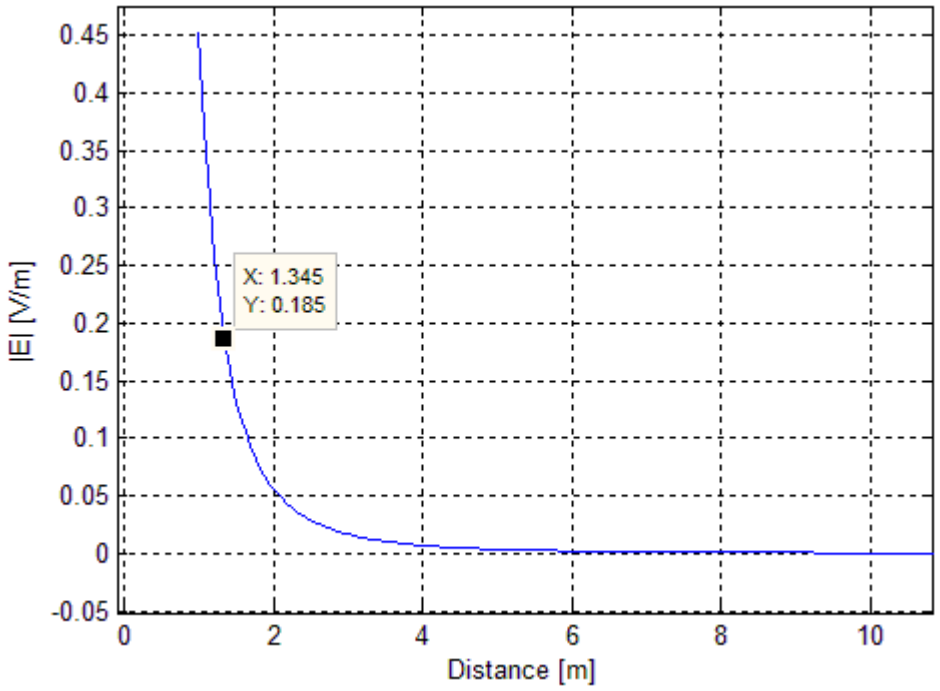

Figure 38: Amplitude of Electric Field in the Direction of Propagation vs. Distance.

5.6. Significance of Research

The method devised in this research is unique in that it combines a CEM antenna model and the two-ray model to calculate RSS values in a dynamic airborne environment. In addition, it serves as a foundation for future research in antenna modeling, airborne wireless network simulation, and flight path optimization using MATLAB®.

5.7. Recommendations for Future Research

Future researchers should first focus on increasing the accuracy of the antenna model. The antenna used in this research was complex to model, and the radiation pattern showed deviation from the datasheet's specifications. A simpler antenna may be easier to model and yield better results. For this reason, I would recommend using a simpler antenna. For those interested in making the model more accurate for the flight tests performed in this research. I suggest trying the thin wire model or the finite element method.

For the flight environment at Camp Atterbury's small UAV airstrip, the two-ray model did not outperform the one-ray model; however, further research is warranted in studying the two-ray model's performance over a paved runway. This research may prove that the two-ray model is better at characterizing signal propagation over a runway.

For the flight tests performed for this research, the separation distance did not exceed 400 m. Two-ray model may become more accurate when the horizontal separation distance is greater than 400 m. This is because the absolute values of the reflection coefficients from Section 3.6 approach 1 as the angle α goes to zero regardless of the polarization or electromagnetic properties of the soil [39]. Further research is warranted to validate the accuracy of the two-ray model for greater horizontal separation distances. The original plan was to have the aircraft fly out to a horizontal separation distance of over one mile. However, feedback from amplifier used

to boost the RF signal of the WLAN modules caused the modules to fail (Appendix A). The modules functioned for several hours before failing and may have failed due to thermal issues.

This research used WLAN modules in order to make RSS measurements. In order to gain a better understanding of the physical layer, a software defined radio should be used. A software defined radio opens the possibility of testing different modulation schemes and operating at a variety of frequencies. In addition, software defined radios could be used to perform RF source localization and navigation via signals of opportunity. Future researches should study how to implement these radios on a small unmanned aerial vehicle.

In February of 2014, Steve Perlman announced the development of technology called pCell [55]. This technology relies on deliberate interference of electromagnetic signals, which is in opposition to previous communication technology. Each pCell radio transmits part of the signal to be picked up by the receiver. Through precise timing, the signals combine at one point in space to provide the full signal. This system has been lab tested and has shown drastic improvement in bandwidth over legacy systems. If this system can be employed airborne environment, it could provide a means for a more efficient and reliable communications. Future researchers should look into the implementation of this technology into future communication systems.

Appendix A. Hardware Configuration

The data collection portion of this research was performed using two aircraft. The first aircraft contained a WLAN module which was configured as an access point, while the second aircraft contained a WLAN module which was configured as a client. The second aircraft was used to take measurements of the received signal strength (RSS). Though the ArduPilot Mega (APM) was used by both aircraft, it was not used to control the aircraft which avoided the possibility of crash due to microcontroller malfunction. Section A.1 discusses the aircraft used in the experiment and includes recommendations for future configurations. Section A.2 presents the hardware configuration of the aircraft containing the network client. Section A.3 describes the hardware configuration for the aircraft containing the access point, which acts as the airborne 802.11 wireless relay. Section A.4 discusses recommendations for future hardware configuration that makes use of the APM's autopilot feature.

A.1. Aircraft

The aircraft used in this experiment was the Super Sky Surfer sold by Banana Hobby. The Super Sky Surfer is an RC sailplane with a large wingspan (2400 mm) and wing cord length (315 mm), which facilitates slow flight and high lifting capacity. Several modification were made to the airframe in order to carry a larger than standard payload and facilitate easy setup and teardown.

The standard configuration of the Super Sky Surfer uses two servos mounted within the fuselage to actuate the elevator and rudder. Both servos were moved near the tail which allows more weight to be place in the fuselage without causing the aircraft to become nose heavy (Figure 39 and Figure 40). In addition, the pushrod assembly was replaced with stronger materials: thicker pushrods and studier clevises.

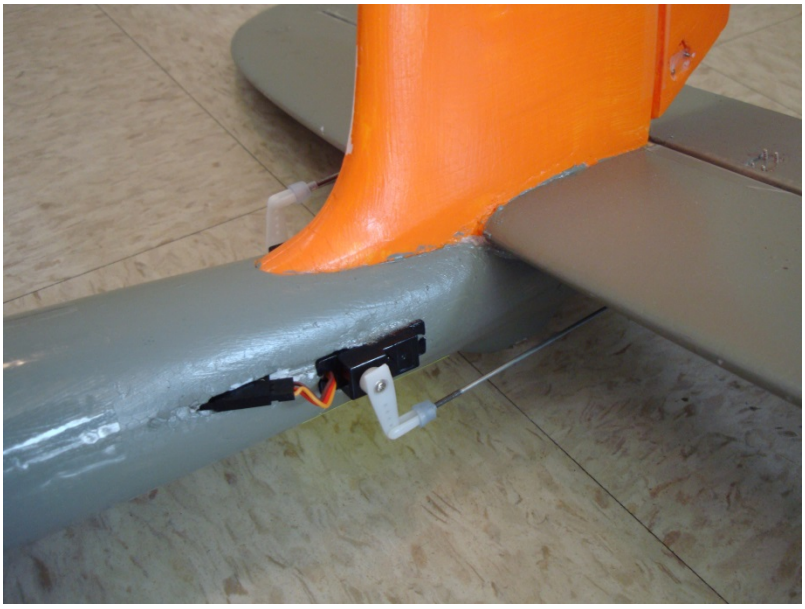

Figure 39: Elevator Servo.

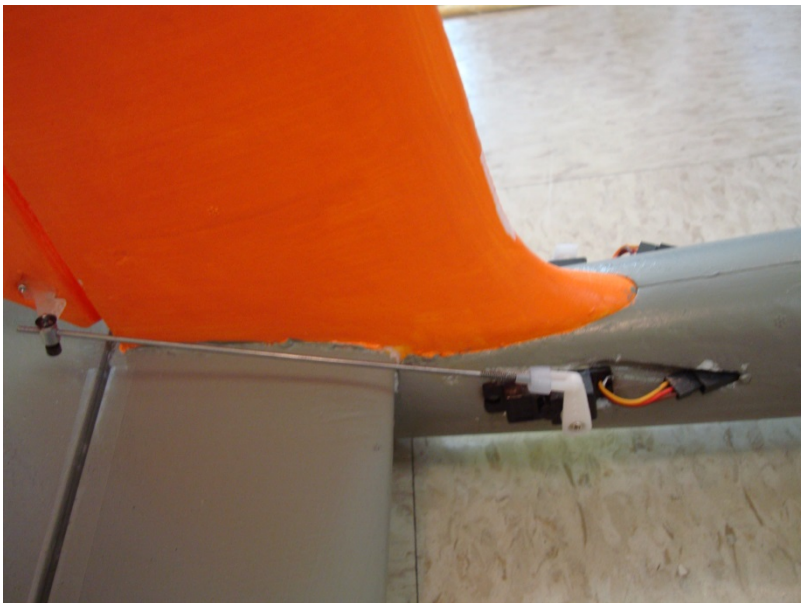

Figure 40: Rudder Servo.

To produce greater power from the motor, the stock speed controller was replaced with a Turnigy® Plush 60A Bulletproof ESC/BEC. In the addition, the battery was upgraded from a three cell to a four-cell, 4500-mAh, 35-70C, Turnigy battery, and the propeller was replaced with an 8x6 pusher propeller.

In order to allow the wings of the aircraft to be easily removed for storage, the servo connections were moved to under the wing (Figure 41). This configuration also made assembly easier. Both aircraft used Spektrum® DSMX receivers with remote receivers (Figure 42).

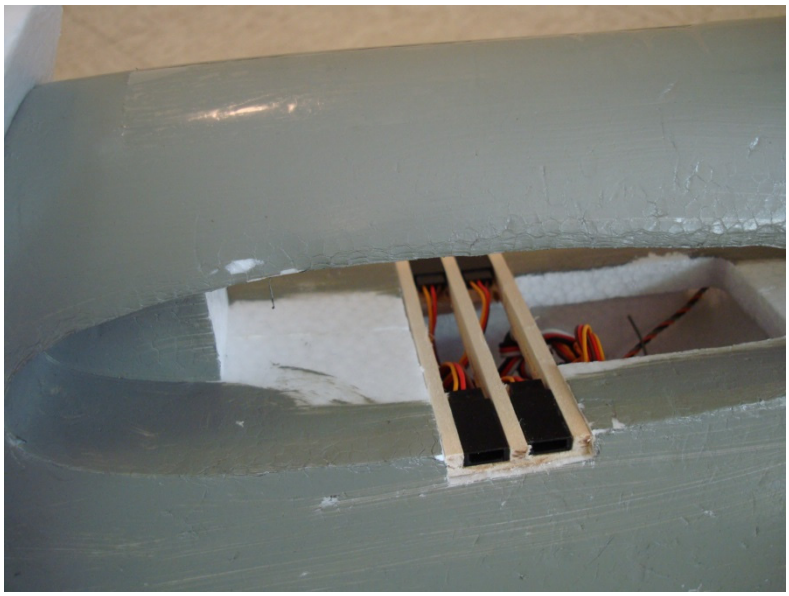

Figure 41: Servo connections for wings.

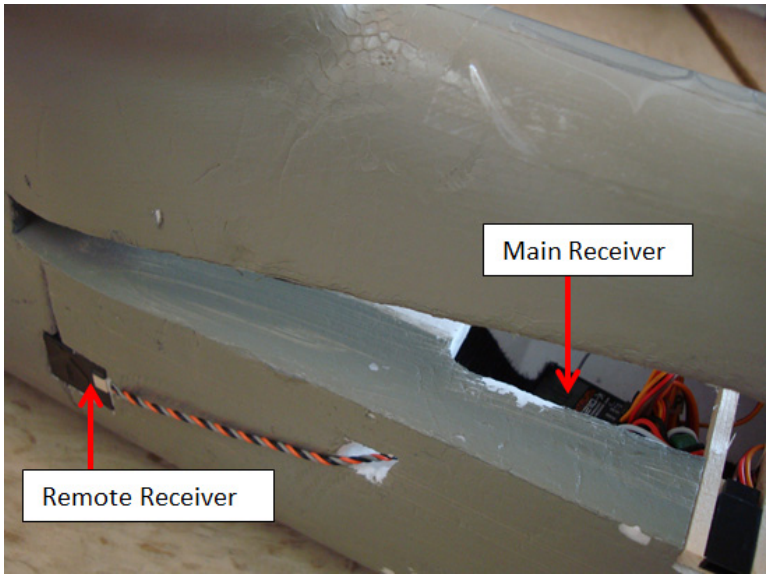

Figure 42: Spektrum receiver with externally mounted remote receiver.

Flight testing with the Super Sky Surfer revealed several weaknesses with the aircraft due to poor manufacturing and low quality standards. The stock motor is well designed; however, the

magnets within the motor detached from the rotor during flight. This is caused by poor adhesion of the magnets to the rotor. This problem is fixed by placing the rotor on a drill or similar device, applying super glue to the magnets, and spinning the rotor to allow the centripetal force to pull the glue into the cracks surrounding the magnets.

The stock servos which are included in the almost-ready-to-fly kit are of low quality, and the failure of an aileron servo during flight caused one of the aircraft used in this research to crash. Furthermore, the glue along the center seam of the fuselage has proven unreliable, causing the fuselage after several flights to start splitting down the seam. In order to alleviate these problems, the Super Sky Surfer should be purchased in kit form without servos, and fuselage seam should be reinforced with tape and glue.

A.2. Client Aircraft Payload Configuration

The payload carried by the client aircraft consisted of:

- 1-W bidirectional 2.4-GHz amplifier
- 6-V voltage regulator for amplifier
- Roving Networks® RN-171-XV 802.11 b/g WLAN module [56]
- XtreamBee XBee® adapter board [57]
- 3DR™ 915-MHz telemetry transceiver
- 2.4-GHz antenna [47]
- 3DR™ uBlox™ GPS/magnetometer module
- APM power module
- APM 2.6 microcontroller

The 1-W bidirectional 2.4-GHz amplifier was used in the initial configuration of the aircraft to amplify the signal to and from the WLAN module; however, after several flights were performed, the amplifier caused the module to burn out. The engineers at Roving Networks stated that the antenna circuit of the module does not support an amplifier. For the remainder of the flight tests, the amplifier remained in the aircraft only to provide weight for balancing, and the voltage regulator was removed.

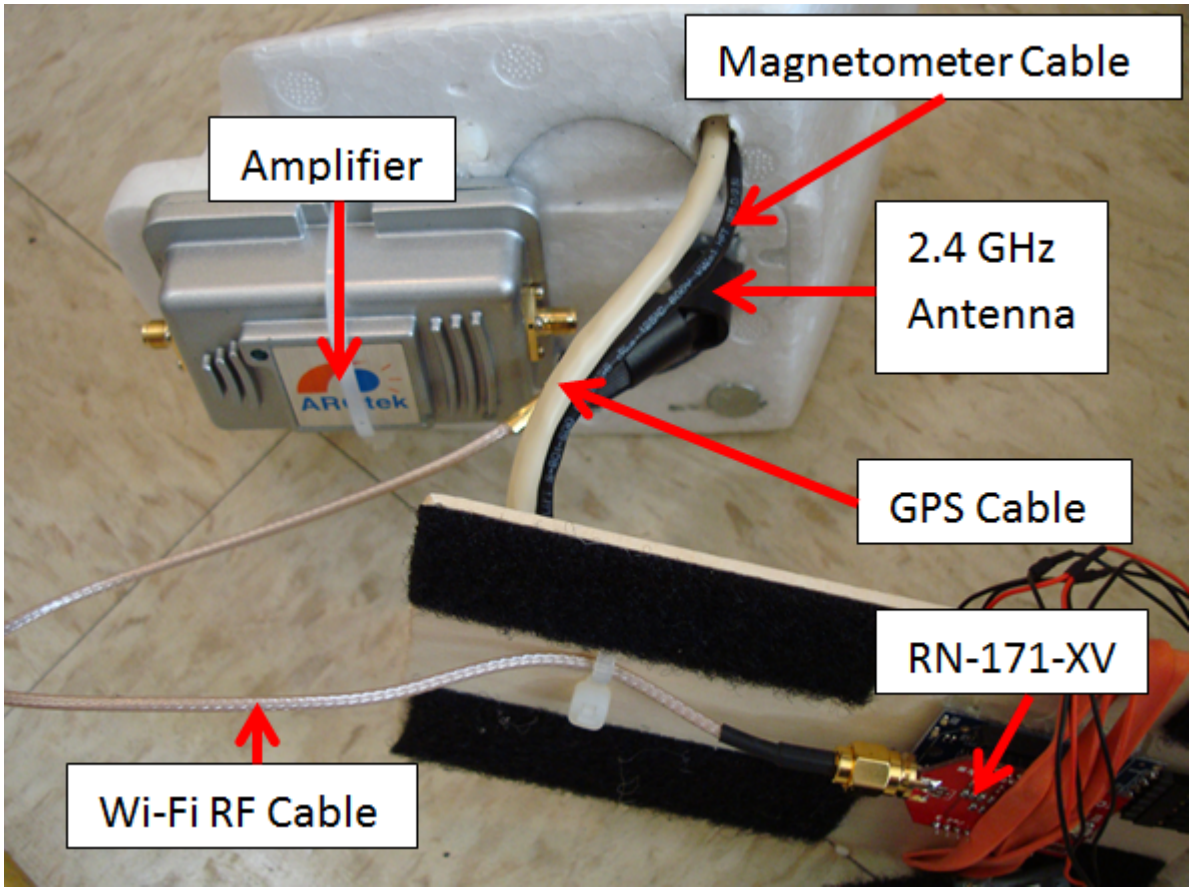

Figure 43: RN-171-XV connected directly to antenna.

The RN-171 is the red module shown in Figure 43. It is attached the XtreamBee Xbee adapter board, and the adapter boards selection switch is set to master. The telemetry receiver enabled a real-time display of aircraft positioning information and RSS on a ground station (Figure 44). The diagram show in Figure 45 outlines the relationship among payload

components. The GPS/magnetometer module was enclosed by the canopy (Figure 46 and Figure 47), which also provided support for the antenna.

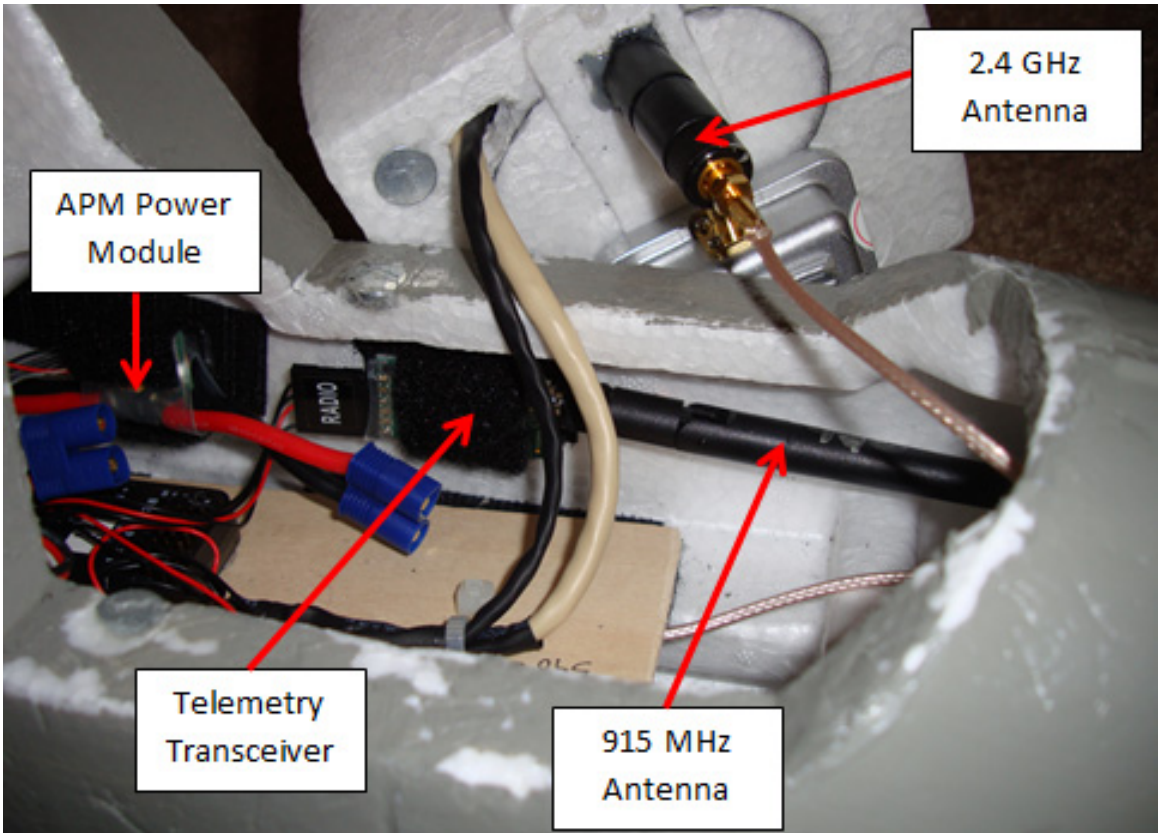

Figure 44: Image of payload bay.

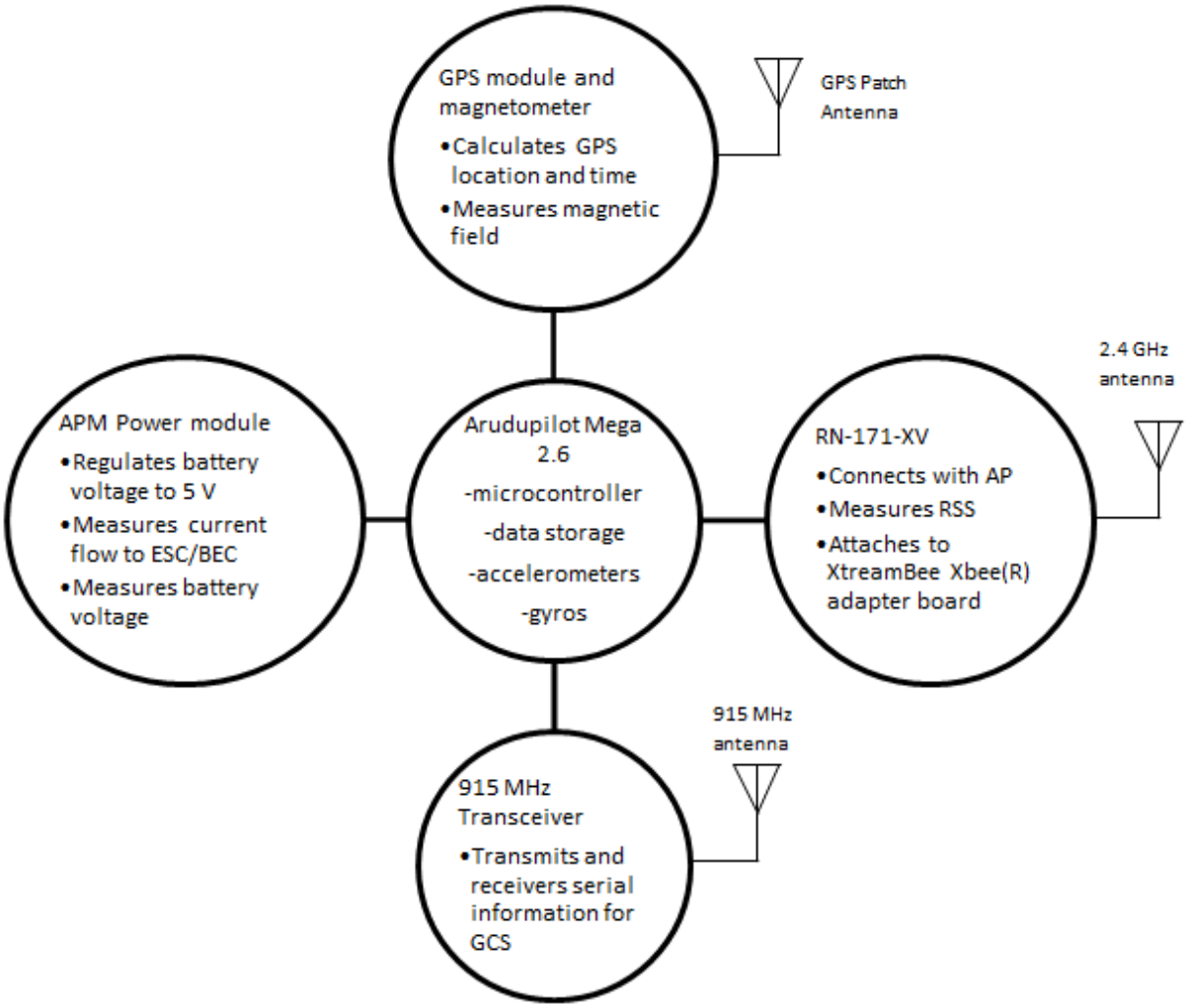

Figure 45: Diagram of payload components for the client aircraft.

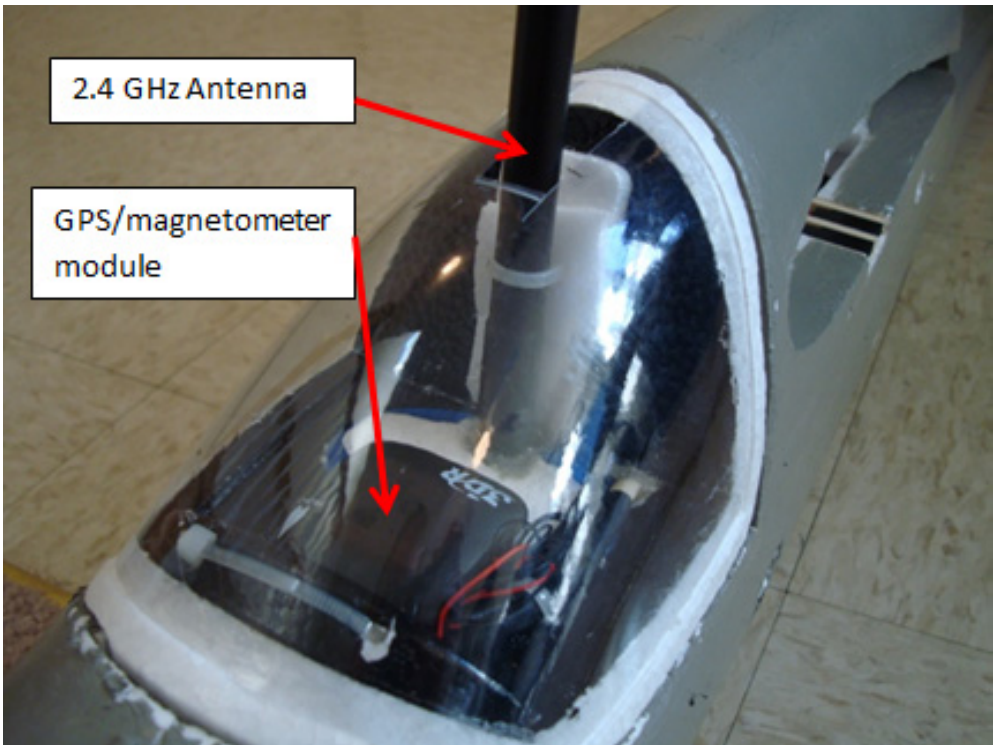

Figure 46: GPS/magnetometer module and antenna.

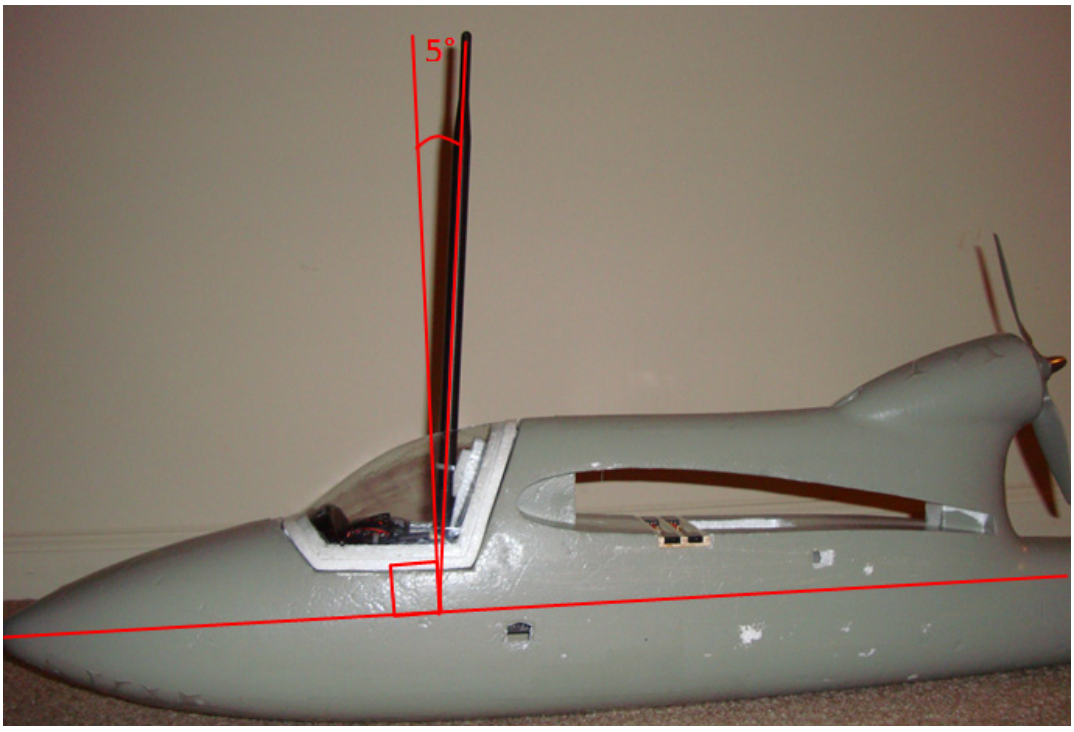

Figure 47: Side view displaying antenna placement.

The APM power module supplies five volts to the microcontroller, which subsequently provided five volts to the GPS module, telemetry transceiver, and WLAN module. The microcontroller was modified from its standard configuration to allow access to two Universal Asynchronous Receiver/Transmitter (UART) ports. UART0 port is shared by the USB™ port and telemetry port. When the USB port is connected with a computer, the telemetry port is disabled by an onboard multiplexer. UART2 port is accessible at the through-hole JP13 location (Figure 48), and the pins adjacent to JP13 provide five volts and ground. UART2 was used to communicate with the WLAN module (Figure 49).

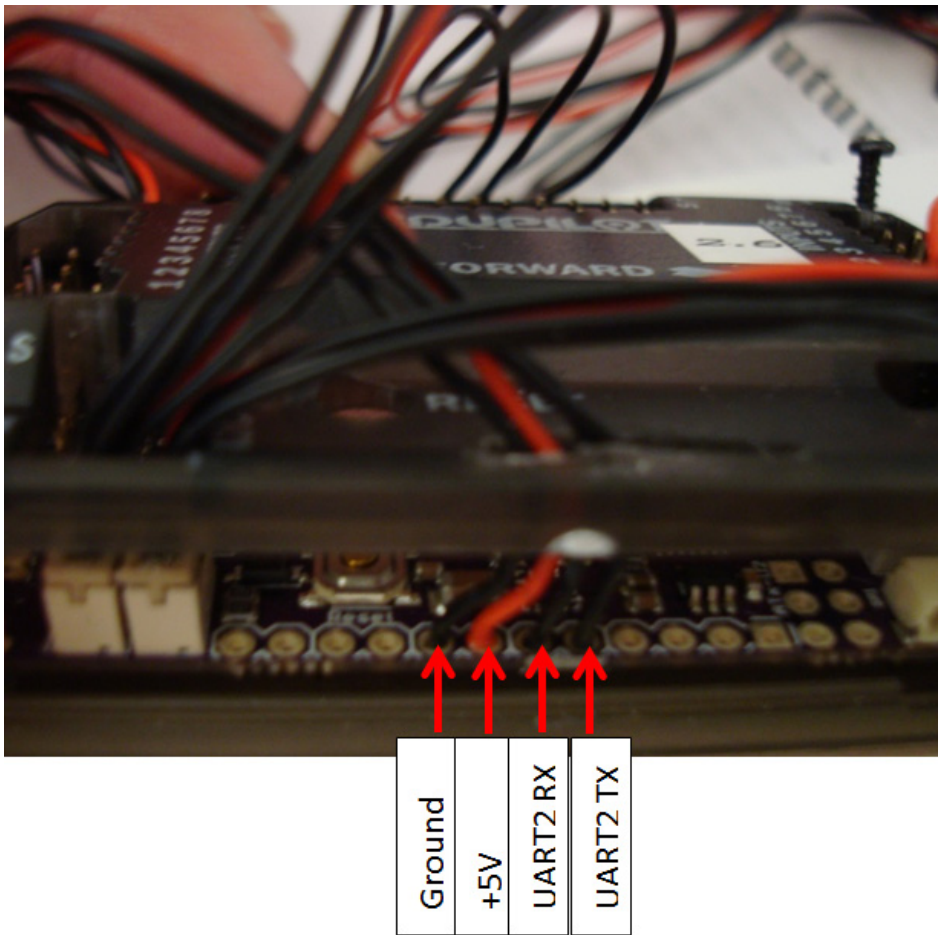

Figure 48: UART2 connection.

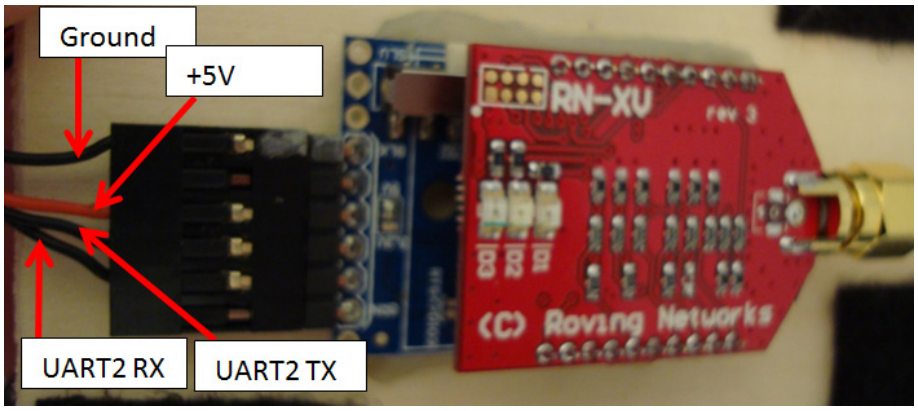

Figure 49: WLAN module connection.

A.3. Access Point Aircraft Payload Configuration

The payload carried by the access point aircraft consisted of:

- 1-W bidirectional 2.4-GHz amplifier
- Roving Networks® RN-171-XV 802.11 b/g WLAN module [56]
- XtreamBee XBee® adapter board [57]
- 2.4-GHz antenna [47]
- 3DR™ uBlox™ GPS module
- APM power module
- APM 2.5 microcontroller

The access point aircraft was similar to the client aircraft with following differences. UART2 port and telemetry transceiver were not used, and the microcontroller did not communicate with the WLAN module. The standard telemetry cable and port were used with serial data lines removed and provided only power to the WLAN module. The reason that the WLAN module is not communicated with by the microcontroller is because the module cannot report signal strength information when configured as an access point. Lastly, the APM 2.5

contains the magnetometer onboard, while the GPS module is external. Figure 50outlines the relationship among payload components.

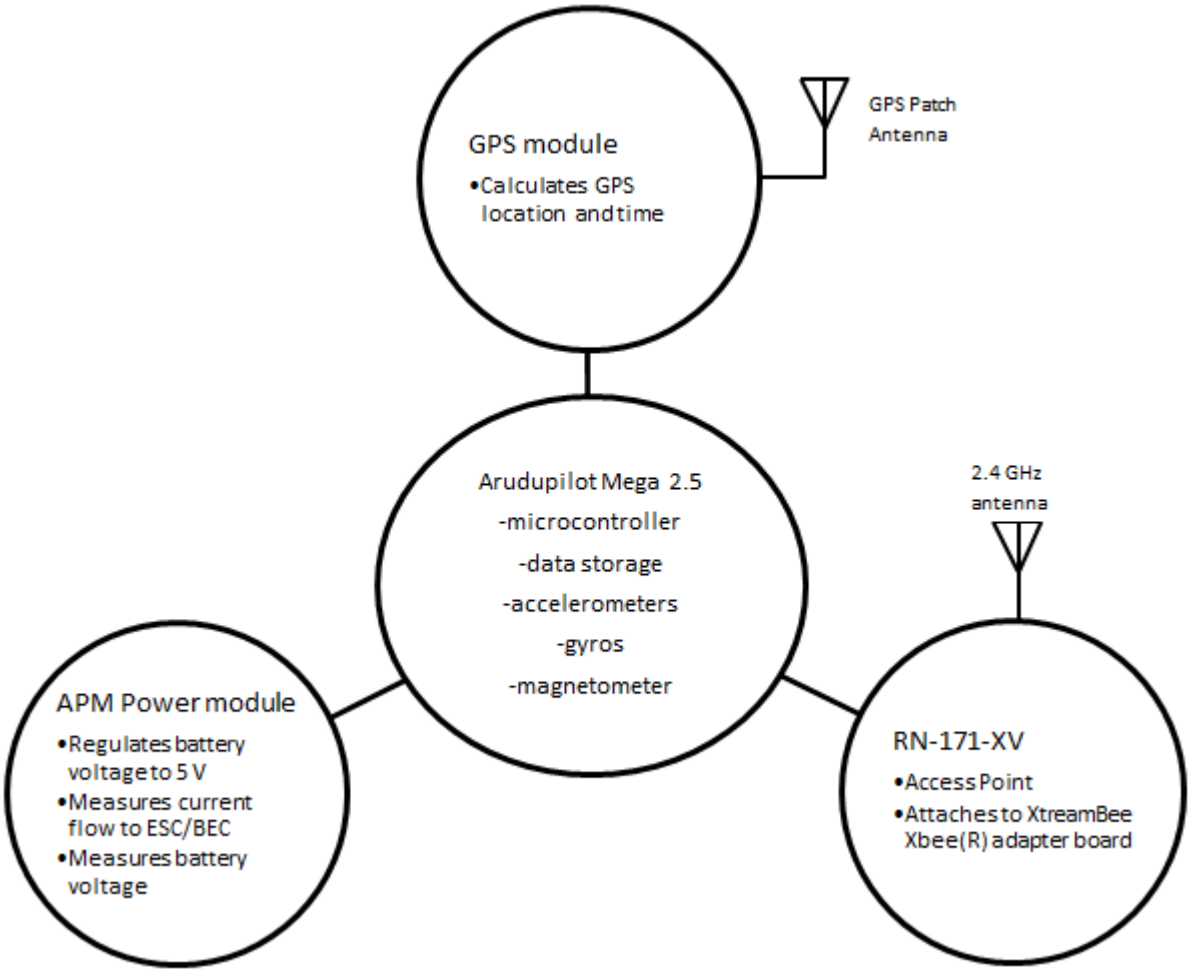

Figure 50: Diagram of payload for access point aircraft.

A.4. Using APM autopilot feature

The APM is capable of flying the aircraft in addition to measuring signal strength data. However, using the code written for this research, problems with the WLAN module will cause the APM's main processor to run a continuous loop in which the processor is looking for data from the WLAN module. Since this loop does not contain the navigation or control functions, the APM will not update flight control surfaces and may cause the plane to crash. The APM 2.5 and 2.6 do not contain a failsafe multiplexer. Consequently, if the processor runs into an infinite loop

or is programmed incorrectly, the APM may not be able to switch back to manual mode in case of an emergency. If future research involves using the APM to control the aircraft while running customized code, an external hardware multiplexer should be used to eliminate the possibility of aircraft loss due to programming errors. Figure 51 displays the implementation of a failsafe mux sold by 3DRobotics™.

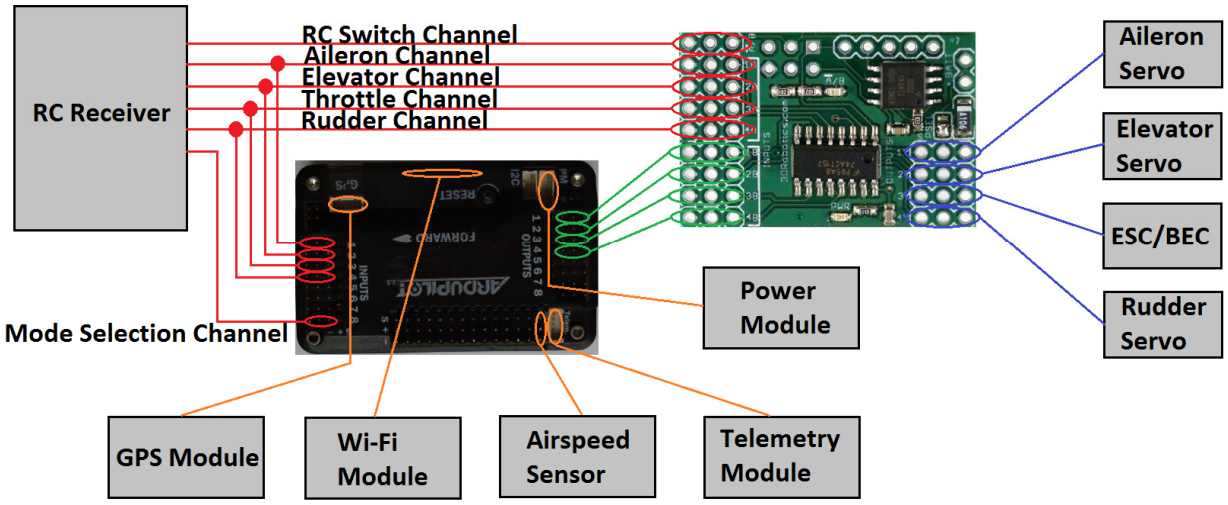

Figure 51: Failsafe mux implementation.

Appendix B. Software Configuration

In order to collect the data necessary for this research, the ArduPlane V2.75beta2 source code [58] was modified, and the WLAN modules were manually configured. Section B.1 discusses the modifications made to the original ArduPlane source code in order to collect the received signal strength (RSS). Section B.2 describes the setup process for the WLAN modules, and Section B.3 illustrates how troubleshooting was performed.

B.1. ArduPlane source code modifications

The ArduPlane source code configures the ArduPilot as an autopilot for fixed-wing aircraft. Modifications were made to the ArduPlane source code installed on the aircraft to include a client WLAN module. Minor modifications were made to the ArduPlane code so as to not disrupt the original ArduPlane routines. The WLAN module was originally connected to the standard telemetry port. To collect WLAN data, the flow of telemetry data through this port must be stopped. However, stopping telemetry data flow also stops data flow through the USB. Consequently, the Mission Planner ground control software [58] is unable to communicate with board. For this reason, the original configuration was abandoned, and the WLAN module was connected to the UART2 port, which is the only other available port on the board. This configuration allowed communications through the standard telemetry port and USB to remain functional.

The Arduino programming language requires a void setup function and void loop function. The setup function initializes the board in preparation for the loop function. The setup function runs whenever power is connected to the ArduPilot, the reset button is pressed, or USB port is connected or disconnected from a computer. Within this function, a command is sent to the WLAN module requesting a reboot. This ensures that the module will be in the same state

every time the setup function runs. Following the reboot command is a command to place the module in command mode, which is necessary to acquire RSS. Algorithm 1 is a section of *WifiTestConfiguration.ino*, and the additions to this file are highlighted in red.

Algorithm 1: Additional Code added to setup function (WifiTestConfiguration.ino).

```
void setup() {
    // this needs to be the first call, as it fills memory with
    // sentinel values
    memcheck_init();
    cliSerial = hal.console;
    // load the default values of variables listed in var_info[]
    AP_Param::setup_sketch_defaults();
    // arduplane does not use arming nor pre-arm checks
    notify.init();
    AP_Notify::flags.armed = true;
    AP_Notify::flags.pre_arm_check = true;
    rssi_analog_source = hal.analogin->channel(ANALOG_INPUT_NONE);
    vcc_pin = hal.analogin->channel(ANALOG_INPUT_BOARD_VCC);

    batt_volt_pin = hal.analogin->channel(g.battery_volt_pin);
    batt_curr_pin = hal.analogin->channel(g.battery_curr_pin);

    init_ardupilot();

    // initialise the main loop scheduler
    scheduler.init(&scheduler_tasks[0],
    sizeof(scheduler_tasks)/sizeof(scheduler_tasks[0]));

    hal.uartC->println_P(PSTR("reboot"));//Reboot WLAN adapter
    delay(500);
    hal.uartC->print_P(PSTR("$$$")); //Place WLAN adapter in command mode
    delay(500);
}
```

The void loop function is the main program which runs continuously after initialization has been performed. This loop contains a scheduler which allots time for the multiple tasks and ensures that control updates are made at 50 Hz. Within this schedule is a logging task which stores telemetry data to the onboard memory. *Log.pde* comprises the code used for logging (see Figure 2). In Algorithm 2, modifications are highlighted in red. The character string *mystring* was declared in the beginning of *WifiTestConfiguration.ino*. Since the RSS data must be logged with the corresponding attitude data to meet data collection requirement, the commands to

acquire data from the WLAN module were placed within the function which logs the attitude data to the memory. In this code, the show r command is routinely sent to the WLAN module, and the module sends back a text string. This string is then parsed to pull out the RSS. The RSS is then stored as an integer, and this value is logged with the rest of the data in the attitude packet.

Algorithm 2: Code which requests and stores RSS data (Log.pde)

```
// Write an attitude packet. Total length : X bytes
// Modified by Matthew Vincie
static void Log_Write_Attitude(void)
{
    uint16_t stored_rssi;
    while(!hal.uartC->available()){}//Wait for input from modem
    hal.uartC->flush();  //Flush buffer for UART2
    hal.uartC->println_P(PSTR("show r"));//Request RSS from modem
    for(int i=0;i<14;i++){
        while(!hal.uartC->available()){}
        mystring[i]=hal.uartC->read();}//Places modem reply in mystring
    stored_rssi=((mystring[7]-'0')*10+(mystring[8]-'0'));//Pulls the RSS
    // value from the string and stores the value as an integer
    receiver_rssi=stored_rssi*255/100; //This scaled value is sent to the GCS


    struct log_Attitude pkt = {
        LOG_PACKET_HEADER_INIT(LOG_ATTITUDE_MSG),
        roll  : (int16_t)ahrs.roll_sensor,
        pitch : (int16_t)ahrs.pitch_sensor,
        yaw   : (uint16_t)ahrs.yaw_sensor,
        rssi  : stored_rssi  //RSS value added to the data being stored to
       //the APM memory
    };
    DataFlash.WriteBlock(&pkt, sizeof(pkt));
}
```

The original ArduPlane source code is designed to measure RC receiver RSS and send these values to the ground control station (GCS). Some RC receivers will output a voltage that is proportional to the RSS. The ArduPilot uses an analog-to-digital converter on pins A0, A1, or A13 to measure the voltage coming from RC receiver. The measured voltage is stored in the *receiver_rssi* variable which is continuously updated with each measurement and then sent within the telemetry stream to the GCS. The parameter list provides the ability to select the pin

used in the RSS measurement and to disable the RSS measurement altogether. When the RSS measurement is disabled, the *receiver_rssi* variable will not update from zero; however, this value is still sent to the GCS. The modified code updates the *receiver_rssi* variable with a scaled value of the WLAN module's RSS. This allows real-time display of the RSS to the GCS.

Lastly, the log structure for attitude was modified to contain the RSS variable. This was done by adding an additional "c" before the final "C" within the log attitude structure (Algorithm 3).

Algorithm 3: Modification to attitude log structure (Log.pde).

```
static const struct LogStructure log_structure[] PROGMEM = {
    LOG_COMMON_STRUCTURES,
    { LOG_ATTITUDE_MSG, sizeof(log_Attitude),
      "ATT", "cccC",        "Roll,Pitch,Yaw,RSSI" },//An additional c was
      //added
    //before the final C to allow a slot for RSSI to be stored
    { LOG_PERFORMANCE_MSG, sizeof(log_Performance),
      "PM",  "IHhBBBhhhhB",
"LTime,MLC,gDt,RNCnt,RNBl,GPScnt,GDx,GDy,GDz,I2CErr" },
    { LOG_CMD_MSG, sizeof(log_Cmd),
      "CMD", "BBBBBeLL",   "CTot,CNum,CId,COpt,Prm1,Alt,Lat,Lng" },
    { LOG_CAMERA_MSG, sizeof(log_Camera),
      "CAM", "ILLeccC",   "GPSTime,Lat,Lng,Alt,Roll,Pitch,Yaw" },
    { LOG_STARTUP_MSG, sizeof(log_Startup),
      "STRT", "BB",         "SType,CTot" },
    { LOG_CTUN_MSG, sizeof(log_Control_Tuning),
      "CTUN", "cccchhf",    "NavRoll,Roll,NavPitch,Pitch,ThrOut,RdrOut,AccY"
},
    { LOG_NTUN_MSG, sizeof(log_Nav_Tuning),
      "NTUN", "CICCcc",     "Yaw,WpDist,TargBrg,NavBrg,AltErr,Arspd" },
    { LOG_MODE_MSG, sizeof(log_Mode),
      "MODE", "MB",         "Mode,ModeNum" },
    { LOG_CURRENT_MSG, sizeof(log_Current),
      "CURR", "hhhHf",      "Thr,Volt,Curr,Vcc,CurrTot" },
    { LOG_COMPASS_MSG, sizeof(log_Compass),
      "MAG", "hhhhhhhhh",   "MagX,MagY,MagZ,OfsX,OfsY,OfsZ,MOfsX,MOfsY,MOfsZ"
},
    TECS_LOG_FORMAT(LOG_TECS_MSG),
};
```

B.2. WLAN module setup process

Setting up the WLAN modules is a two-step process. The firmware on each module was first updated to wifly-EZX version 4.00.1. The updated firmware allows the module to function as an access point and includes bug fixes. The second step is to configure the individual modules to perform in the WLAN network. Section B.2.1 describes the method used to update the firmware, and Section B.2.2 outlines the process of configuring the individual modules. For additional information, visit the Microchip website.

B.2.1. WLAN module firmware update

Before the firmware on the module can be updated, the module must be able to communicate with a computer. Communication can be achieved in three ways: using an XtreamBee Xbee adapter board with a FTDI cable, Ad-hoc wireless connection, or RN-XV-EK1 USB serial converter with USB cable. The XtreamBee Xbee method requires moving the solder jumper on the board to allow for a 3.3 V input. Of these methods, the serial converter method provides the easiest setup. This method was used in this research.

Once the module is connected to the computer either by USB or FTDI, communication with the module is done through a terminal emulator which is able to communicate through a serial port. For this research, Tera Term version 4.78 was used, which has features similar to PuTTY and SecureCRT. Tera Term is open source software and can be downloaded from the TeraTerm Project website.

When starting the Tera Term, the serial port associated with the WLAN module must be selected (Figure 52).

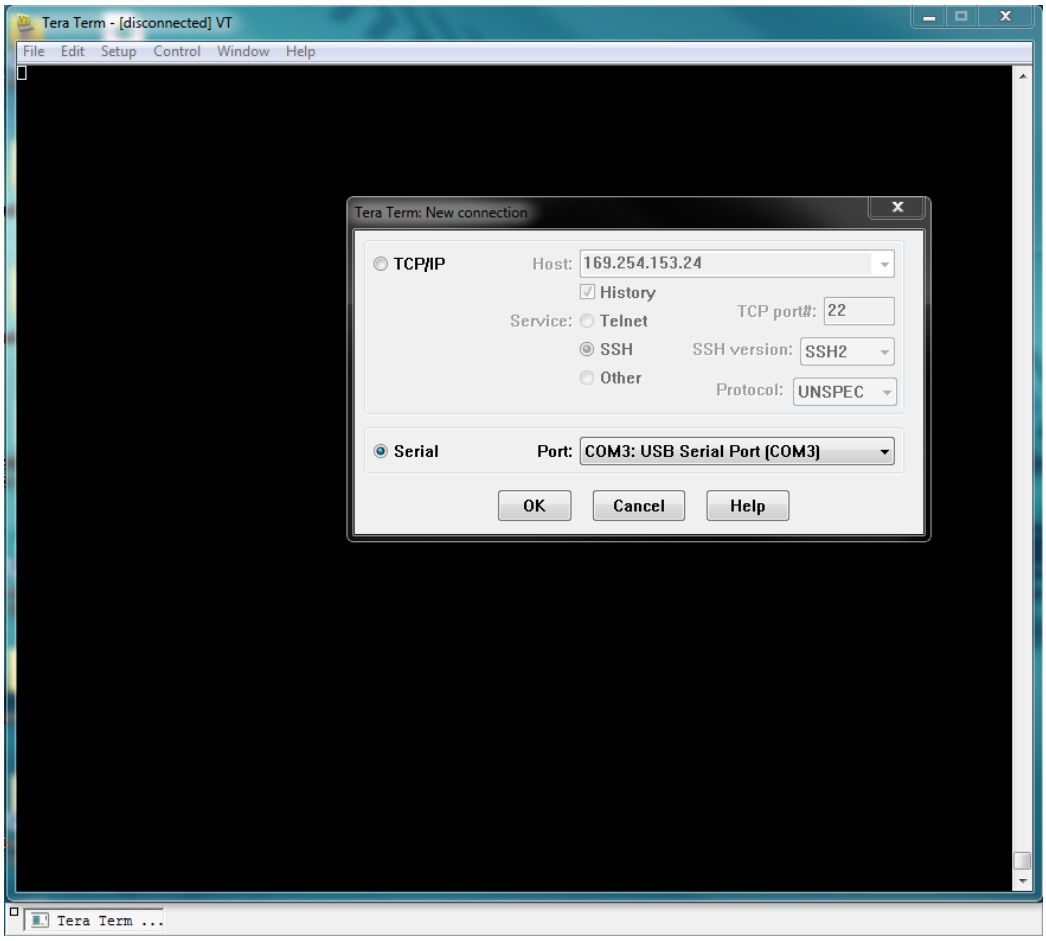

Figure 52: Serial port selection in Tera Term.

After clicking OK, press the reset button on the RN-XV-EK1 board. You should see information similar to that shown in Figure 53.

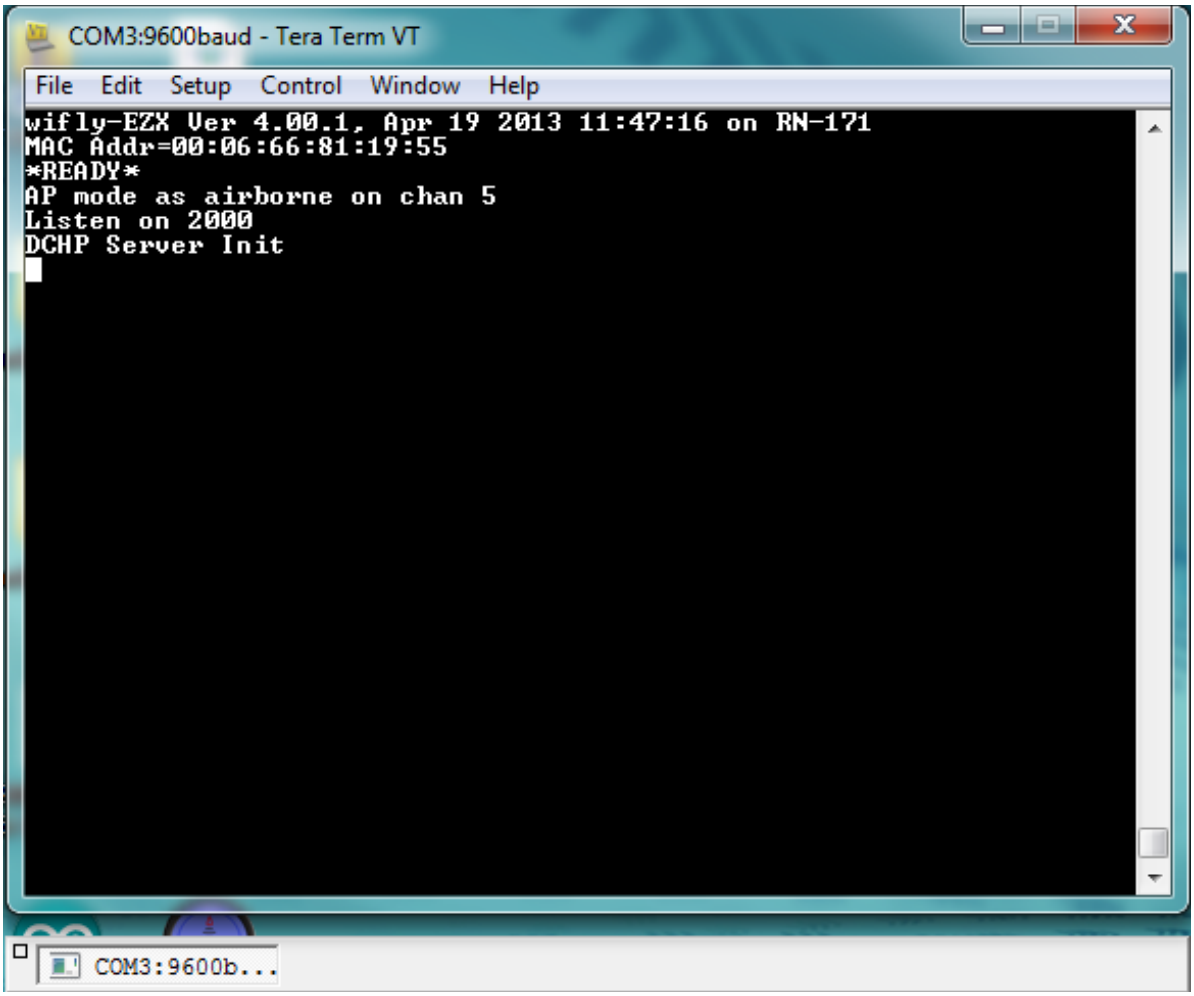

Figure 53: Message seen on startup.

If an illegible message is returned, the baud rate for the port is probably wrong. Configure the baud rate of the port by clicking **Setup** in the toolbar then **Serial port…** (Figure 54). The module is usually set to a baud rate of 9600 from the factory; however, to communicate with the ArduPilot, the baud rate of the module was set to 57600.

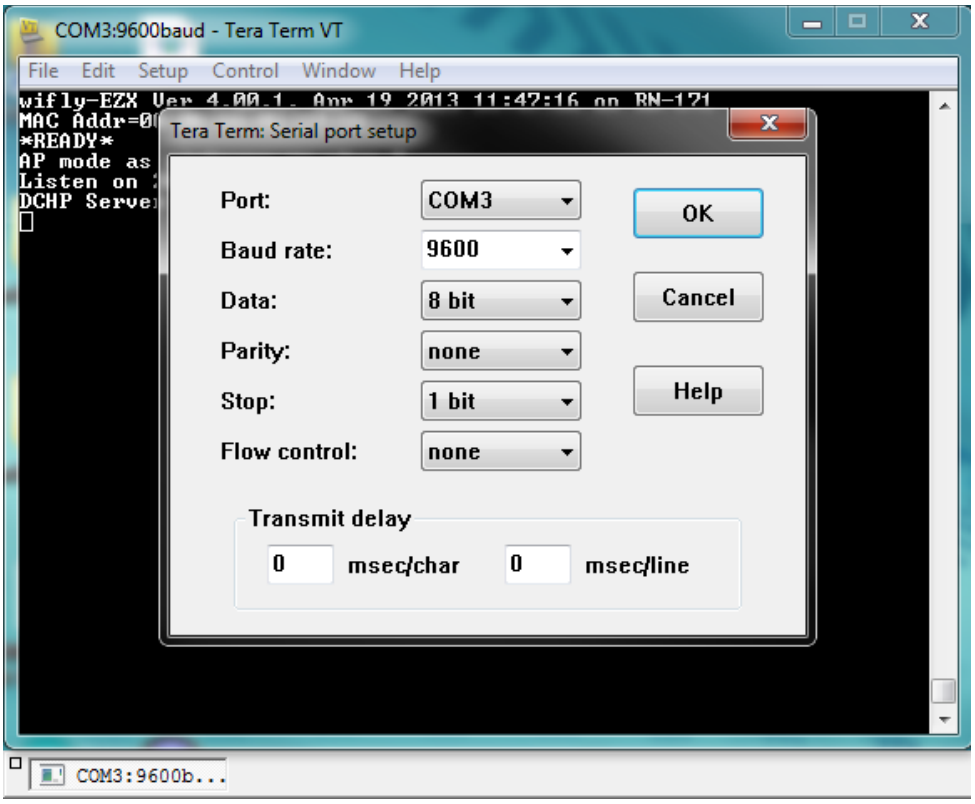

Figure 54: Setting baud rate for serial port.

After a legible message has been received from the module, the firmware update process can begin.

The next step is to place the module in command mode by typing **$$$** in the terminal window together quickly without additional characters directly before or after. The module will then return **CMD**. Type **factory R** to reset the module to factory specifications. Then type **scan** to see which wireless access points are available. If the wireless access point has a password, type **set w p password**, where **password** is the password for the wireless access point. Next type **join SSID**, where **SSID** is the SSID of the access point you are trying to join. This access point must have internet access for firmware update, and the SSID must not have any spaces between characters. Type **ftp update** to download and update the firmware. After the update, type **reboot**,

and place the module in command mode again. Type **factory R,** then type **save**, and lastly type **reboot**. The module is now ready for manual configuration.

B.2.2. WLAN module configuration

To configure the module which functions as the access point in the network, start by placing the module in command mode. Type **set wlan join 7** or **set w j 7** (short notation), to enable AP mode. Next type **set w c 5** to specify wireless communication on 802.11 channel 5. Type **set w s airborne** (airborne is the access point SSID). Then type **set i d 4** which enables the DHCP server. Next type **set w r 0** which reduces the wireless data rate to 1 Mbits/s which is the slowest rate available and maximizes the transmission distance. The final step is to save the configuration. Type **save filename,** where **filename** is the name you would like to use for the configuration file. Multiple configuration files can be saved and loaded from the internal memory. If you run into an error saving the file, make sure that you performed a factory reset before beginning the configuration. Lastly type **save** which will overwrite the running configuration file (*config*). The module is now ready to be rebooted and used. Appendix C shows a list of all the configuration parameters for the access point.

To configure the module which functions as the client in the network, place the module in command mode. Type **set w s SSID**, where **SSID** is the SSID of the access point which will be automatically connected upon startup. The current firmware does not allow the access point to have a password, so the password stored on the client module is irrelevant. Next type **set w r 0** to set the wireless data rate. Then type **set w j 1** to configure the module to automatic login to the access point. Now type **set u b 57600** which allows the module to communicate with the ArduPilot at the baud rate of 57600. When the module is rebooted, the baud rate in Tera Term must be adjusted. Next type **set w a 0** which specifies that the access point which the client is

logging into has open authentication. Type **set w c 5** which tells the client that the access point is on channel 5. Type **set u m 0x01** which disables command echo on the UART port. After saving and rebooting, the user will no longer be able to see the characters as they are typed in Tera Term. Command echo is disabled because it is unnecessary and increases processing on the ArduPilot. The final step is to save the configuration using the same steps as those used for the access point. The module is now ready to reboot. If configured correctly and the access point is on, the module will automatically login to the access point on boot, and this can be seen in Tera Term (Figure 55). A list of all the configuration parameters is show in Appendix D. The average parameter was adjusted to 1 for this research; however, it has no effect on data collection because the last RSS value is always used when the **show r** command is invoked. For thoroughness, to set the average to 1, type **set o a 1**.

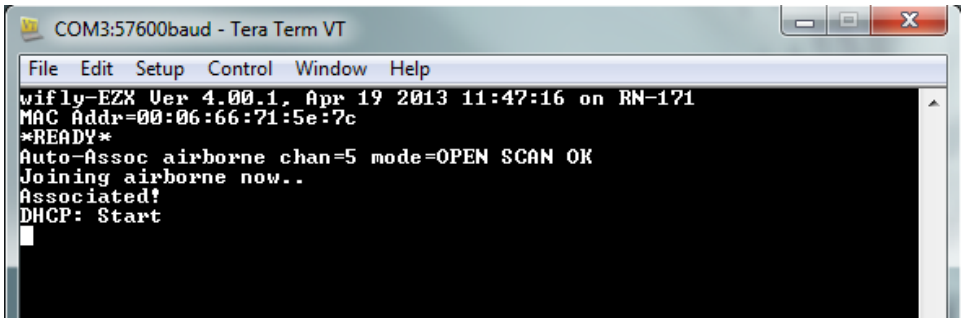

Figure 55: Message received from client module on startup.

B.3. Troubleshooting configuration

In order to troubleshoot operations between the ArduPilot and the client, Wi-Fi module, two circuit configurations were used to listen to the serial data traffic. The configuration in Figure 56 was used to listen to the data coming from the ArduPilot and received by the Wi-Fi module, while the configuration in Figure 57 was used to listen to the data coming from the Wi-Fi module and received by the ArduPilot. The XtreamBee Xbee adapter switch is in the master

position for both configurations. Tera Term is used to display the serial data stream on the connected computer.

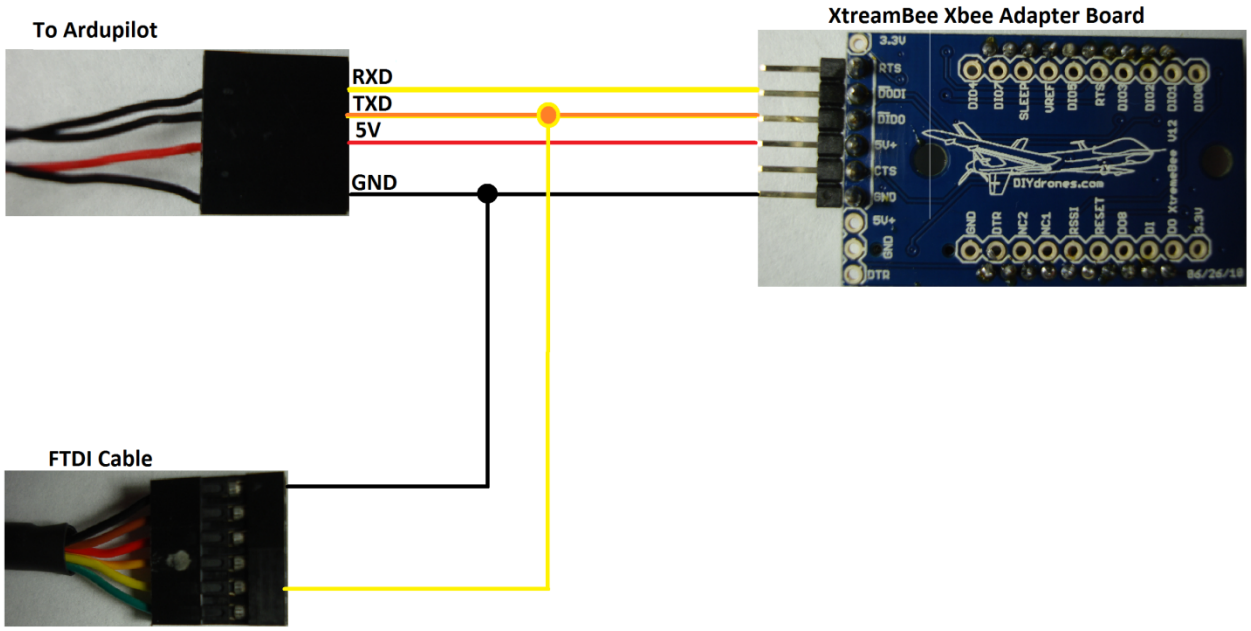

Figure 56: Configuration to listen to data coming from ArduPilot.

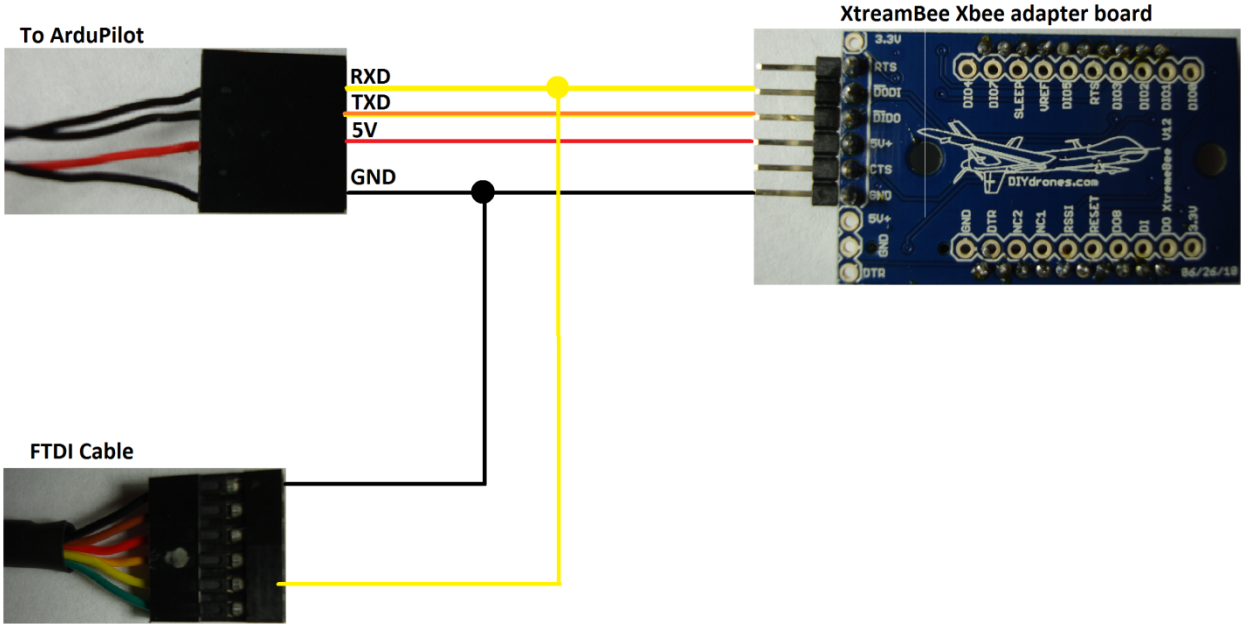

Figure 57: Configuration to listen to data coming from Wi-Fi module.

Appendix C. Access point Configuration Parameters.

```
<4.00> get e
wifly-EZX Ver 4.00.1, Apr 19 2013 11:47:20 on RN-171
Beacon=102
Reboot=0
IF=UP
DHCP=SERVER
IP=0.0.0.0:2000
NM=255.255.255.0
GW=0.0.0.0
HOST=0.0.0.0:2000
PROTO=TCP,
MTU=1524
FLAGS=0x7
TCPMODE=0x0
BACKUP=0.0.0.0
OPEN=*OPEN*
CLOSE=*CLOS*
REMOTE=*HELLO*
FlushSize=1420
MatchChar=0
FlushTimer=5
IdleTimer=0
CmdChar=$
DNS=0.0.0.0
Name=dns1
Backup=rn.microchip.com
Lease=86400
FTP=0.0.0.0:21
File=wifly-EZX.img
User=roving
Pass=Pass123
Dir=public
Timeout=200
FTP_mode=0x0
SSID=airborne
Chan=5
ExtAnt=0
Join=7
Auth=OPEN
Mask=0x1fff
Rate=0, 1  Mb
Linkmon-Infra=30
Linkmon-AP=3600
Passphrase=rubygirl
TxPower=12
EAP_Id=userid
EAP_User=peap-user
SleepTmr=0
WakeTmr=0
```

```
Trigger=0x1
Autoconn=0
IoFunc=0x0
IoMask=0x21f0
IoValu=0x0
DebugReg=0x0
PrintLvl=0x1
LaunchStr=web_app
TimeEna=0
TIMEADR=64.90.182.55:123
Zone=7
Baudrate=9600
Flow=0x0
Mode=0x0
Cmd_GPIO=0
JoinTmr=1000
Replace=0x24
DeviceId=WiFly-EZX
Password=
Format=0x0
Signal=0
Average=5
BCAST=255.255.255.255:55555
Interval=0x7
Backup=0.0.0.0:0
Sensor=0x0
SensePwr=0x0
<4.00>
```

Appendix D. Client Configuration Parameters

```
<4.00> get e
wifly-EZX Ver 4.00.1, Apr 19 2013 11:47:20 on RN-171
Beacon=102
Reboot=0
IF=UP
DHCP=ON
IP=0.0.0.0:2000
NM=0.0.0.0
GW=0.0.0.0
HOST=0.0.0.0:2000
PROTO=TCP,
MTU=1524
FLAGS=0x7
TCPMODE=0x0
BACKUP=0.0.0.0
OPEN=*OPEN*
CLOSE=*CLOS*
REMOTE=*HELLO*
FlushSize=1420
MatchChar=0
FlushTimer=5
IdleTimer=0
CmdChar=$
DNS=0.0.0.0
Name=dns1
Backup=rn.microchip.com
Lease=86400
FTP=0.0.0.0:21
File=wifly-EZX.img
User=roving
Pass=Pass123
Dir=public
Timeout=200
FTP_mode=0x0
SSID=airborne
Chan=0
ExtAnt=0
Join=1
Auth=OPEN
Mask=0x1fff
Rate=0, 1  Mb
Linkmon-Infra=30
Linkmon-AP=3600
Passphrase=open
TxPower=12
EAP_Id=userid
EAP_User=peap-user
SleepTmr=0
WakeTmr=0
```

```
Trigger=0x1
Autoconn=1
IoFunc=0x0
IoMask=0x21f0
IoValu=0x0
DebugReg=0x0
PrintLvl=0x1
LaunchStr=web_app
TimeEna=0
TIMEADR=64.90.182.55:123
Zone=7
Baudrate=57600
Flow=0x0
Mode=0x1
Cmd_GPIO=0
JoinTmr=1000
Replace=0x24
DeviceId=WiFly-EZX
Password=
Format=0x0
Signal=92
Average=1
BCAST=255.255.255.255:55555
Interval=0x7
Backup=0.0.0.0:0
Sensor=0x0
SensePwr=0x0
<4.00>
```

Appendix E. Supporting Figures

This appendix contains figures from all three scenarios and supports the results section of this thesis.

E.1. Air-to-Air Scenario Figures

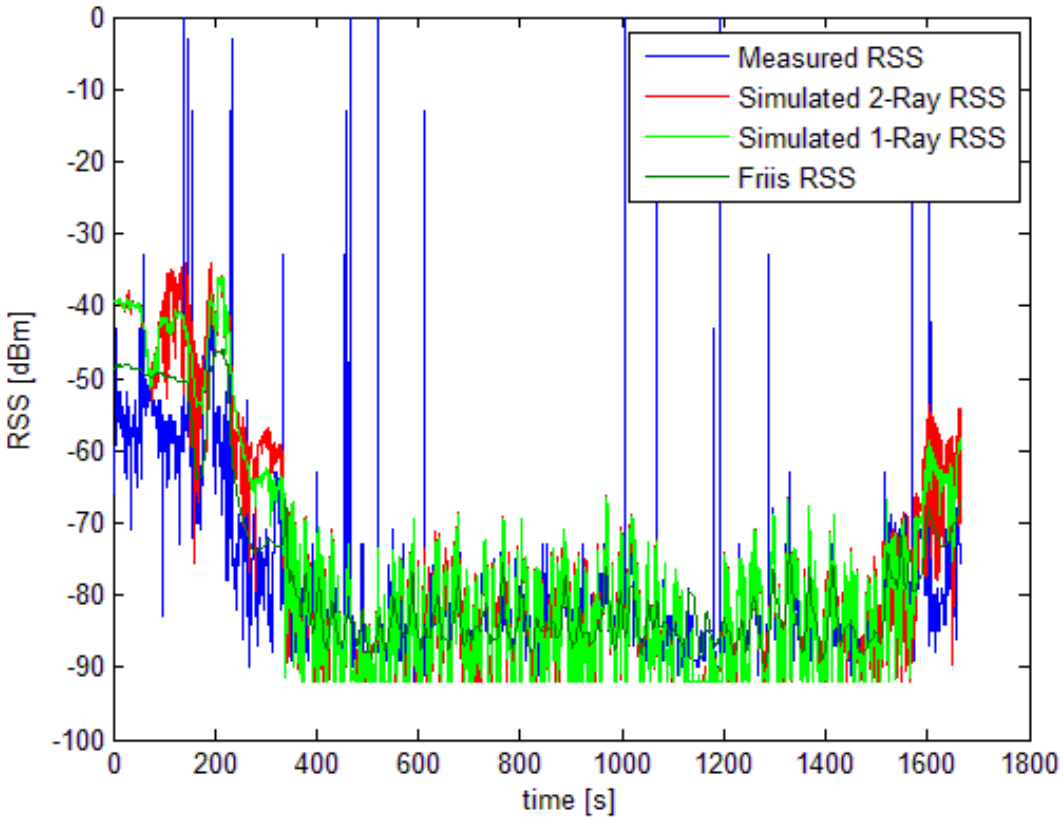

Figure 58: RSS vs. Time for AtoA Scenario using Raw Heading.

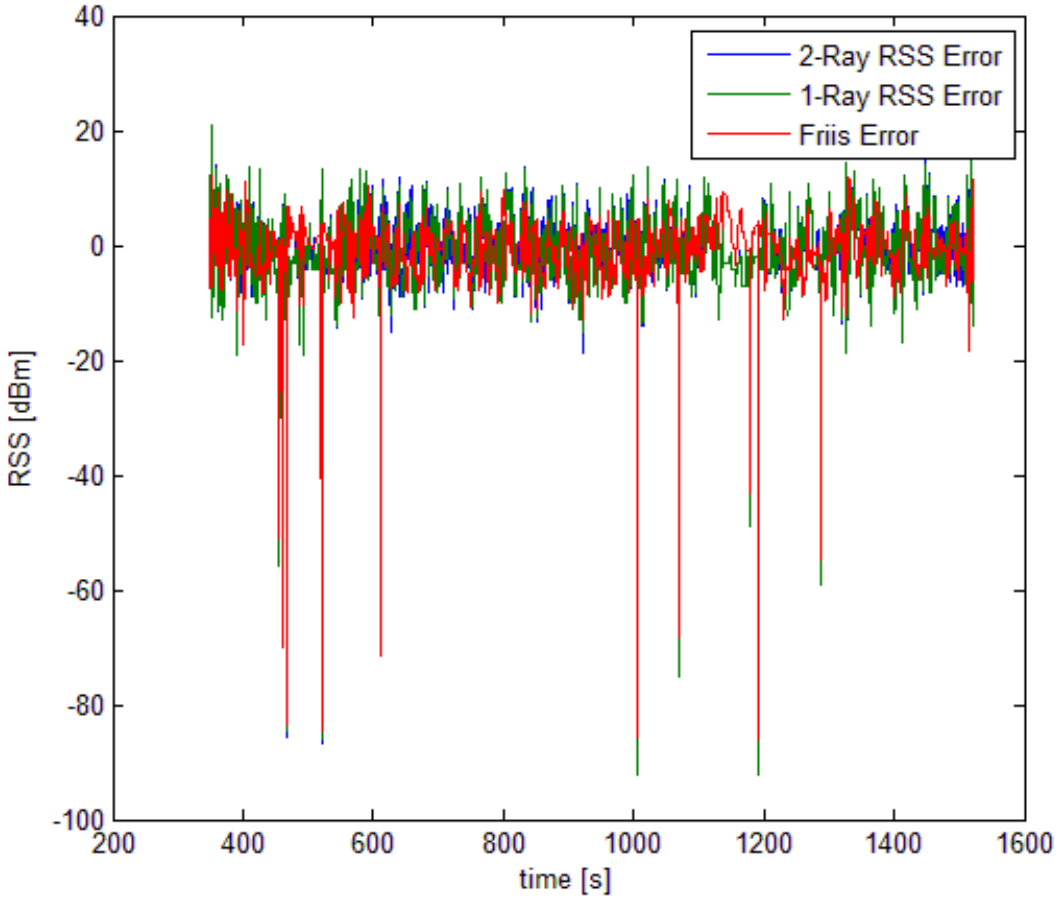

Figure 59: Error vs. Time for AtoA Scenario using Raw Heading.

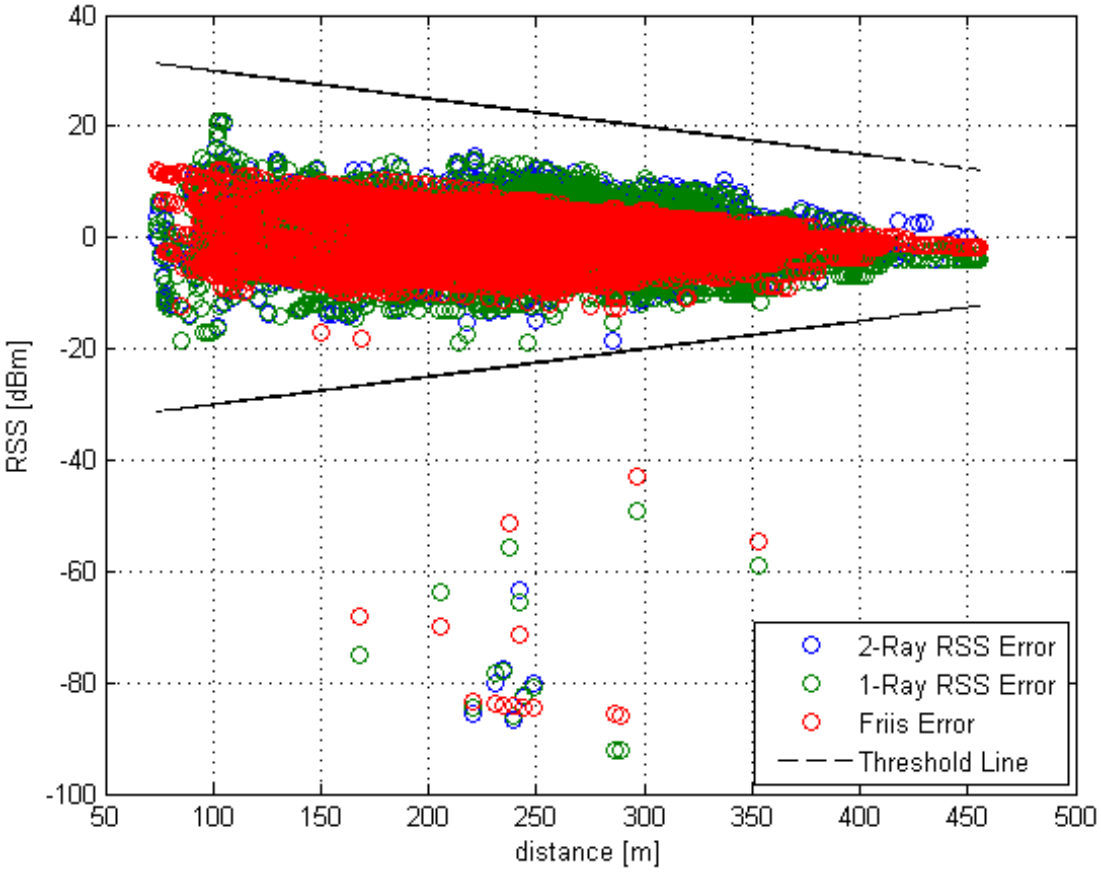

Figure 60: Scatter Plot of Error vs. Distance for AtoA Scenario using Raw Heading.

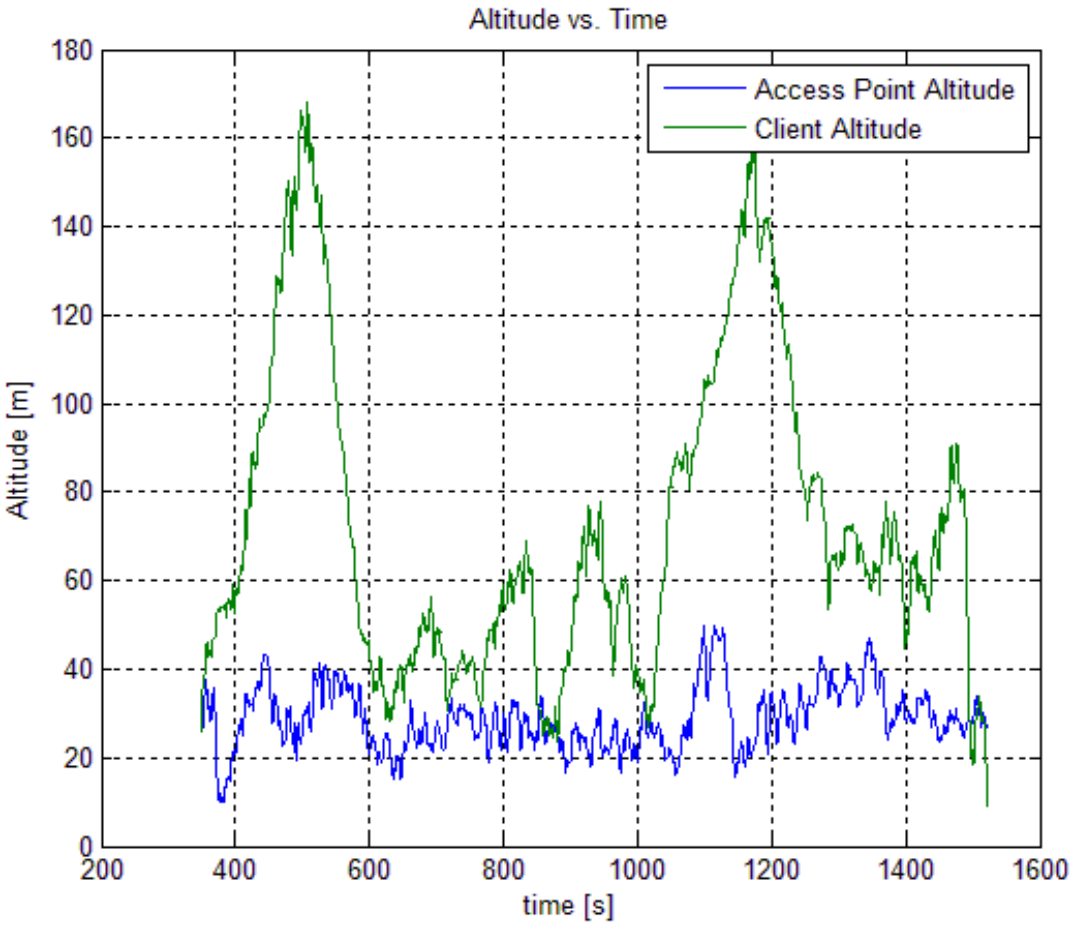

Figure 61: Altitude vs. Time for AtoA Scenario.

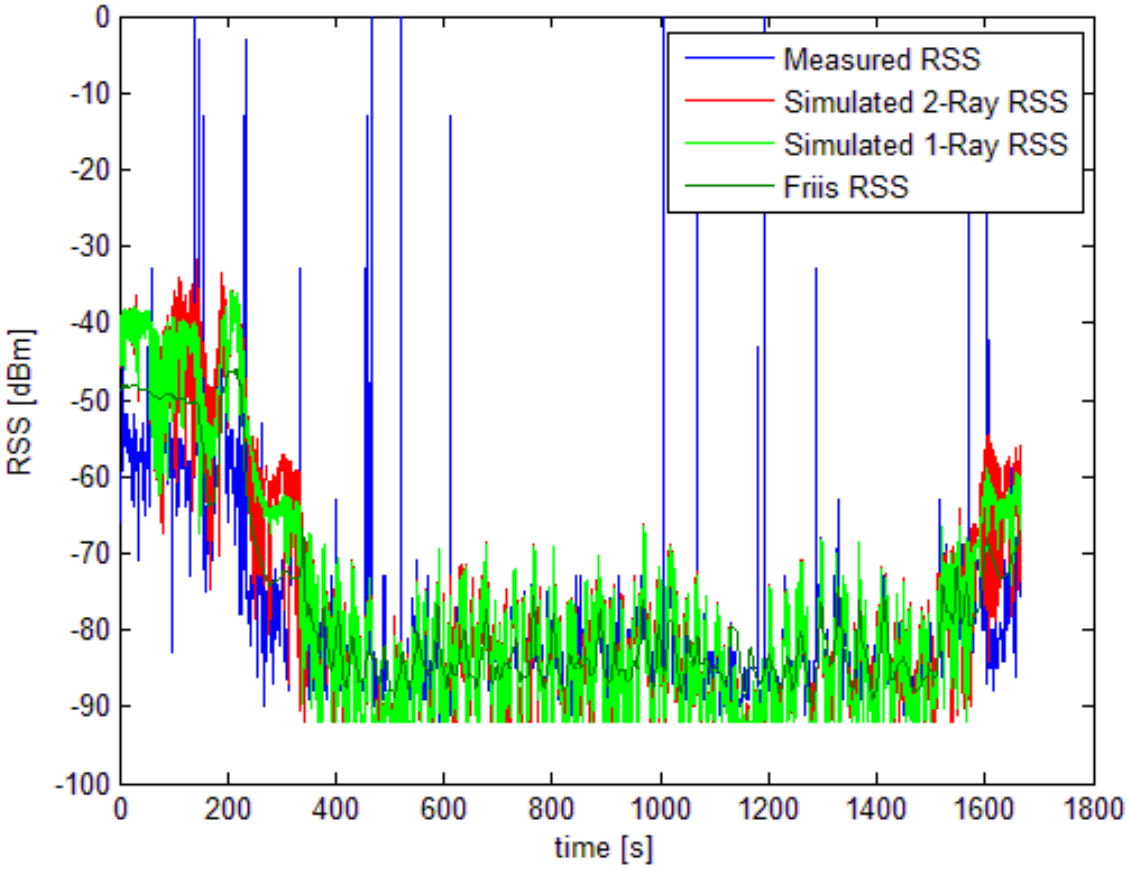

Figure 62: RSS vs. Time for AtoA Scenario using GPS Based Heading.

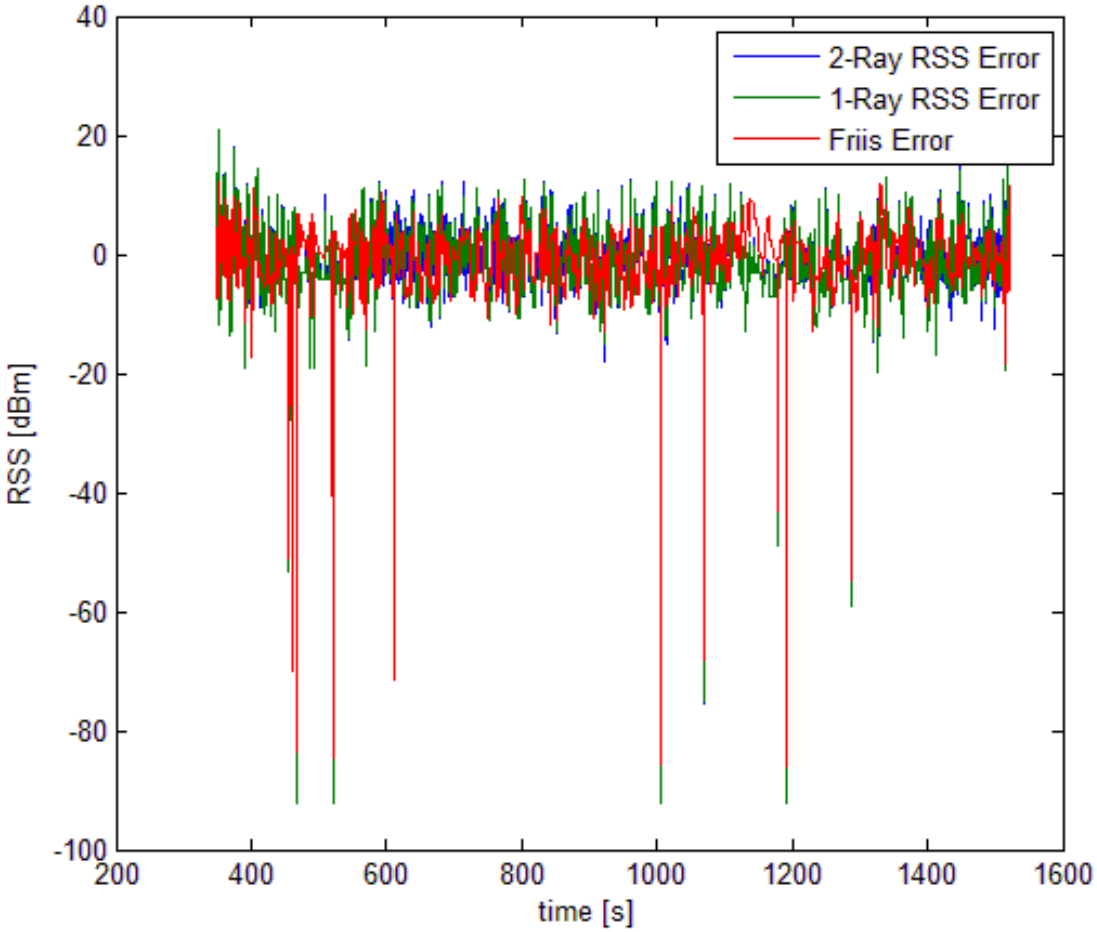

Figure 63: Error vs. Time for AtoA Scenario using GPS Based Heading.

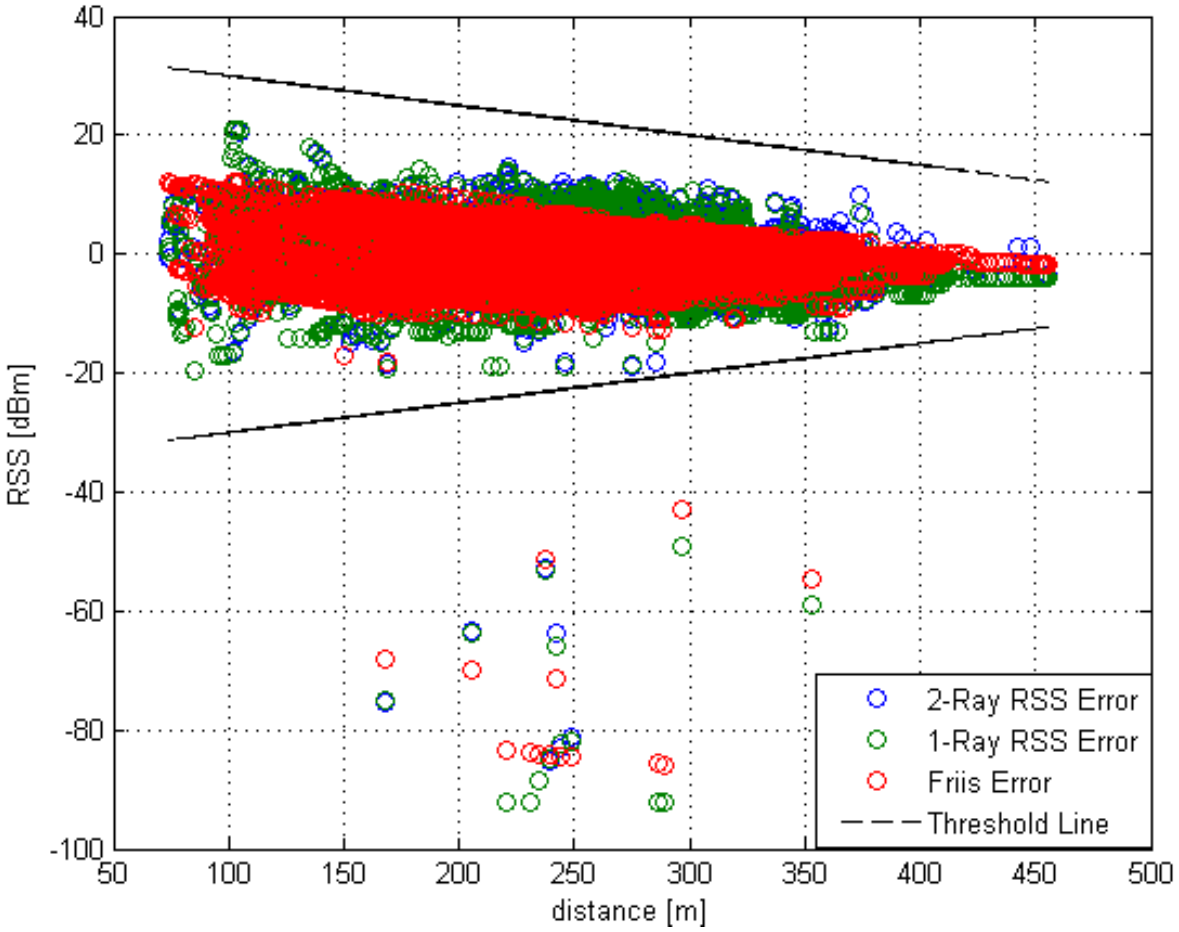

Figure 64: Error vs. Distance for AtoA Scenario using GPS Based Heading.

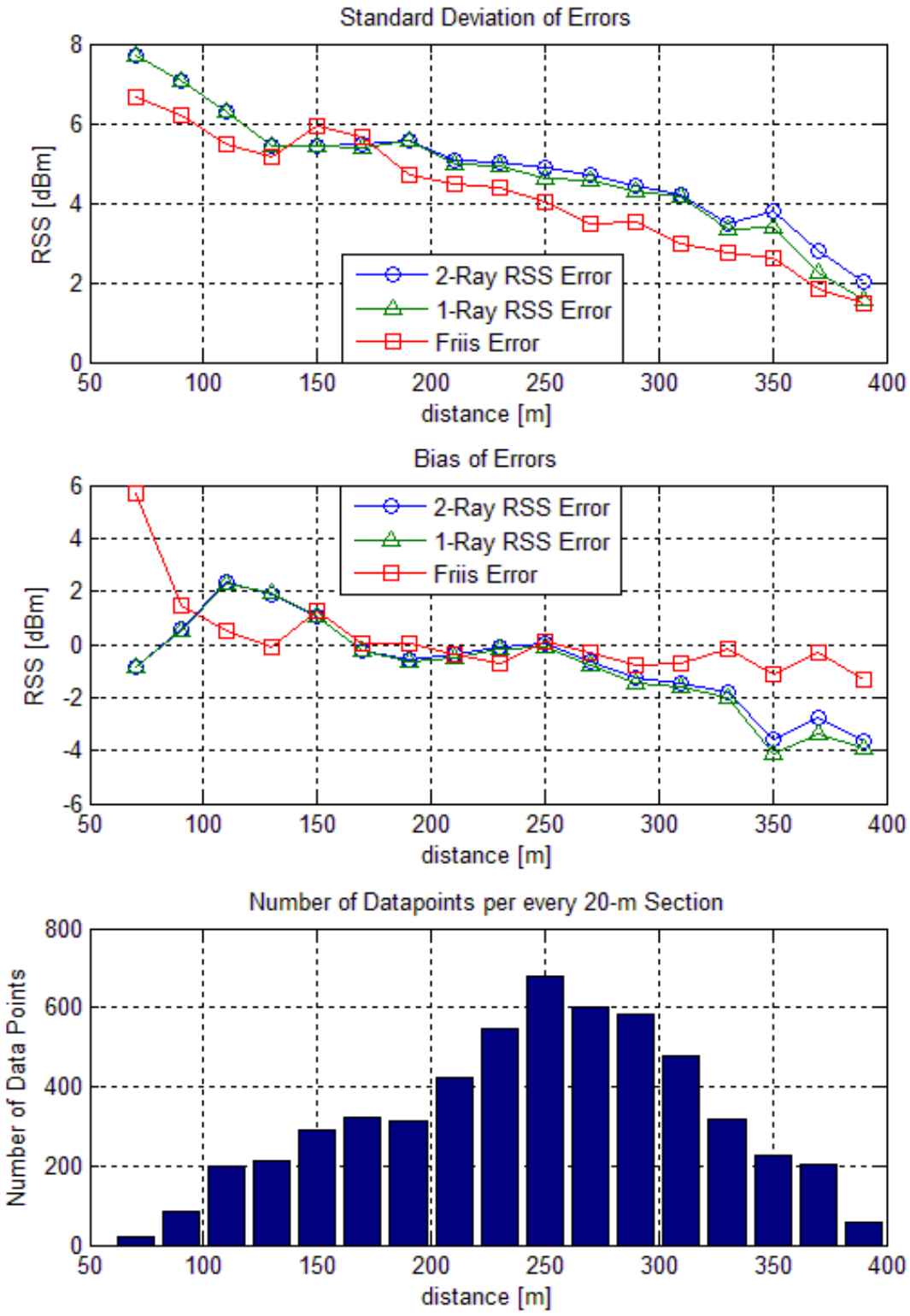

Figure 65: Statistical Analysis of AtoA Scenario with GPS Based Heading.

E.2. Ground-to-Air Scenario Figures

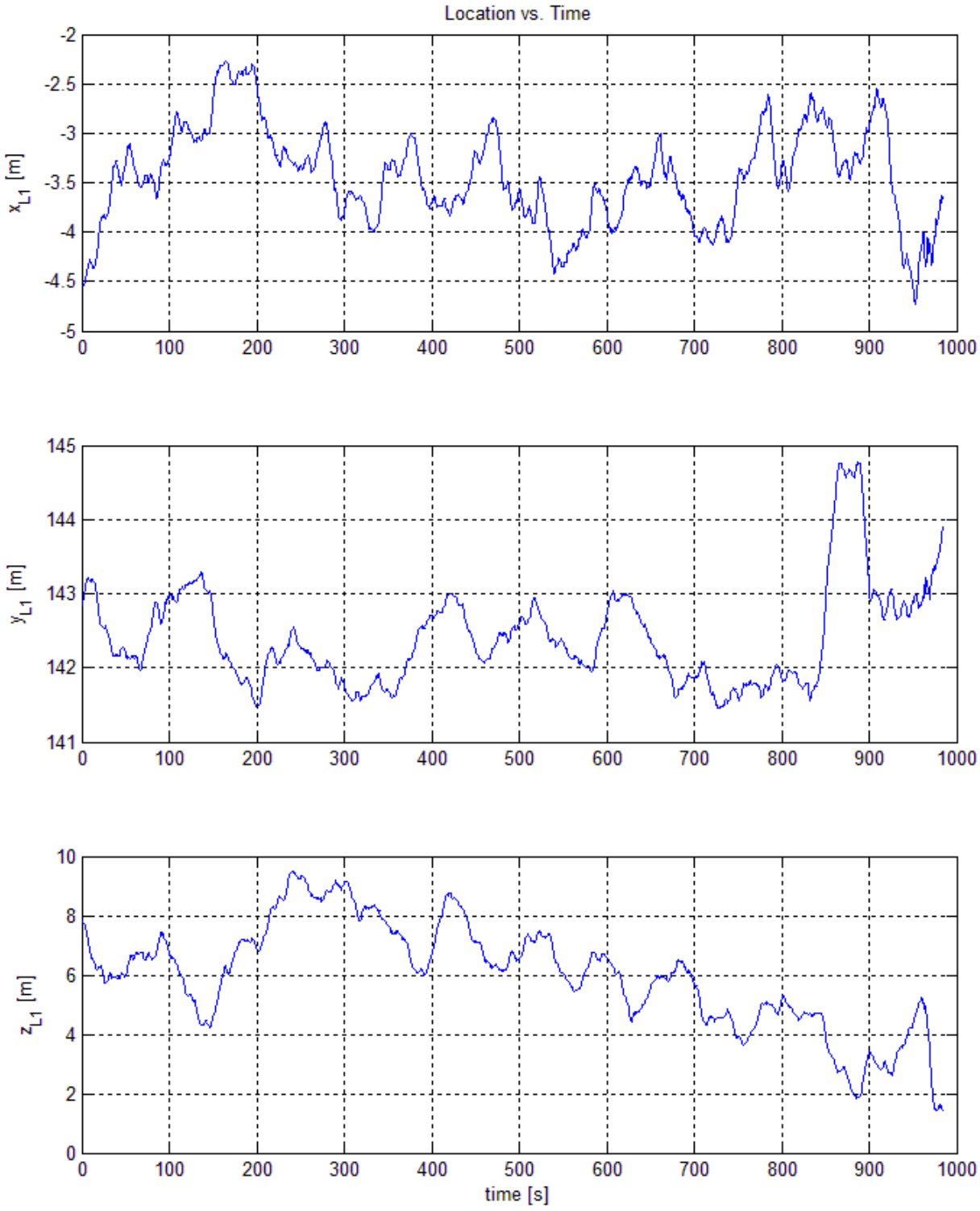

Figure 66: Access Point's Position vs. Time for GtoA Scenario.

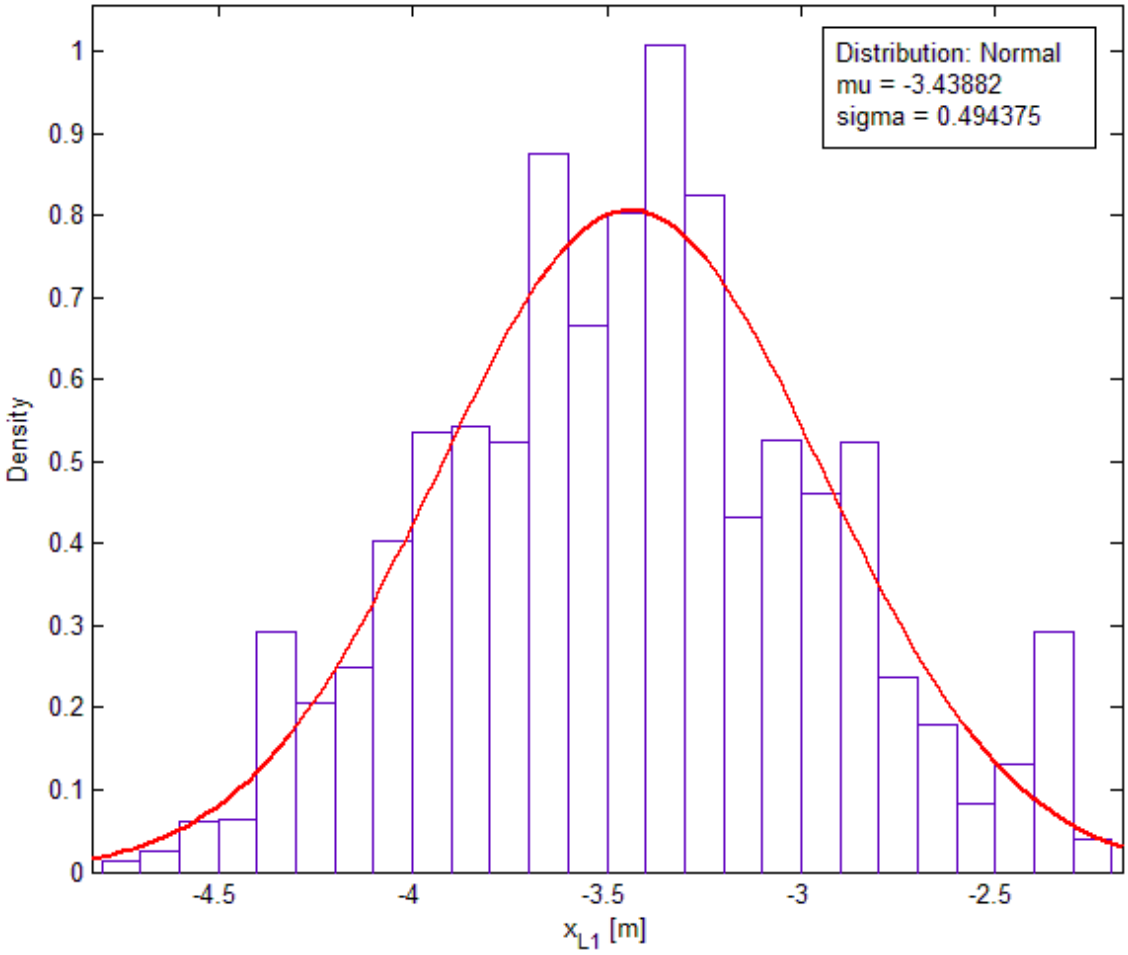

Figure 67: Distribution of *x* location of Access Point for GtoA Scenario.

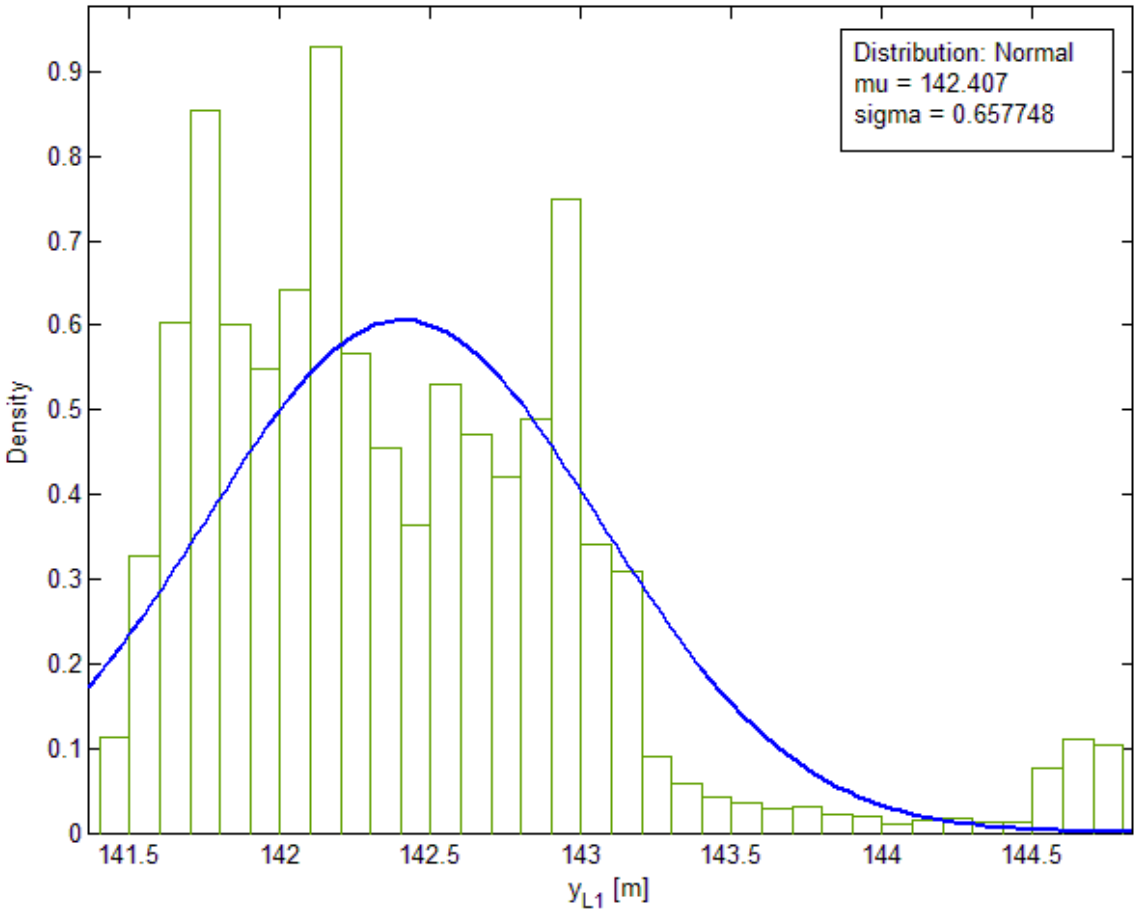

Figure 68: Distribution of *y* location of Access Point for GtoA Scenario.

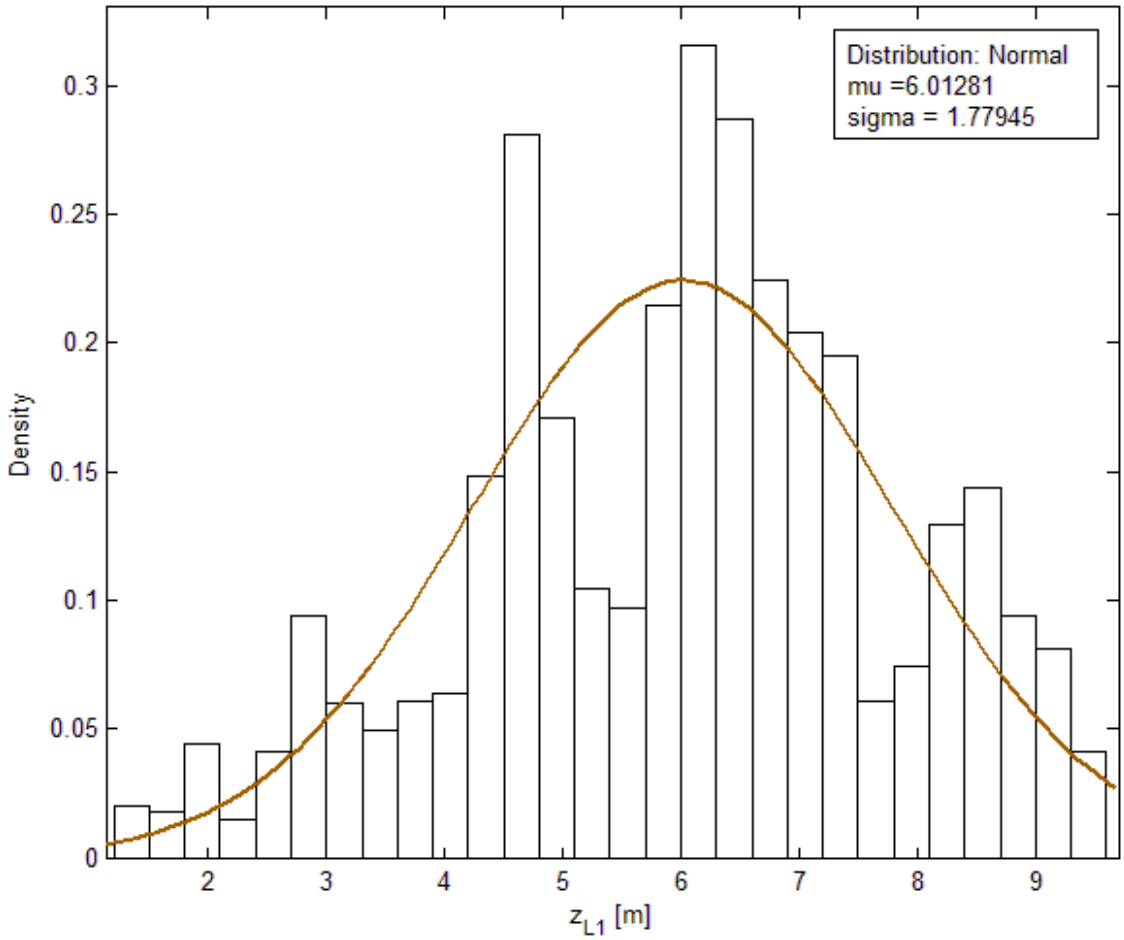

Figure 69: Distribution of *z* location of Access Point for GtoA Scenario.

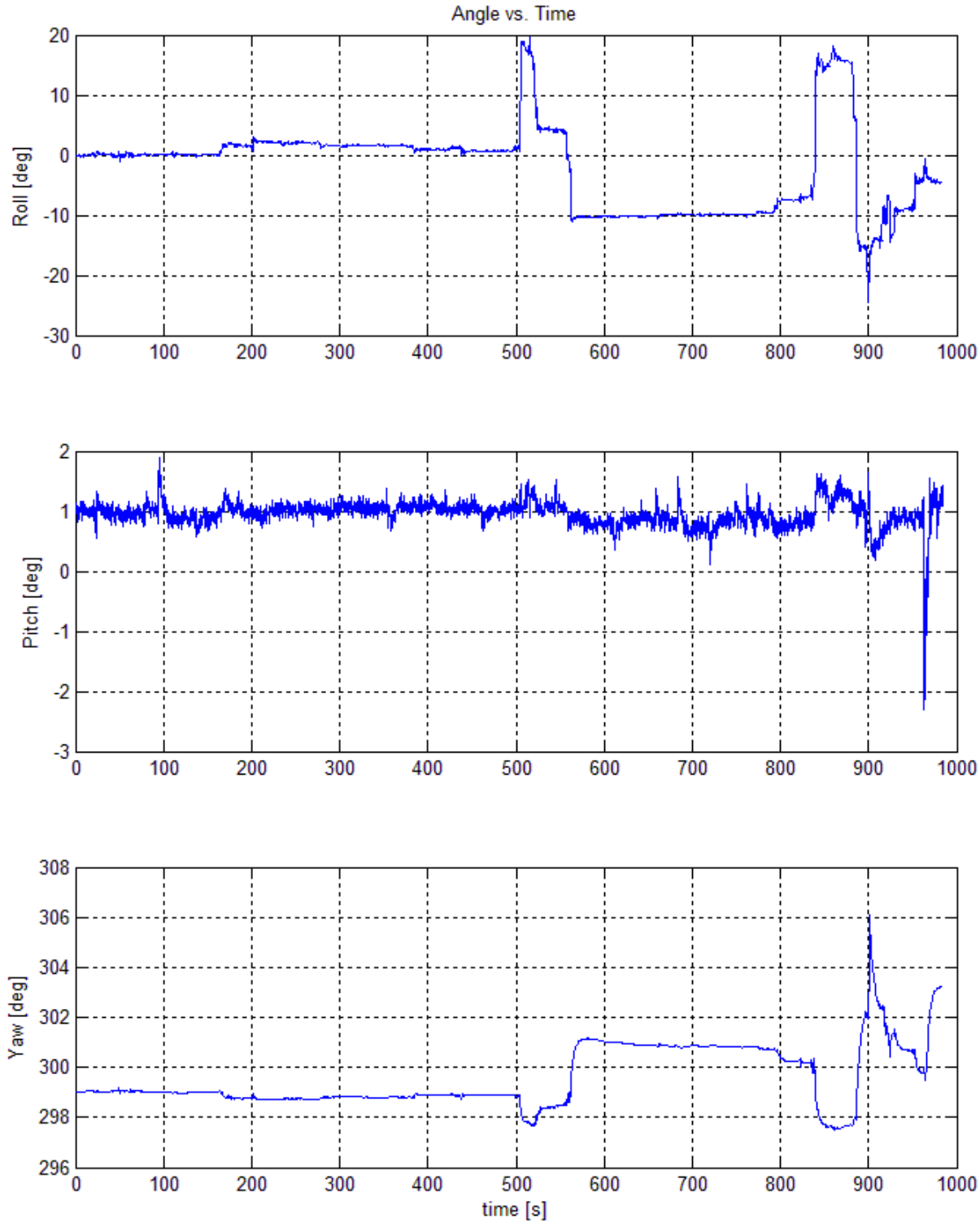

Figure 70: Access Point's Attitude Angles for GtoA Scenario.

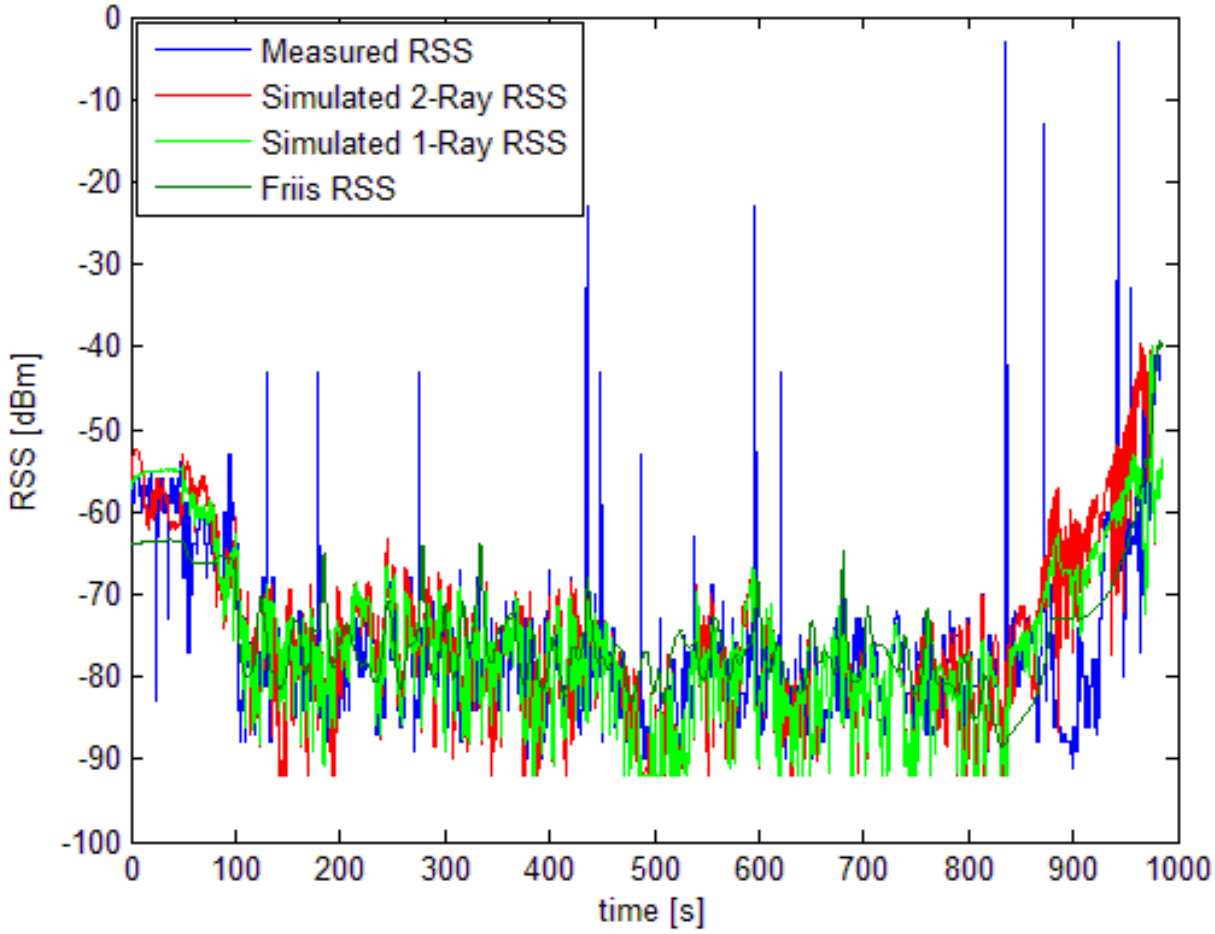

Figure 71: RSS vs. Time for GtoA Scenario using Raw Heading.

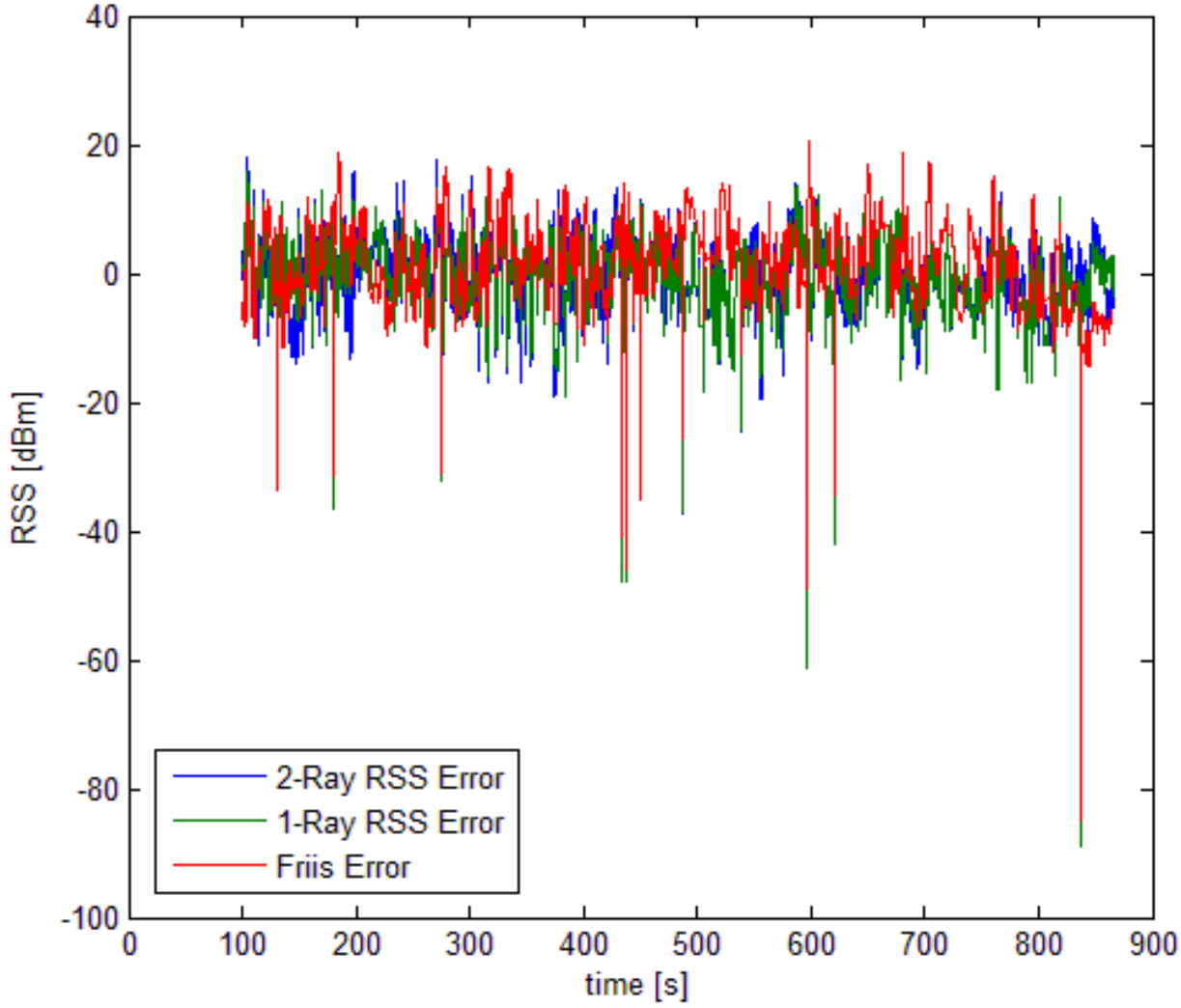

Figure 72: Error vs. Time for GtoA Scenario using Raw Heading.

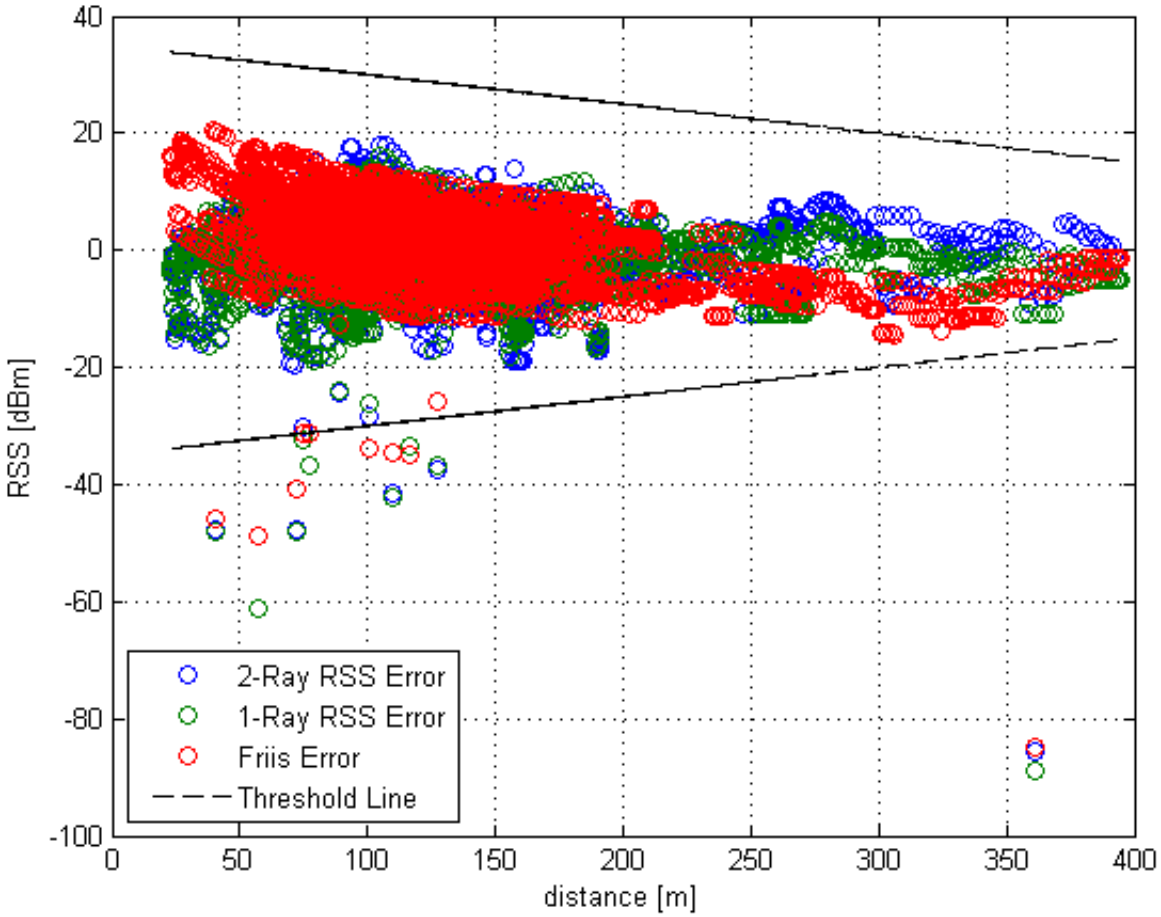

Figure 73: Error vs. Distance for GtoA Scenario using Raw Heading.

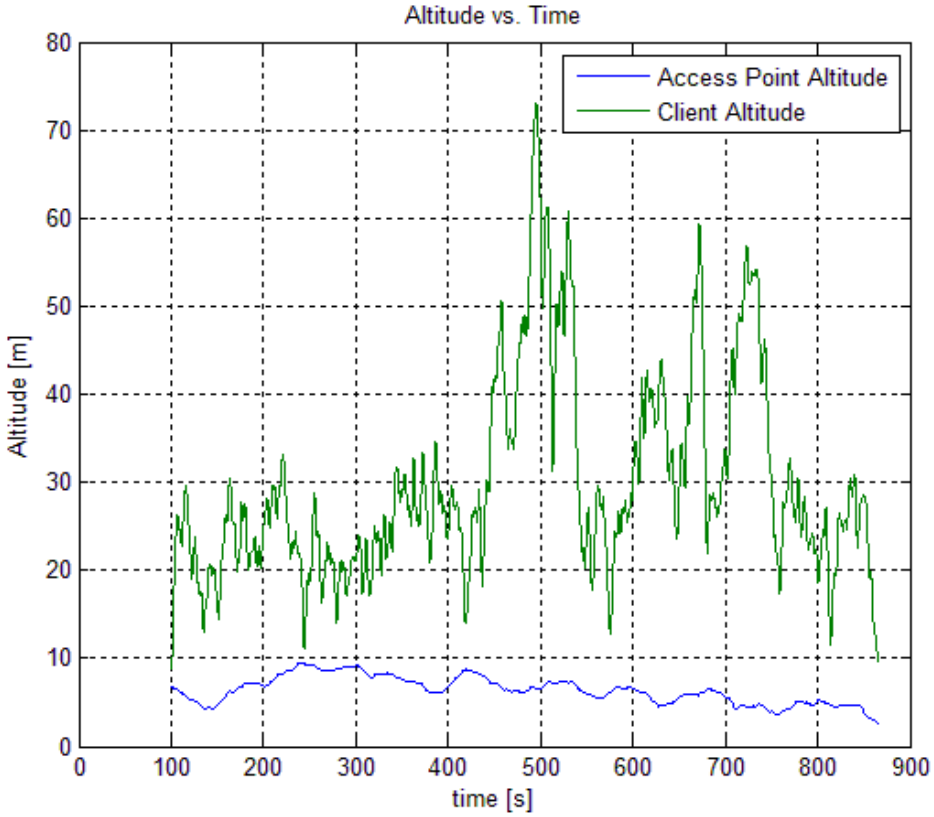

Figure 74: Altitude vs. Time for GtoA Scenario.

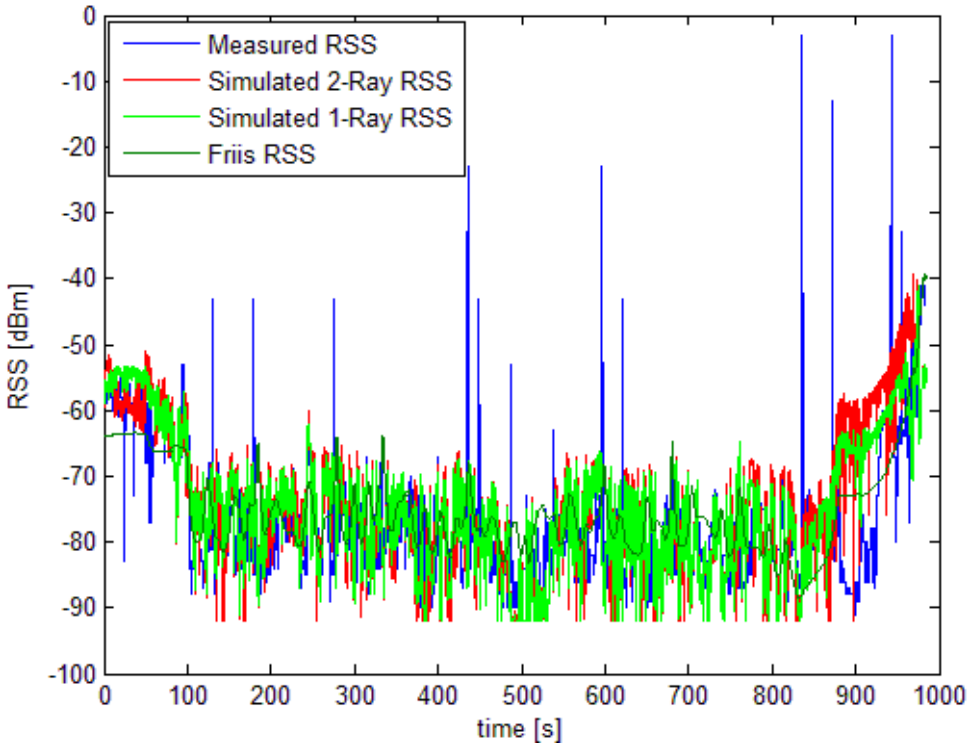

Figure 75: RSS vs. Time for GtoA Scenario using GPS Based Heading.

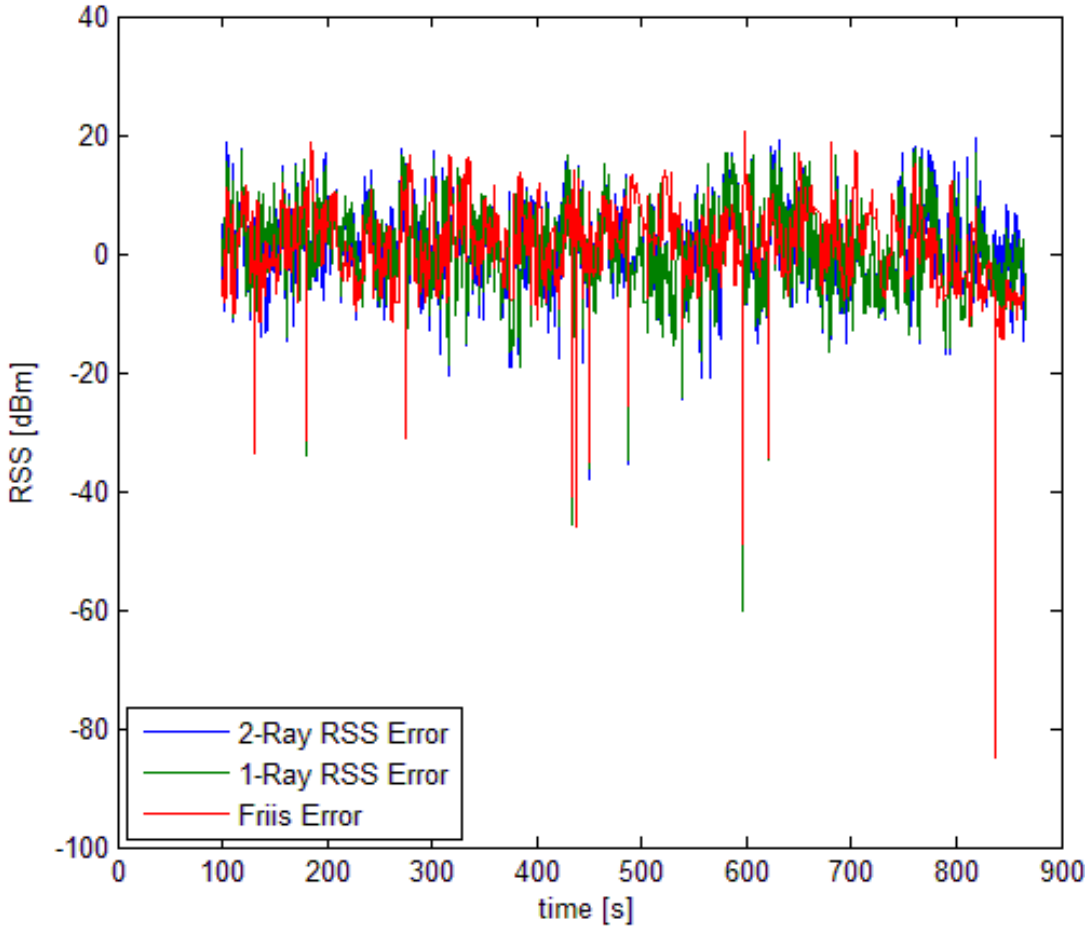

Figure 76: Error vs. Time for GtoA Scenario using GPS Based Heading.

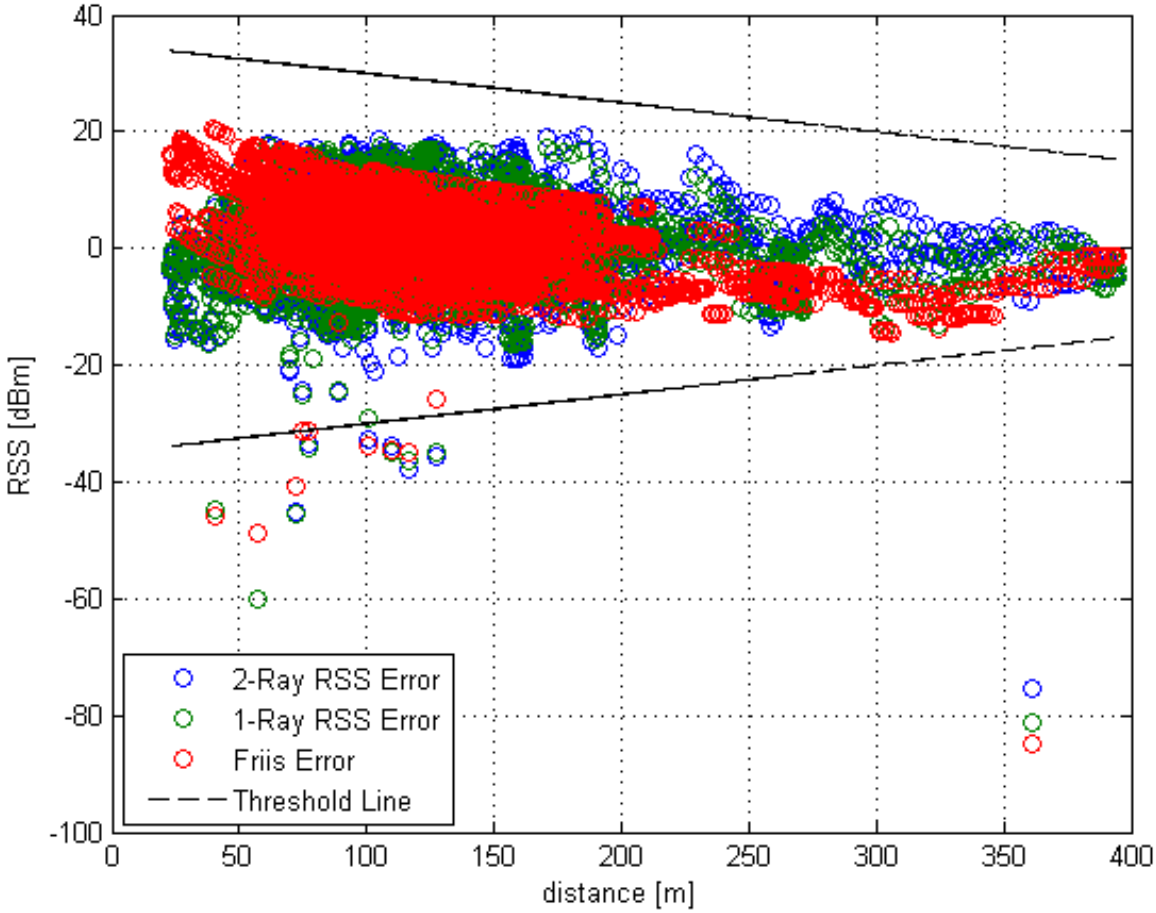

Figure 77: Error vs. Distance for GtoA Scenario using GPS Based Heading.

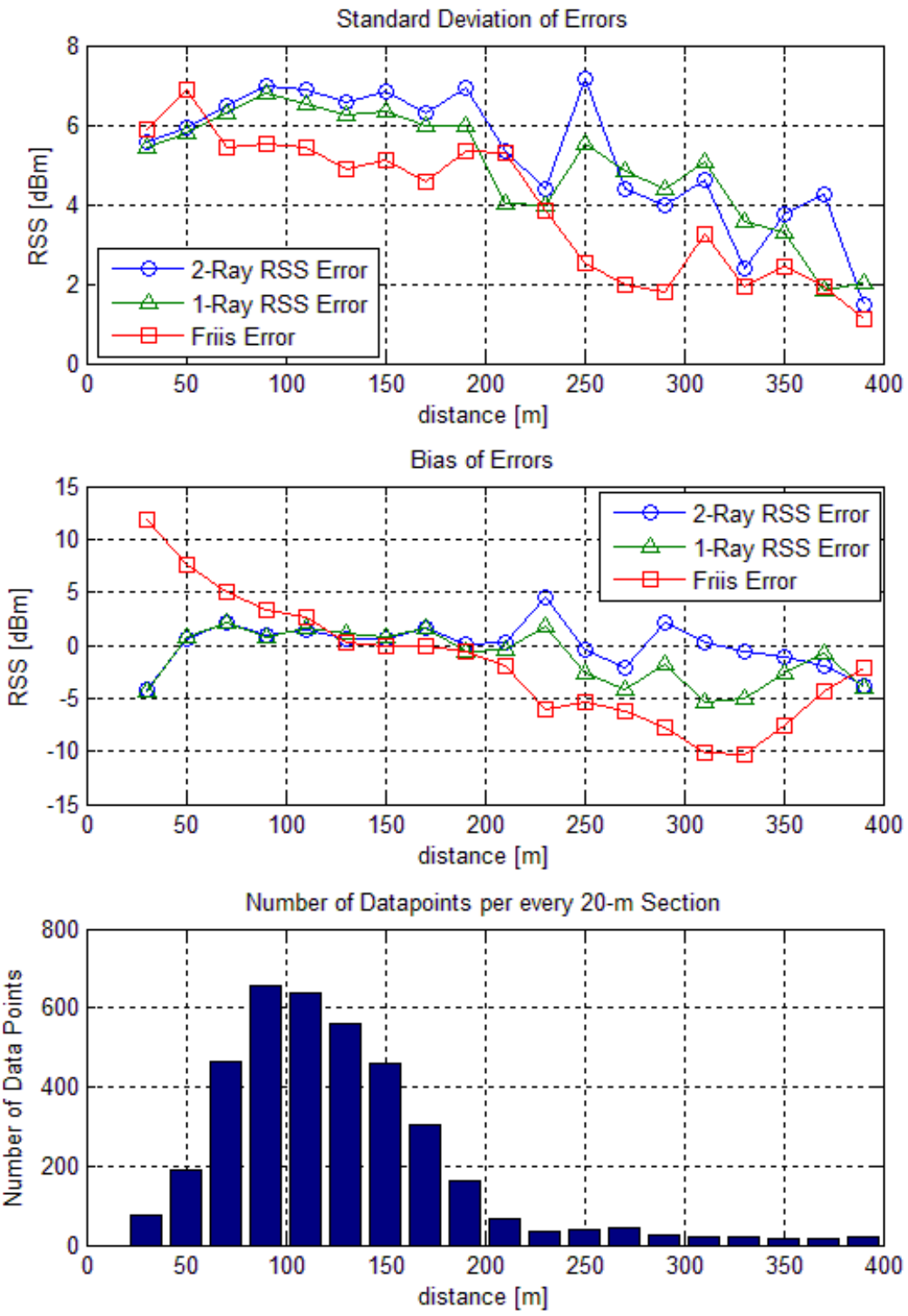

Figure 78: Statistical Analysis of GtoA Scenario with GPS Based Heading.

E.3. Air-to-Ground Scenario Figures

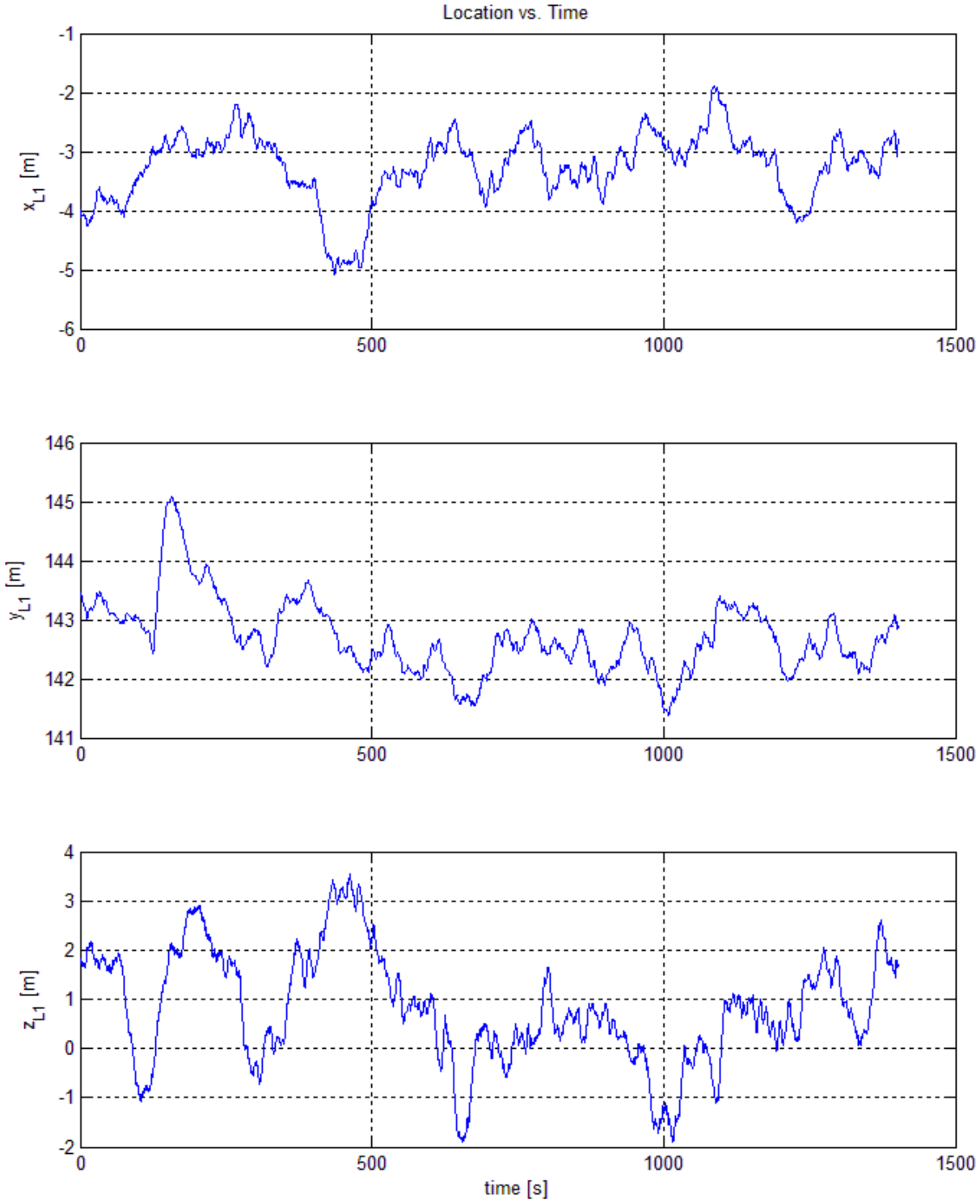

Figure 79: Client's Position vs. Time for AtoG Scenario.

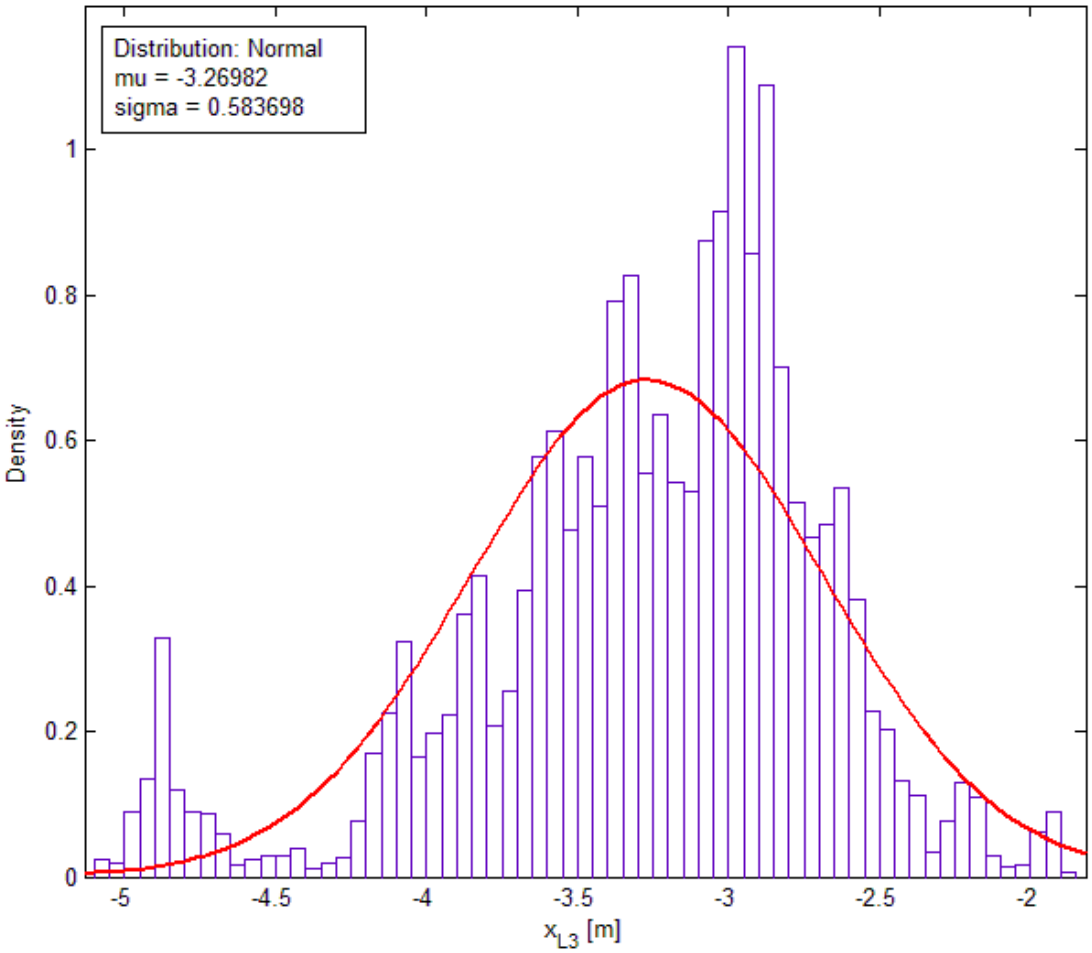

Figure 80: Distribution of *x* location of Client for AtoG Scenario.

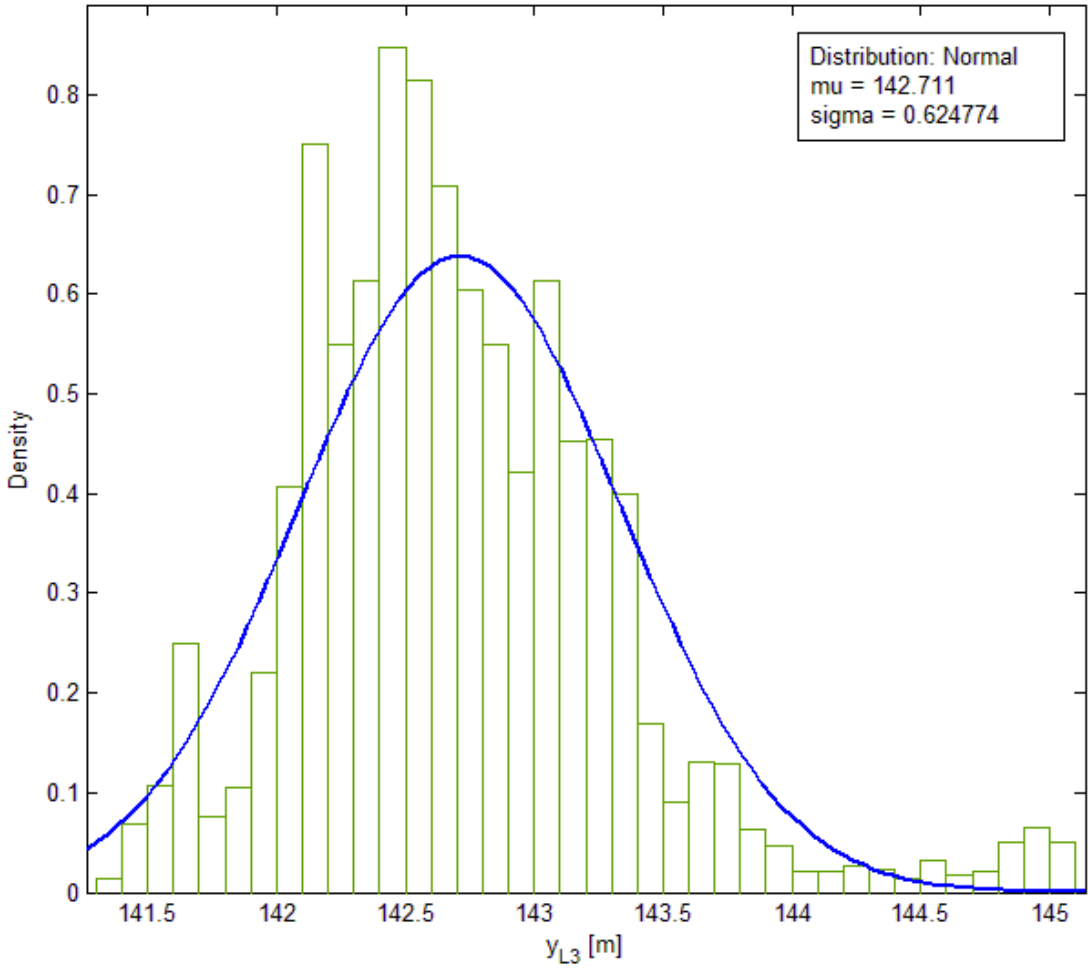

Figure 81: Distribution of *y* location of Client for AtoG Scenario.

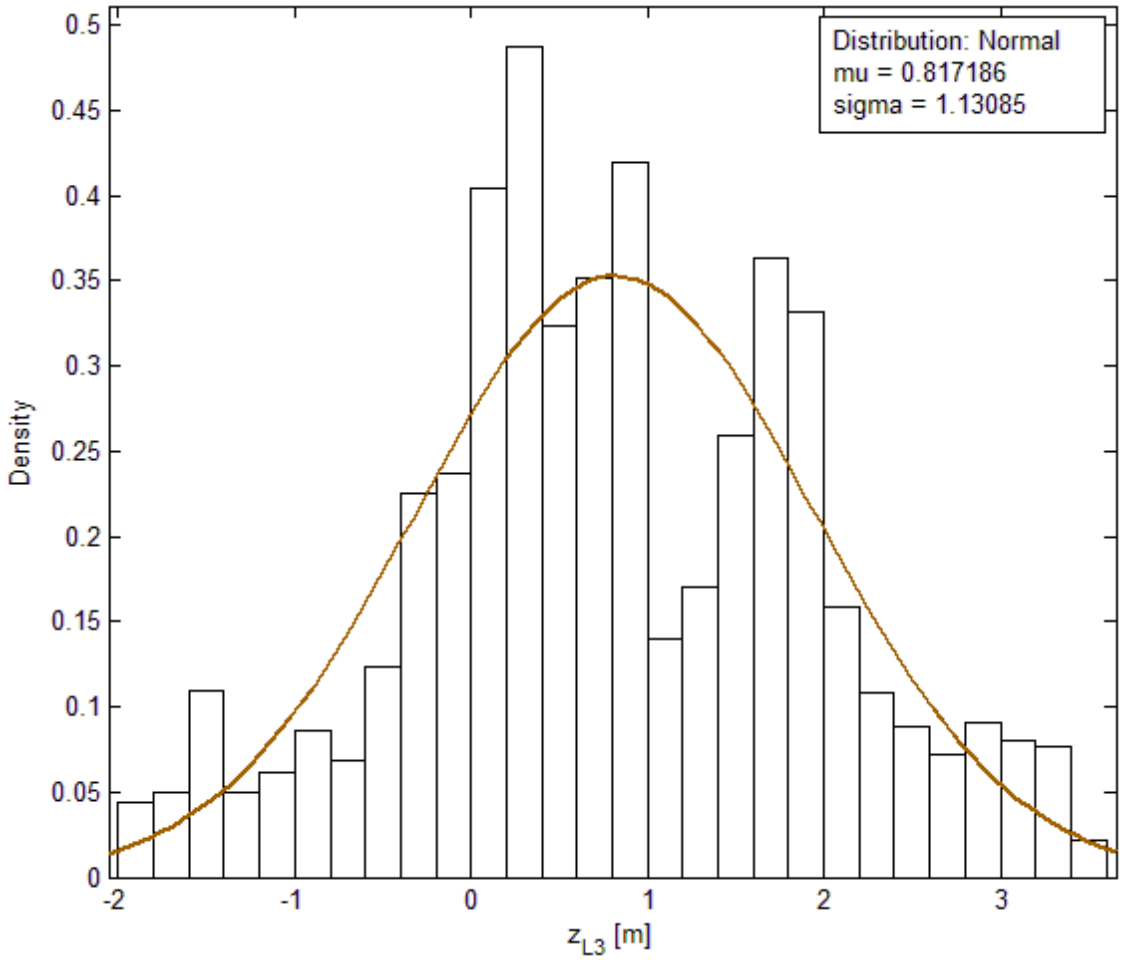

Figure 82: Distribution of *z* location of Client for AtoG Scenario.

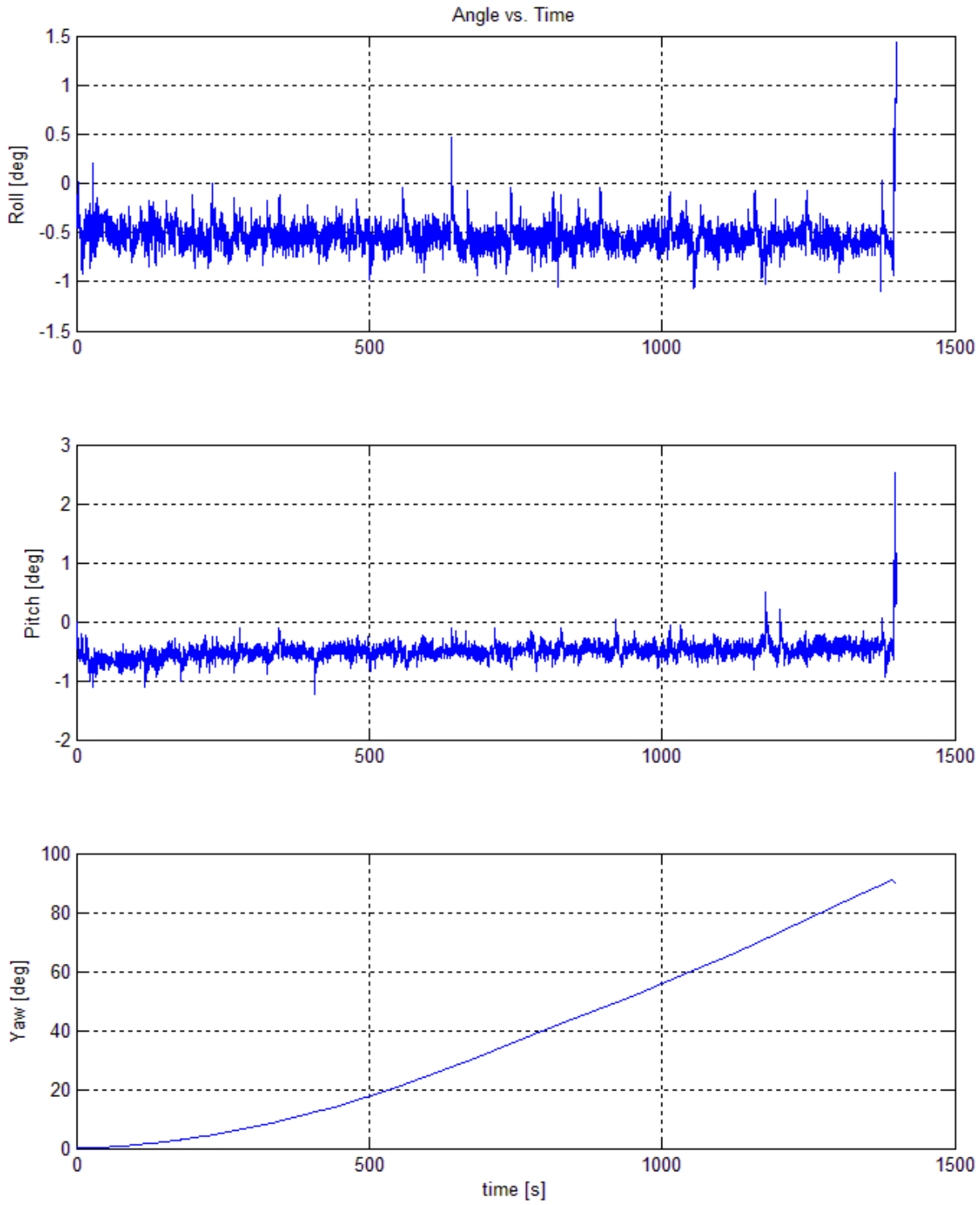

Figure 83: Client's Attitude Angles for AtoG Scenario.

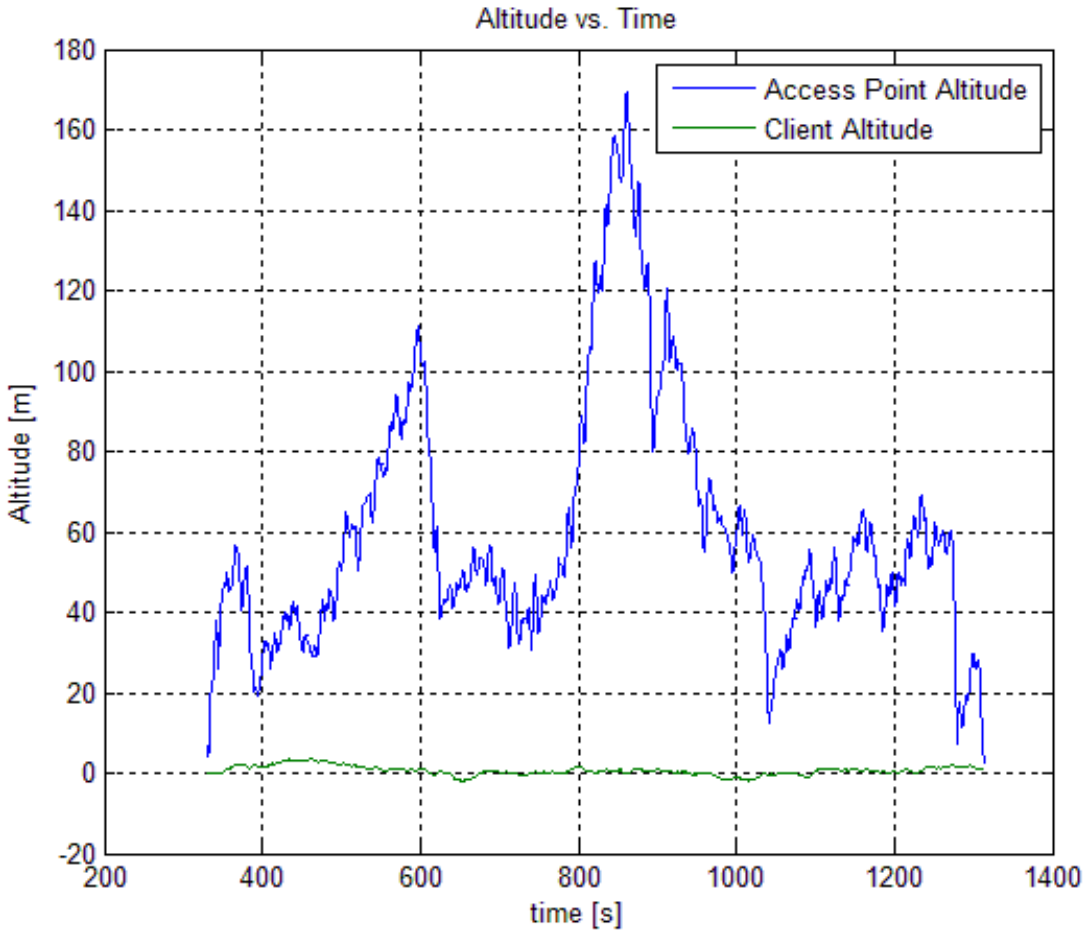

Figure 84: Altitude vs. Time for AtoG Scenario.

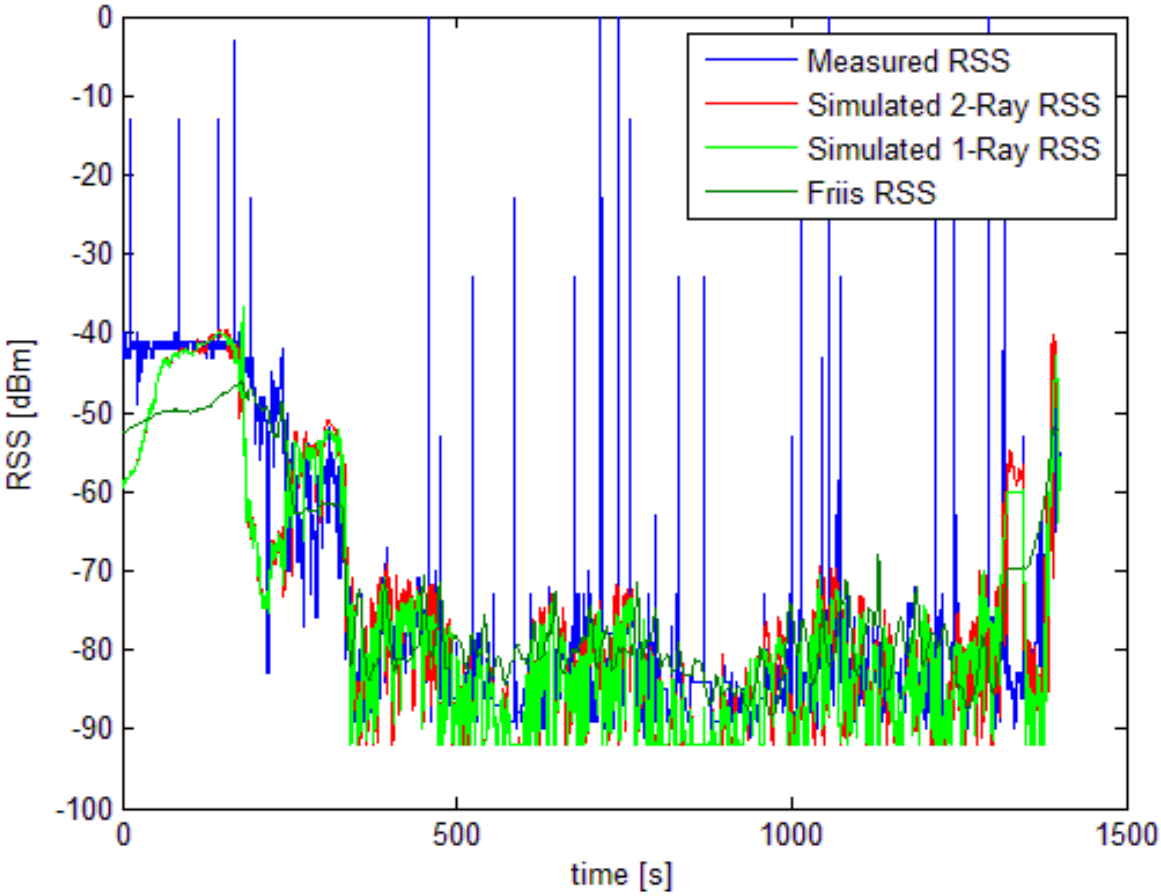

Figure 85: RSS vs. Time for AtoG Scenario using Raw Heading.

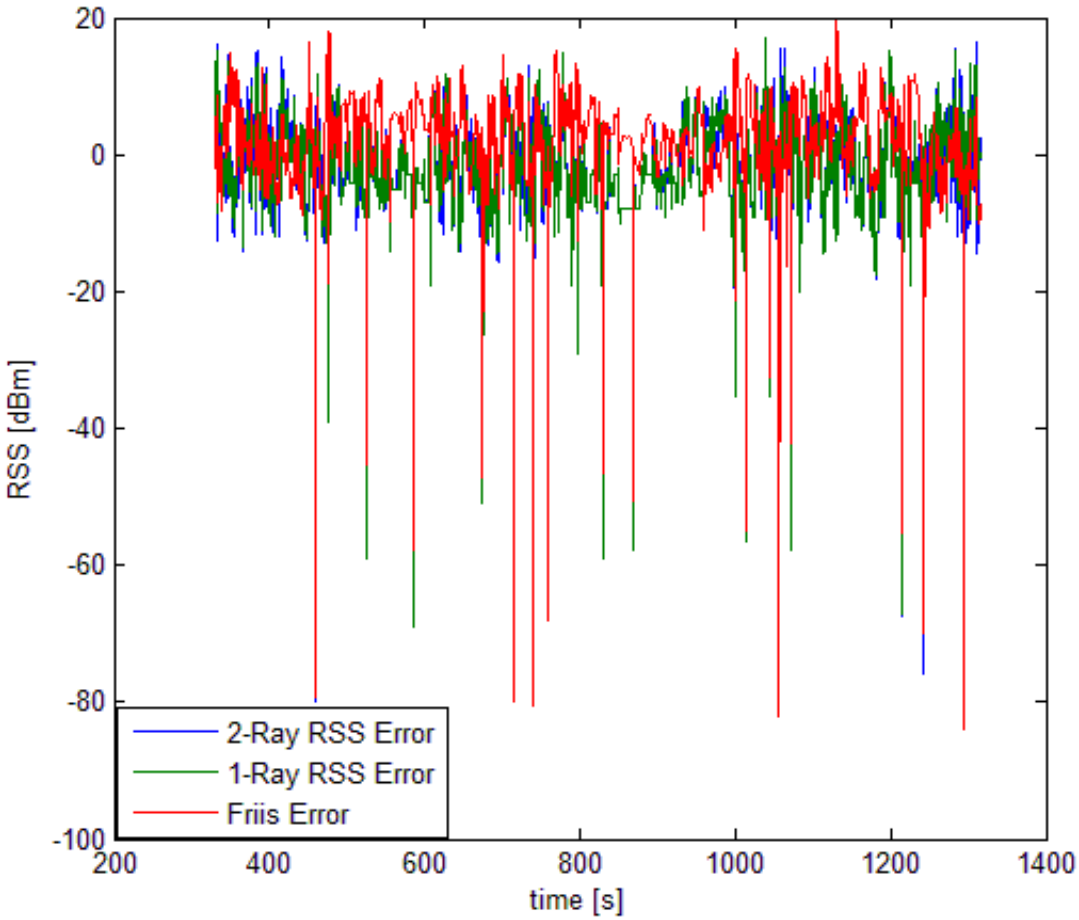

Figure 86: Error vs. Time for AtoG Scenario using Raw Heading.

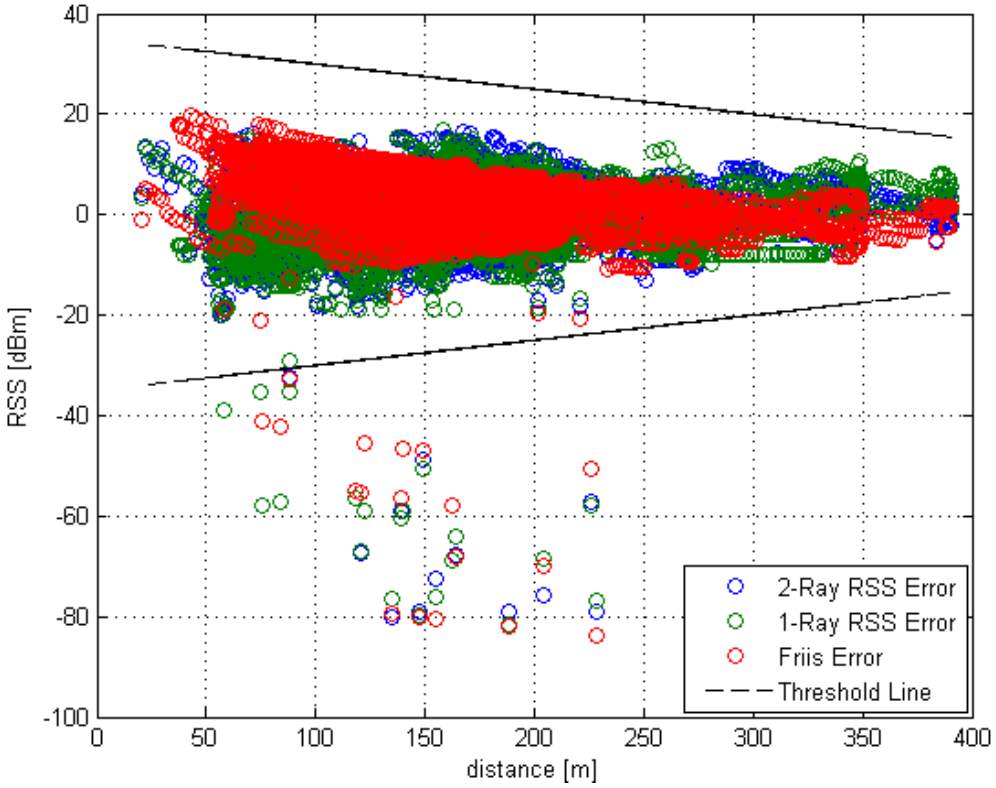

Figure 87: Error vs. Distance for AtoG Scenario using Raw Heading.

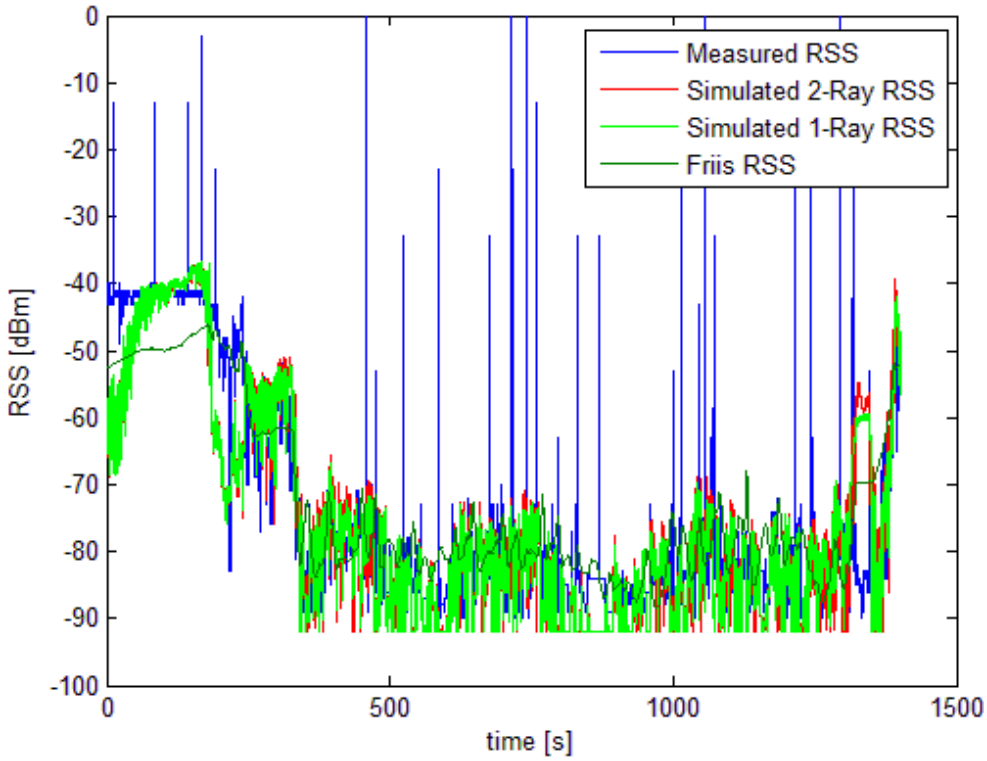

Figure 88: RSS vs. Time for AtoG Scenario using GPS Based Heading.

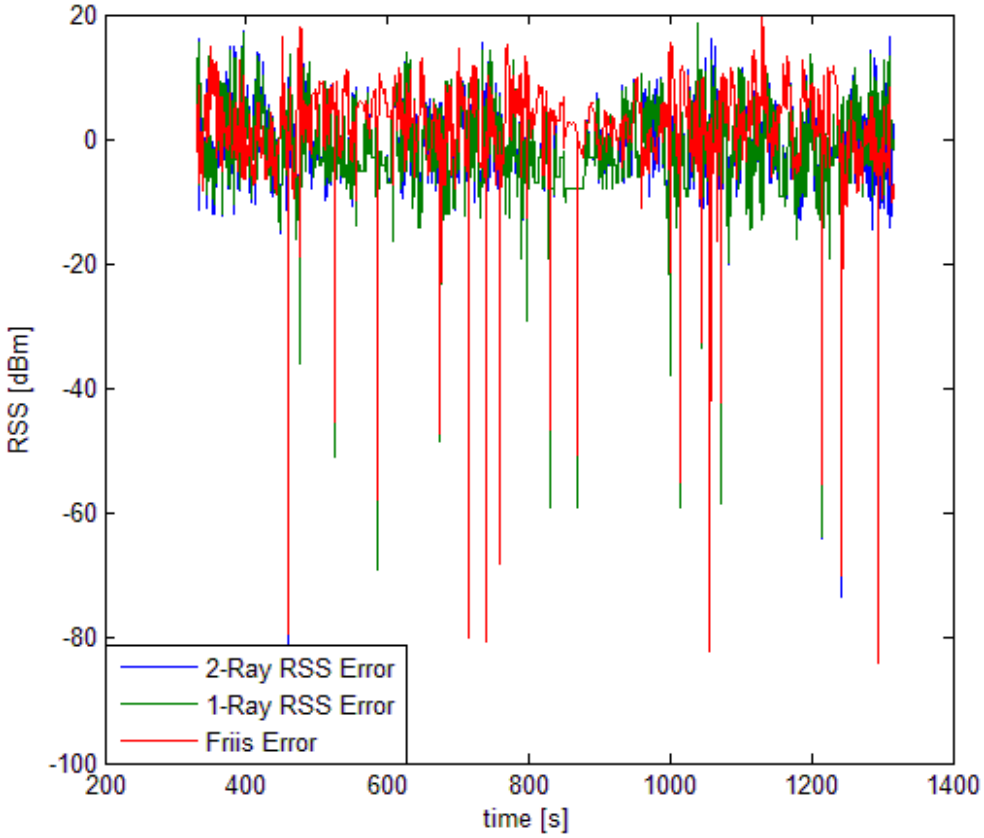

Figure 89: Error vs. Time for AtoG Scenario using GPS Based Heading.

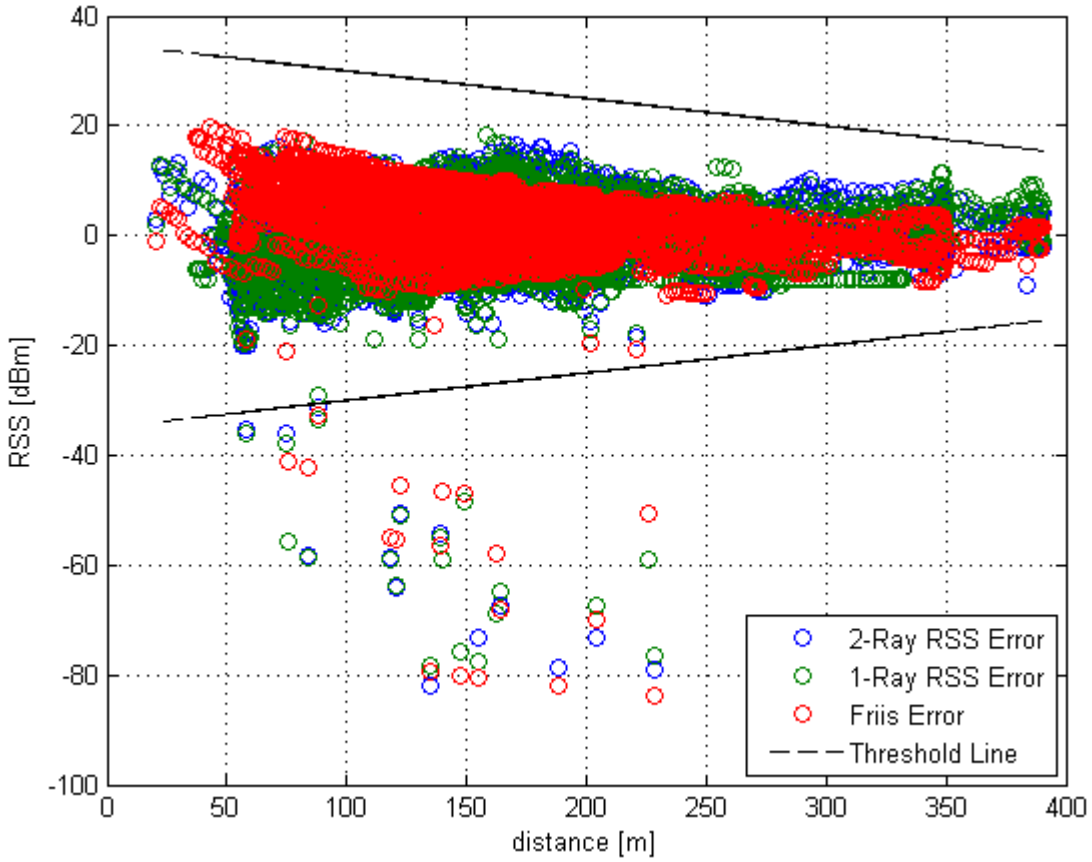

Figure 90: Error vs. Distance for AtoG Scenario using Raw Heading

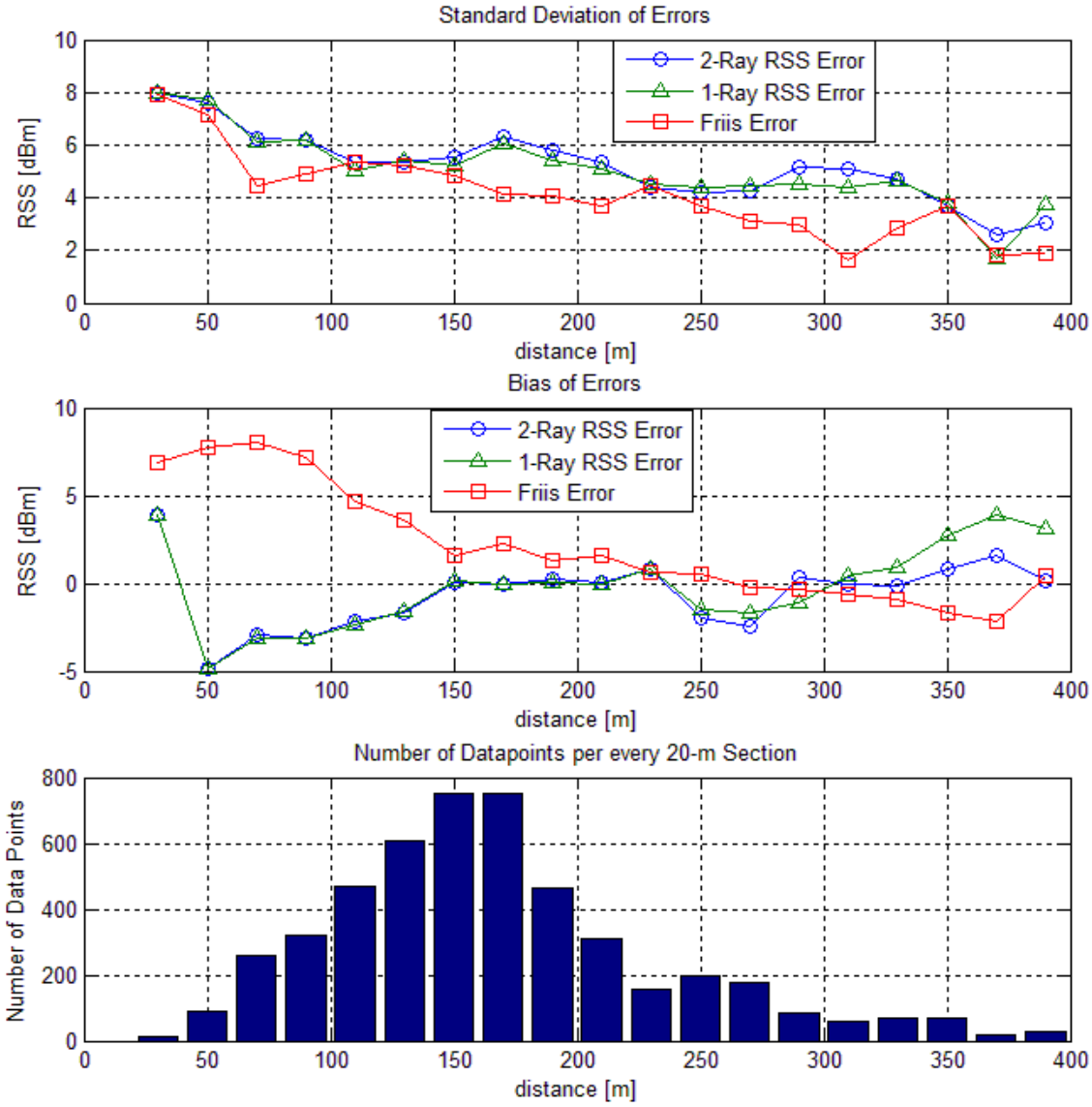

Figure 91: Statistical Analysis of AtoG Scenario with GPS Based Heading.

E.4. Figures from all scenarios combined

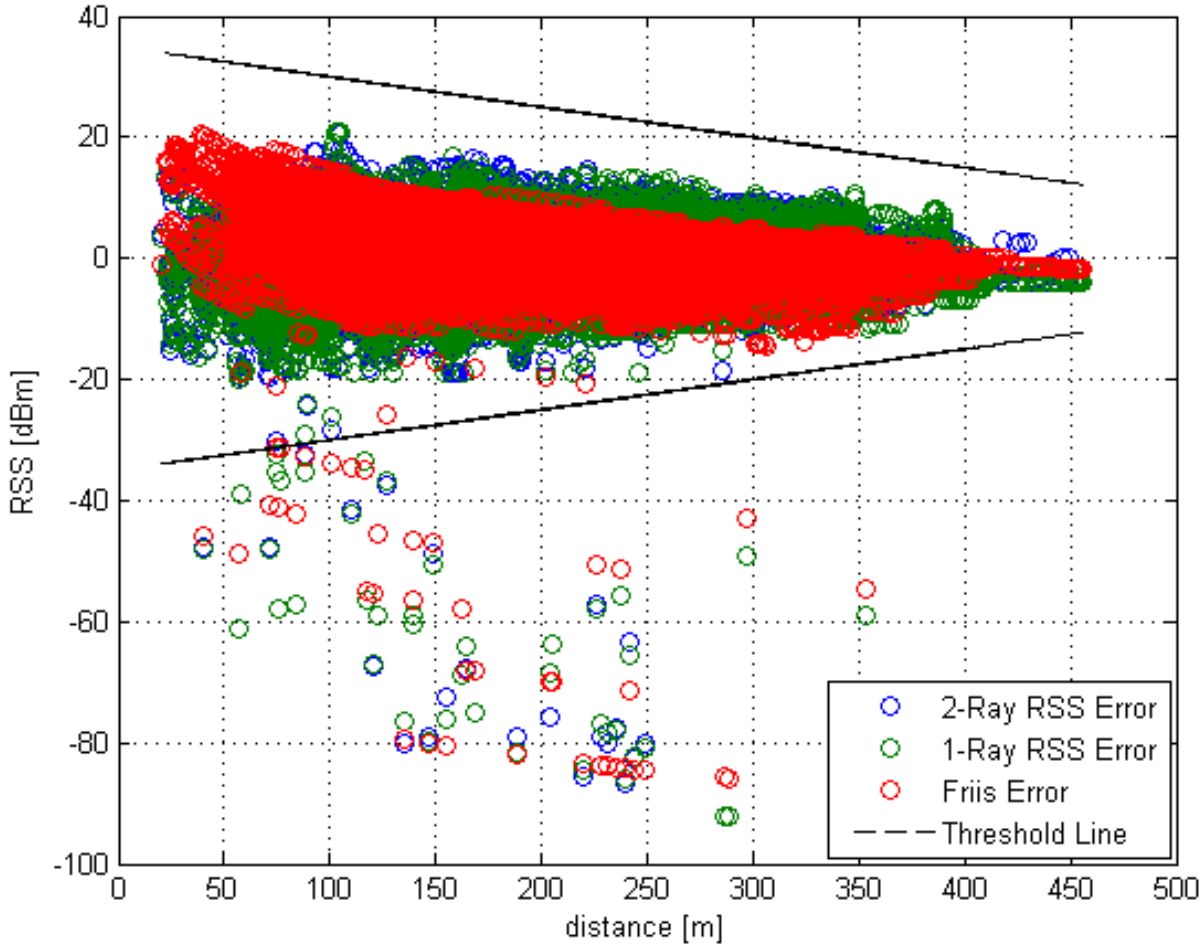

Figure 92: Error vs. Distance for All Scenario using GPS Based Heading.

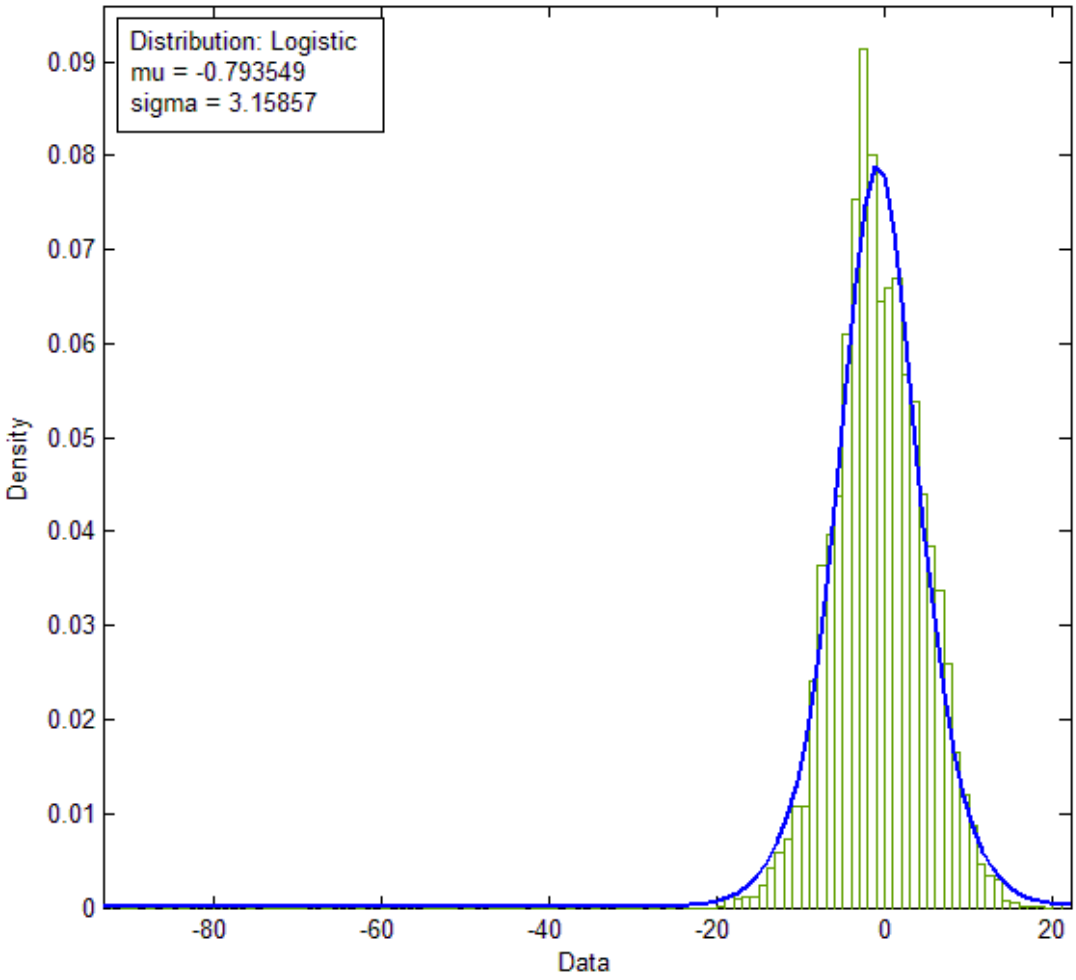

Figure 93: Error distribution of one-ray for all scenarios (data unit is dBm).

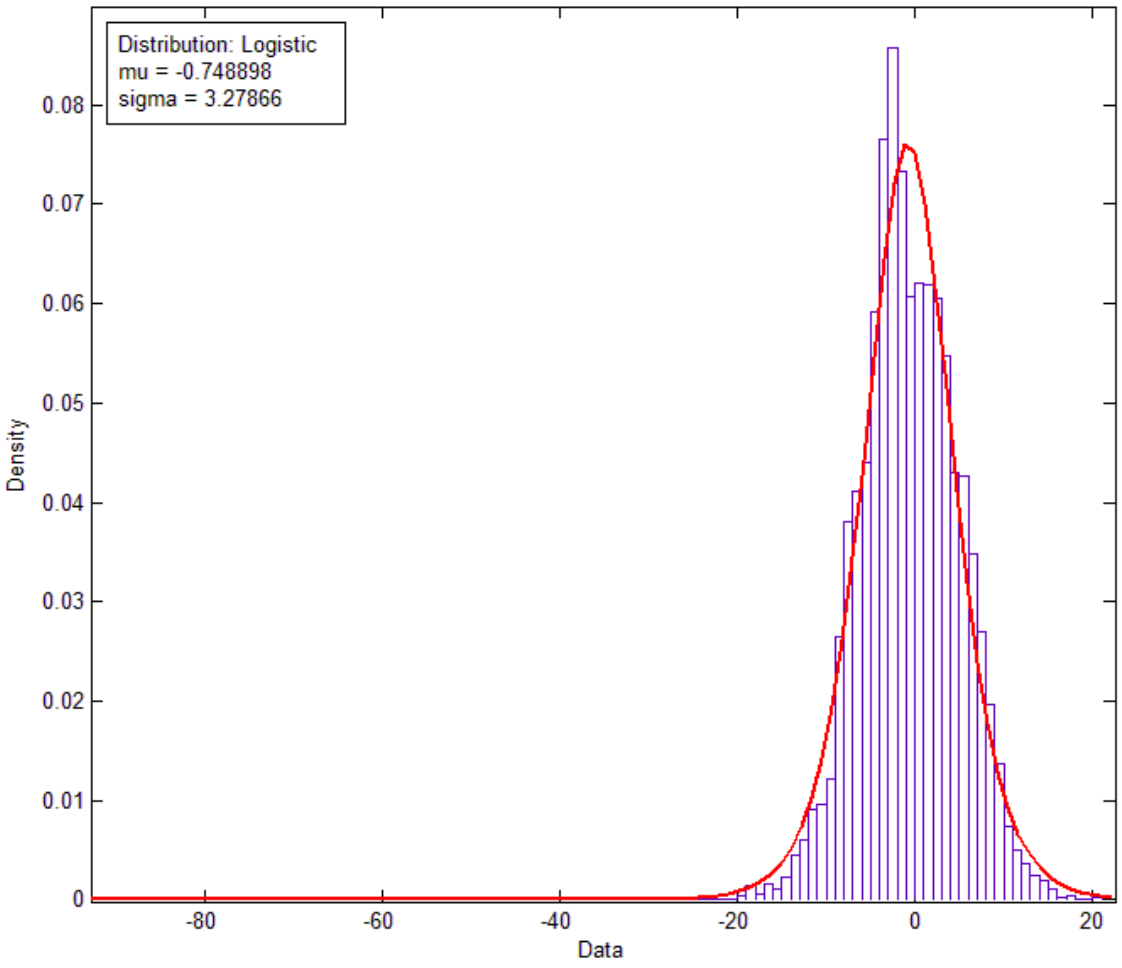

Figure 94: Error distribution of two-ray for all scenarios (data unit is dBm).

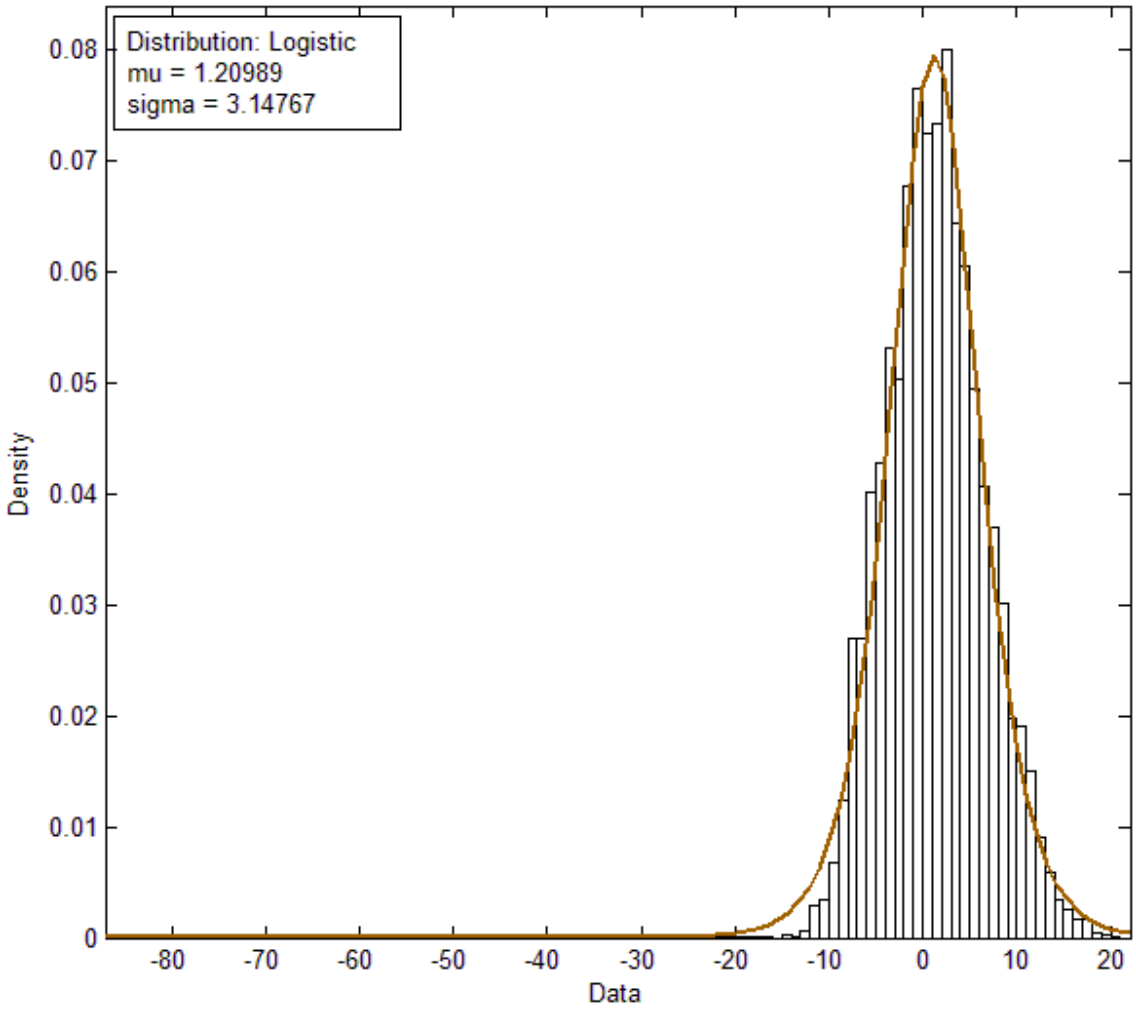

Figure 95: Error distribution of Friis for all scenarios (data unit is dBm).

Bibliography

[1] R. Lee, J. Manner, J. Kim, B. Hurley, P. Amodio, and K. Anderson, ”The role of deployable aerial communications architecture in emergency communications and recommended next steps,” *Federal Communications Commission,* Washington, DC, White Paper DOC-309742A1. September 2011.

[2] K. Pawlikowski, H.-D.J. Jeong, and J.-S.R. Lee, "On credibility of simulation studies of telecommunication networks," *IEEE Communications Magazine,* vol. 40, no. 1, pp. 132-139, 2002. DOI: 10.1109/35.978060.

[3] L. F. Perrone, D. Nicol, and Yuan Yougu, "Modeling and simulation best practices for wireless ad hoc networks," in *Proc. of the 2003 Winter Simulation Conference,* vol. 1, pp. 685-693, 2003. DOI: 10.1109/WSC.2003.1261484.

[4] S. Kurkowski, T. Camp, and M. Colagrosso, "Manet simulation studies: the current state and new simulation tools," Technical Report MCS 06-01, Colorado School of Mines, pp. 1-13, Feb 2006.

[5] T. R. Andel and A. Yasinsac, "On the credibility of manet simulations," *Computer ,*vol. 39, no. 7, pp. 48-54, 2006.

[6] J. H. Hansen, ”Optimal guidance of a relay mav for isr support beyond line-of-sight.” MS Thesis, AFIT/GAE/ENG/08-01, Air Force Institute of Technology, Wright-Patterson AFB, OH. 27 March 2008.

[7] M. T. Seibert, A. J. Stryker, J. R. Ward, and C. T. Wellbaum, ”System analysis and prototyping for single operator management of multiple unmanned aerial vehicles operating beyond line of sight.” MS Thesis, AFIT/GSE/ENV/10-M01, Air Force Institute of Technology, Wright-Patterson AFB, OH, 26 March 2010.

[8] J. P. Boire, ”Autonomous routing of unmanned aerial vehicle (UAV) relays to mimic optimal trajectories in real time.” MS Thesis, AFIT/GSE/ENV/11-M03, Air Force Institute of Technology, Wright-Patterson AFB, OH, 24 March 2011.

[9] T. J. Shuck, ”Development of autonomous optimal cooperative control in relay rover configured small unmanned aerial systems.” MS Thesis. AFIT-ENV-13-M-27, Air Force Institute of Technology, Wright-Patterson AFB, OH, 21 March 2013.

[10] S. A. Songer, ”Aerial networking for the implementation of cooperative control on small unmanned.” MS Thesis. AFIT-ENV-13-M-29, Air Force Institute of Technology, Wright-Patterson AFB, OH. 21 March 2013.

[11] C. M. Durham, ”Evaluation of an OPNET model for unmanned aerial vehicle networks.” MS Thesis. AFIT/GCO/ENG/09-04, Air Force Institute of Technology, Wright-Patterson AFB, OH. 26 March 2009.

[12] K. Daniel, S. Rohde, N. Goddemeier, and C. Wietfeld, ”Cognitive agent mobility for aerial sensor networks,” *IEEE Sensors Journal,* vol. 11 ,no. 11, pp. 2671-2682. 2011. DOI: 10.1109/JSEN.2011.2159489.

[13] S. Morgenthaler, T. Braun, Z. Zhongliang, T. Staub, and M. Anwander, ”UAVNet: A mobile wireless mesh network using unmanned aerial vehicles,” in *Proc. of 2012 IEEE Globecom Workshops*, pp. 1603-1608, 2012. DOI: 10.1109/GLOCOMW.2012.6477825.

[14] T. Stoyanova, F. Kerasiotis, A. Prayati, and G. Papadopoulos, ”Communication-aware deployment for wireless sensor networks,” in *Proc of Second International Conference on Sensor Technologies and Applications*, pp. 217-222, 2008. DOI: 10.1109/SENSORCOMM.2008.97.

[15] D. P. Horner and A. J. Healey, ”Use of artificial potential fields for UAV guidance and optimization of WLAN communications,” *in Proc. Of IEEE/OES 2004 Autonomous Underwater Vehicles Conference*, pp. 88-95, 2004. DOI: 10.1109/AUV.2004.1431198.

[16] Z. Pengcheng, Y. Kai, and A. Swindlehurst, ”Wireless relay communications using an unmanned aerial vehicle,” in *Proc. of IEEE 7th Workshop on Signal Processing Advances in Wireless Communications*. pp. 1-5, 2006. DOI: 10.1109/SPAWC.2006.346492.

[17] C. Chen-Mou, P. Hsiao, H. Kung, and D. Vlah, ”Transmit antenna selection based on link-layer channel probing,” in *Proc. of World of Wireless Mobile and Multimedia Networks 2007 IEEE International Symposium*, pp. 1-6, 2007. DOI: 10.1109/WOWMOM.2007.4351703.

[18] G. Hadynski, S. Lee, G. Rajappan, R. Sundaram, X. Wang, and F. Zhou, ”Optimization of directional antenna network topology in airborne networks,” in *Proc. of 2010 Military Communications Conference*. pp. 68-73, 2010. DOI: 10.1109/MILCOM.2010.5680269.

[19] C. E. Lin, Y. Huang, Y. Lai, Y. Yeh, and W. Huang, ”Airborne antenna tracking for sky-net mobile communication,” in *Proc. of 2011 Fifth International Conference on Sensing Technology*, pp. 569-574, 2011. DOI: 10.1109/ICSensT.2011.6137044.

[20] A. Ayyagari, J. Harrang, and S. Ray, ”Airborne information and reconnaissance network,” in *Proc. of 1996 Military Communications Conference*, vol. 1, pp. 230-234, 1996. DOI: 10.1109/MILCOM.1996.568619.

[21] H. T. Kung, C. Lin, T. Lin, S. Tarsa, and D. Vlah, ”Measuring diversity on a low-altitude UAV in a ground-to-air wireless 802.11 mesh network,” in *Proc. of GLOBECOM Workshops*, pp. 1799-1804, 2010. DOI: 10.1109/GLOCOMW.2010.5700251.

[22] E. K. Çetinkaya, J. Rohrer, A. Jabbar, M. Alenazi, D. Zhang, D. Broyles, K. Pathapati, H. Narra, K. Peters, S. Gogi, and J. Sterbenz, "Protocols for highly-dynamic airborne networks," in *Proc. of the 18th Annual International Conference on Mobile Computing and Networking*, pp. 411-414. 2012. DOI: 10.1145/2348543.2348597

[23] C. Cheng, P. Hsiao, H. Kung, and D. Vlah, "Maximizing throughput of UAV-relaying networks with the load-carry-and-deliver paradigm," in *Proc. of Wireless Communications and Networking Conference*, pp. 4417-4424, 2007. DOI: 10.1109/WCNC.2007.805.

[24] A. Sivakumar, T. Phang, C. Tan, and W. Seah, "Robust airborne wireless backbone using low-cost UAVs and commodity WiFi technology," in *Proc. of 8th International Conference on ITS Telecommunications*. pp. 373-378, 2008.
DOI: 10.1109/ITST.2008.4740289.

[25] H. T. Kung, "Research and demonstration of video streaming on unmanned aerial vehicles (UAV) networks." Harvard University, Cambridge, MA, 2008.

[26] C. Danilov, T. Henderson, T. Goff, J. Kim, J. Weston, N. Neogi, A. Ortiz, and D. Uhlig, "Experiment and field demonstration of a 802.11-based ground-UAV mobile ad-hoc network," in *Proc. in 2009 Military Communications Conference*, pp. 1-7, 2009.
DOI: 10.1109/MILCOM.2009.5379932.

[27] D. Hague. H. Kung, and B. Suter, "Field experimentation of cots-based UAV networking," in *Proc. of 2006 Military Communications Conference*, pp. 1-7. 2006.
DOI: 10.1109/MILCOM.2006.302070.

[28] J. Allred, A. Hasan, S. Panichsakul, W. Pisano, P. Gray, J. Huang, R. Han, D. Lawrence, and K. Mohseni, "SensorFlock: An airborne wireless sensor network of micro-air vehicles," in *Proc. of the 5th International Conference on Embedded Networked Sensor Systems*, pp. 117-129, 2007.

[29] T. X. Brown, S. Doshi, S. Jadhav, and J. Himmelstein, "Test bed for a wireless network on small UAVs," in *Proc. of the 3rd AIAA "Unmanned Unlimited" Technical Conference*, Chicago, IL, pp. 20-30, 2004.

[30] T. X. Brown, B. Argrow, C. Dixon, S. Doshi, R. Thekkekunnel, and D. Henkel, "Ad hoc uav ground network (augnet)," in *Proc. of AIAA 3rd Unmanned Unlimited Technical Conference*. 2004. DOI: 10.2514/6.2004-6321.

[31] M. Gillen, J. Loyall, K. Usbeck, K. Hanlon, A. Scally, J. Sterling, R. Newkirk, R. Kohler, "Beyond line-of-sight information dissemination for force protection," in *Proc. of 2012 Military Communications Conference*, pp. 1-6. 2012.
DOI: 10.1109/MILCOM.2012.6415700.

[32] T. M. Schulteis and J. G. Price, "Project stork UAV/UGV collaborative initiative," *Defense and Security*. International Society for Optics and Photonics, pp. 414-425, 2004.

[33] J. M. Grasmeyer and M. T. Keennon, "Development of the black widow micro air vehicle". *Progress in Astronautics and Aeronautics*, vol. 195, pp. 519-535. 2001.

[34] A. Ryan, M. Zennaro, A. Howell, R. Sengupta, and J. Hendrick, "An overview of emerging results in cooperative UAV control," in *Proc. of 43rd IEEE Conference in Decision and Control*. vol. 1, pp. 602-607, 2004. DOI: 10.1109/CDC.2004.1428700.

[35] U.S. Department of Defense, "DoD Releases Electromagnetic Spectrum Strategy," www.defense.gov/Releases, February 20, 2014, [Online]. Available: http://www.defense.gov/Releases/Release.aspx?ReleaseID=16547

[36] Riverbed, "OPNET IT Guru," support.riverbed.com. [Online] Available: https://support.riverbed.com/bin/support/static//doc/opnet/17.5.A/online/itguru_17.5.PL5/Modules/wwhelp/wwhimpl/js/html/wwhelp.htm#href=FA_10_Ov.060.1.html#47363 (Accessed: 12 March 2014)

[37] C. V. Chung, "Simulation of radiowave propagation in a dense urban environment," MS Thesis, Naval Postgraduate School, Monterey, CA, 2007.

[38] Leidos, "Asymptotic Electromagnetic Radiation Software," www.leidos.com. [Online] Available: https://www.leidos.com/products/software/urbana (Accessed: 13 February 2014)

[39] T. S. Rappaport, *Wireless Communications: Principles and Practice,*2nd ed., New Jersey, Prentic Hall PTR, 1996.

[40] K. Daniel, M. Putzke, B. Dusza, and C. Wietfeld, "Three dimensional channel characterization for low altitude aerial vehicles," in *Proc. of 7th International Symposium on Wireless Communication Systems*. pp. 756-760. 2010. DOI: 10.1109/ISWCS.2010.5624356.

[41] T. Stoyanova, F. Kerasiotis, A. Prayati, G. Papadopoulos, "A practical RF propagation model for wireless network sensors," in *Proc. of 3rd International Conference on Sensor Technologies and Applications*, pp. 194-199, 2009. DOI: 10.1109/SENSORCOMM.2009.39.

[42] N. Ahmed, S. Kanhere, and S. Jha, "Link characterization for aerial wireless sensor networks," in *Proc. of 2011 IEEE GLOBECOM Workshops*, pp. 1274-1279, 2011. DOI: 10.1109/GLOCOMW.2011.6162388.

[43] L. C. Kempel, "Computational Electromagnetics for Antennas" in *Antenna engineering handbook*, 4th ed. J. L. Volakis, New York, McGraw-Hill Book Company, 1984, pp. 59.1-59.29.

[44] S. N. Makarov, *Antenna and EM Modeling with MATLAB*, vol. 1, Princeton University Press, 2002.

[45] S. N. Makarov and L. C. Kempel, "MATLAB Antenna Toolbox. A Draft," 2 February 2006, [Online], Available: http://ece.wpi.edu/mom/ (Accessed: 13 February 2014).

[46] CSGNetwork, "Length of a degree of latitude and longitude calculator," CSGNetwork.com. [Online] Available: http://www.csgnetwork.com/degreelenllavcalc.html (Accessed: 13 February 2014).

[47] TP-LINK Technology, "2.4GHz 8dBi indoor omni-directional antenna," TL-ANT3408CL datasheet, Available: http://www.tp-link.com/en/products/details/?model=TL-ANT2408CL#down.

[48] W. H. Hayt, Jr. and J. A. Buck , "Plane wave reflection and dispersion," in *Engineering Electromagnetics,* 7th ed., 2006, pp. 434-475.

[49] S. S. Haykin and M. Moher, "Propagation and Noise," in *Modern Wireless Communication,* 2004, pp. 11-94.

[50] D. M. Dobkin, "Propagation," in *RF Engineering for Wireless Networks: Hardware, Antennas, and Propagation,* 2011, pp. 251-303.

[51] H. R. Anderson, "Electromagnetic wave propagation," in *Fixed Broadband Wireless System Design,* 2003, pp. 25-68.

[52] W. E. Patitz, B. C. Brock, and E. G. Powell, "Measurement of dielectric and magnetic properties of soil," Sandia National Labs, Albuquerque, NM, 1995. SAND95-2419

[53] S. M. Rao, D. Wilton, and A. W. Glisson, "Electromagnetic scattering by surfaces of arbitrary shape," *IEEE Transactions on Antennas and Propagation*, vol. 30, no. 3, pp. 409-418, 1982. DOI: 10.1109/TAP.1982.1142818

[54] C. A. Balanis, *Antenna Theory: Analysis and Design*, Hoboken, New Jersey, John Wiley & Sons, Inc., 2005.

[55] Artiemis, "What is pcell," [Online]. Available: http://www.artemis.com/pcell (Accessed: 20 February 2014).

[56] Roving Networks, "802.11 b/g Wireless LAN Module," RN-171-XV datasheet, Available: http://ww1.microchip.com/downloads/en/DeviceDoc/rn-171-xv-ds-v1.04r.pdf.

[57] 3DRobotics, "XtreamBee Xbee adapter board," store.3drobotics.com [Online]. Available: https://store.3drobotics.com/products/xtreambee-xbee-adapter-board (Accessed: 14 February 2014).

[58] 3DRobotics, "ArduPilot/APM development site," ardupilot.com [Online]. Available: http://dev.ardupilot.com (Accessed: 14 February 2014).

REPORT DOCUMENTATION PAGE

Form Approved
OMB No. 074-0188

PLEASE DO NOT RETURN YOUR FORM TO THE ABOVE ADDRESS.

1. REPORT DATE *(DD-MM-YYYY)*	2. REPORT TYPE	3. DATES COVERED *(From – To)*
27-03-2014	Master's Thesis	Aug 2012 – March 2014

TITLE AND SUBTITLE

Airborne Wireless Communication Modeling and Analysis with MATLAB

5a. CONTRACT NUMBER

5b. GRANT NUMBER

5c. PROGRAM ELEMENT NUMBER

6. AUTHOR(S)

Vincie, Matthew J., 2nd Lieutenant, USAF

5d. PROJECT NUMBER

5e. TASK NUMBER

5f. WORK UNIT NUMBER

7. PERFORMING ORGANIZATION NAMES(S) AND ADDRESS(S)

Air Force Institute of Technology
Graduate School of Engineering and Management (AFIT/ENY)
2950 Hobson Way, Building 640
WPAFB OH 45433-8865

8. PERFORMING ORGANIZATION REPORT NUMBER

AFIT-ENG-14-M-80

9. SPONSORING/MONITORING AGENCY NAME(S) AND ADDRESS(ES)

Sponsor: AFRL Sensors Directorate, Reference Branch
Name: Dr. Jacob Campbell (Research Engineer)
Telephone number: (293) 255-6127 x 4154 (jacob.campbell@wpafb.af.mil)

10. SPONSOR/MONITOR'S ACRONYM(S)

11. SPONSOR/MONITOR'S REPORT NUMBER(S)

12. DISTRIBUTION/AVAILABILITY STATEMENT

DISTRUBTION STATEMENT A. APPROVED FOR PUBLIC RELEASE; DISTRIBUTION UNLIMITED.

13. SUPPLEMENTARY NOTES

14. ABSTRACT

Over the past decade, there has been a dramatic increase in the use of unmanned aerial vehicles (UAV) for military, commercial, and private applications. Critical to maintaining control and a use for these systems is the development of wireless networking systems [1]. Computer simulation has increasingly become a key player in airborne networking developments though the accuracy and credibility of network simulations has become a topic of increasing scrutiny [2-5]. Much of the inaccuracies seen in simulation are due to inaccurate modeling of the physical layer of the communication system. This research develops a physical layer model that combines antenna modeling using computational electromagnetics and the two-ray propagation model to predict the received signal strength. The antenna is modeled with triangular patches and analyzed by extending the antenna modeling algorithm by Sergey Makarov, which employs Rao-Wilton-Glisson basis functions. The two-ray model consists of a line-of-sight ray and a reflected ray that is modeled as a lossless ground reflection. Comparison with a UAV data collection shows that the developed physical layer model improves over a simpler model that was only dependent on distance. The resulting two-ray model provides a more accurate networking model framework for future wireless network simulations.

15. SUBJECT TERMS

Aerial Networking, Antenna Modeling, UAV, UAS, Data Links, Airborne Communication

16. SECURITY CLASSIFICATION OF:			17. LIMITATION OF ABSTRACT	18. NUMBER OF PAGES	19a. NAME OF RESPONSIBLE PERSON
a. REPORT	b. ABSTRACT	c. THIS PAGE			Dr. Gilbert L. Peterson, AFIT/ENG
U	U	U	UU	146	19b. TELEPHONE NUMBER *(Include area code)* (937) 255-6565, ext 4281 (gilbert.peterson@afit.edu)

Standard Form 298 (Rev. 8-98)
Prescribed by ANSI Std. Z39-18